



**Space weather impacts on  
ground-based energy  
infrastructure**

Zoë Maria Lewis

Supervisor: Prof. Jim Wild

*August 2021*

Word count: 12485

## Abstract

It is well documented that space weather may impact electricity infrastructure. Several widespread blackouts have been observed in the past few decades and directly linked to the largest geomagnetic storms (e.g. the Hydro Québec incident in 1989). However, less is known about the impact of lower-level geomagnetically induced currents (GICs) on the health of transformers in the long term. In this study, dissolved gas data from UK power station transformers were analysed in detail in a space weather context for the first time. Dissolved gas measurements from 2010–2015 were used to look for evidence of a link between degradation of the transformer insulation and heightened levels of SYM-H and  $\frac{dB}{dt}$  as measured at Eskdalemuir and Hartland magnetometer stations. Firstly, case studies were examined of the most significant storms in this time period using dissolved gas analysis (DGA) methods, specifically the Low Energy Degradation Triangle (LEDT). The case studies were then augmented with a statistical survey, including Superposed Epoch Analysis (SEA) of multiple storm events. No evidence of a strong space weather impact can be found during this time period, likely due to the relatively quiet nature of the Sun during this epoch and the modernity of the transformers studied.

## Declaration of Authorship

I, Zoë M. Lewis, declare that this thesis titled ‘Space weather impacts on ground-based energy infrastructure’ and the work presented in it are my own. I confirm that:

- This work was done wholly or mainly while in candidature for a research degree at this University.
- Where any part of this thesis has previously been submitted for a degree or any other qualification at this University or any other institution, this has been clearly stated.
- Where I have consulted the published work of others, this is always clearly attributed.
- Where I have quoted from the work of others, the source is always given. With the exception of such quotations, this thesis is entirely my own work.
- I have acknowledged all main sources of help.
- Where the thesis is based on work done by myself jointly with others, I have made clear exactly what was done by others and what I have contributed myself.

Signed:

Date: 14th August 2021

## Acknowledgements

I would like to first acknowledge the data sources used in this dissertation. The Dissolved Gas data were provided by Douglas Barker at EDF Energy. SYM-H, Dst and K indices were accessed from the World Data Center for Geomagnetism, Kyoto, and for the ground magnetometer data we gratefully acknowledge INTERMAGNET, Alan Thomson and SuperMAG, PI Jesper W. Gjerloev. The geomagnetic storm list was provided by Maria Walach, extended to cover the time period 1981–2019 using the algorithm described in the paper Walach *et al.* (2019). The OMNI sunspot data were obtained from the GSFC/SPDF OMNIWeb interface at <https://omniweb.gsfc.nasa.gov>.

This project would not have been possible without the help of many individuals. I would like to thank my supervisor Jim for making this project so enjoyable and productive, entirely remotely and during a very strange year. Thanks also to the entire SPP group at Lancaster for making me feel welcome through the medium of Microsoft Teams, and for their helpful suggestions and feedback on my work. I would also like to acknowledge the contributions of Matt Allcock and Douglas Barker at EDF energy, who provided valuable insight and support to the project as well as the data on which this work is based. Also to Trevor Gaunt at the University of Cape Town for his advice and assistance in applying the LEDT method.

On a personal note, this project would have been a lot harder without the support of my friends Ollie, Connor and Arnav. They provided endless Python troubleshooting and always help me out of whatever rut I've got myself into. I'm looking forward to seeing what they do next. Finally, thanks are due to my family. Without their support I would not have been able to complete this project, particularly during such a difficult year.

# Contents

<b>1</b>	<b>Introduction and background</b>	<b>6</b>
1.1	What is space weather? . . . . .	6
1.2	The solar-terrestrial connection . . . . .	7
1.2.1	Drivers of space weather . . . . .	7
1.2.2	Geomagnetic indices . . . . .	9
1.3	Geomagnetically Induced Currents . . . . .	12
1.4	Transformers . . . . .	14
1.4.1	GIC risk to transformers . . . . .	14
1.4.2	Dissolved Gas Analysis . . . . .	17
<b>2</b>	<b>Data</b>	<b>21</b>
2.1	Time period studied . . . . .	21
2.2	Space weather data . . . . .	23
2.2.1	Rate of change of horizontal magnetic field component . . . . .	23
2.2.2	SYM-H . . . . .	26
2.3	Storm identification . . . . .	29
2.4	Dissolved Gas data . . . . .	31
<b>3</b>	<b>Dissolved Gas Analysis</b>	<b>33</b>
3.1	LEDT . . . . .	35
3.1.1	Method . . . . .	35
3.1.2	Case study 1 . . . . .	36
3.1.3	Case study 2 . . . . .	37
3.1.4	Case study 3 . . . . .	38
3.1.5	Discussion . . . . .	39
3.2	Duval triangle . . . . .	40
3.3	Key Gas Ratio . . . . .	40
<b>4</b>	<b>Superposed Epoch Analysis</b>	<b>42</b>
<b>5</b>	<b>Further analysis</b>	<b>45</b>
5.1	Heat maps . . . . .	45

5.2 Cross correlation . . . . .	46
<b>6 Discussion and suggestions for future work</b>	<b>50</b>
<b>7 Summary and conclusions</b>	<b>52</b>
<b>A Event lists</b>	<b>60</b>
<b>B Raw gas concentrations</b>	<b>62</b>
<b>C LEDTs</b>	<b>65</b>
<b>D Superposed Epoch Analysis</b>	<b>76</b>

# 1 Introduction and background

## 1.1 What is space weather?

Space weather refers to variability in the complex solar-terrestrial system by which activity at the Sun's surface can influence conditions at the Earth (Eastwood, 2008). This system comprises and links the Sun, the solar magnetic field, the magnetised solar wind, and Earth's magnetosphere, ionosphere, and neutral atmosphere (Cannon, 2013). Space weather has the potential to impact human life in many ways, particularly as society has become increasingly reliant on technology.

The best-known effects of this solar-terrestrial connection are the aurora borealis and aurora australis (the northern and southern lights), attracting many tourists to the polar regions and being a source of artistic and cultural inspiration for centuries (Figure 1). However, it wasn't until the Carrington Event in 1859 (Carrington, 1859) that the scientific community began to fully appreciate that activity at the Sun was directly linked to an observation of increased auroral activity at the Earth.



Figure 1: The Aurora borealis, or northern lights, above Bear Lake, Alaska (photo by Senior Airman Joshua Strang, distributed by Wikimedia Commons)

As technological advances have been made, the potential for more damaging space weather impacts has become clear. A large solar event is predicted to cause trillions of pounds worth of damage to critical infrastructure, harming not only the economy but also endangering human lives (Oughton *et al.*, 2019). As with

any risk, acquiring knowledge about how and why its impact may be felt is the first step towards mitigation.

One of the greatest challenges of this work is the relative infrequency of such large events. For example, a Carrington-sized event is forecast to occur about once every 100 years (Riley *et al.*, 2017), and detailed digital measurements of the geomagnetic field have only been taken for the past few decades. As demonstrated by the COVID-19 pandemic, rare but disastrous global events can and do happen, and complacency only increases the damage caused. This is why space weather, along with pandemics and other natural and human-made disasters are considered in the UK Government’s 2020 Risk Register (Cabinet Office, 2020), with severe space weather categorised as a level C (moderate) and relatively likely (a 25–125 in 500 chance of the reasonable worst case scenario occurring in the next year) risk in the UK. An unpredicted 1-in-100 year Carrington sized event would cause £15.9 billion of GDP loss in the UK (Oughton *et al.*, 2019). With improved event forecasting this could be reduced to £0.9 billion. These figures highlight the importance of research in this area, to improve forecasts of space weather events and mitigate their impact.

In this project, we looked for evidence of space weather impacts on a set of 13 UK power transformers, during a relatively quiet epoch (2010–2015). We examined dissolved gas data (regularly recorded during normal operation of the transformers) to ascertain whether there was evidence of a deterioration in transformer health as a result of geomagnetic storms during this time period.

## **1.2 The solar-terrestrial connection**

### **1.2.1 Drivers of space weather**

The activity of the Sun varies over an 11 year timescale, from solar maximum to solar minimum (see Figure 2). At the maximum, there is an increase in X-ray and ultraviolet emissions from the Sun and an increase in the number of sunspots (areas of increased magnetic activity) visible on the surface. The Sun’s magnetic field also switches polarity during the maximum activity, so the cycle actually has a 22 year period.

Superimposed on this long-term variation is the smaller scale and shorter term

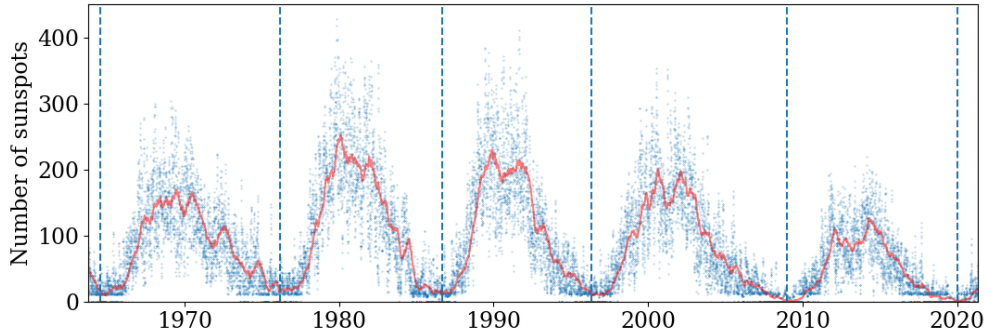


Figure 2: Sunspot numbers over the last 5 solar cycles. Red line shows the 6-month rolling mean, and blue vertical lines delineate solar cycles.

changes driving space weather (Cannon, 2013). The solar wind is an outflow of supersonic charged particles from the Sun’s corona (300–500 km/s), which meets the Earth’s magnetic field at the *magnetopause*, a surface over which the solar wind and terrestrial magnetic field pressures balance. The solar wind pressure distorts the magnetosphere such that it is compressed on the dayside and stretched out into a *magnetotail* on the nightside (Baumjohann *et al.*, 2012) (see Figure 3). Figure 3 also shows the interplanetary magnetic field (IMF): the component of the solar magnetic field which is frozen in the solar wind plasma and drawn out to fill the solar system as the solar wind expands away from the Sun (Baumjohann *et al.*, 2012). In this image the IMF is directed southwards, but in reality it can have any orientation.

Several types of solar event can drive changes in the solar wind speed and pressure. The most significant drivers of space weather are coronal mass ejections (CMEs): large releases of plasma and magnetic field from the Sun’s corona. CMEs are more common during solar maximum, when the sunspot number is high and the Sun’s magnetic field is more unstable. Another source is stream interaction regions (SIRs), which are formed when a slow solar wind stream is overtaken by a fast one, becoming compressed and higher in energy. If directed towards Earth, a CME will take 1–3 days (Thomson *et al.*, 2010) to arrive at the magnetopause.

The magnetosphere protects the Earth from the majority of the solar wind’s variability. When a CME or SIR is directed towards the Earth, a particularly dense and fast region of the solar wind impinges on the magnetosphere. When

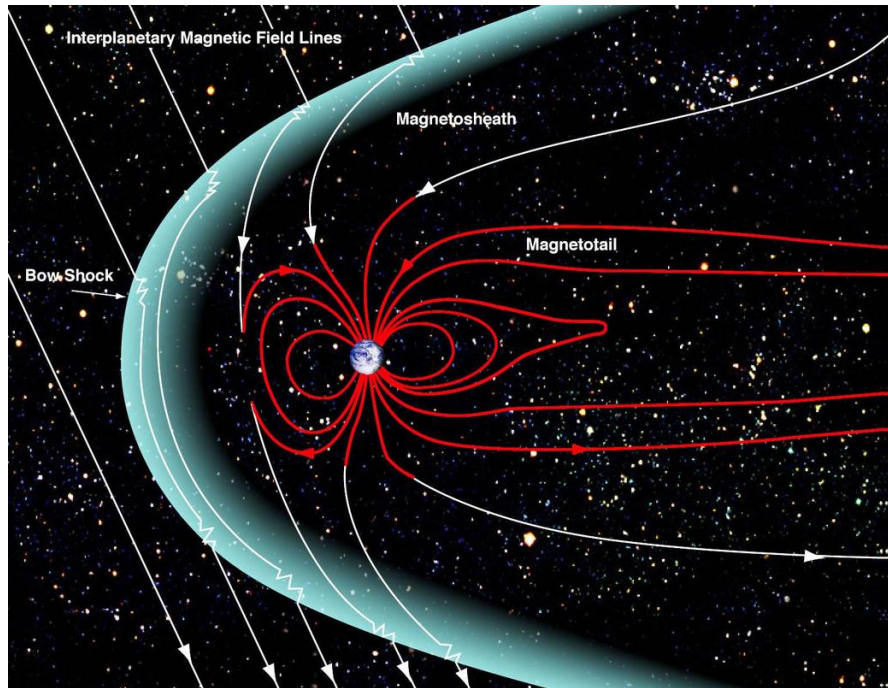


Figure 3: Diagram showing Earth's magnetosphere. *Source: NASA Goddard/Aaron Kaase*

the IMF has a southward-pointing component, the northward pointing magnetic field lines of the Earth on the sun-facing side (dayside) of the magnetopause may merge with the IMF, changing the arrangement of the magnetic field lines and converting magnetic energy into kinetic energy of the charged particles (*dayside reconnection*). When this occurs, the event is said to be *geomagnetic*. This process allows solar wind energy to penetrate the magnetosphere and be transported to the magnetotail on the nightside of the planet, and into the upper atmosphere. This energy builds up until it reaches a critical level when *nightside reconnection* occurs, directing plasma towards the Earth in a *substorm* (Cannon (2013), Dungey (1961)).

### 1.2.2 Geomagnetic indices

We measure geomagnetic activity, and identify when a geomagnetic storm has occurred, with a set of defined indices based upon ground magnetic field measurements. Figure 4 presents some of the indices commonly used in this study.

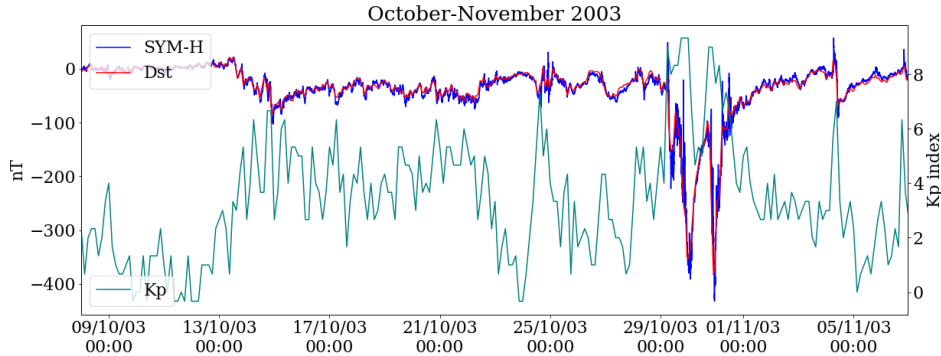


Figure 4: Comparison of 3 geomagnetic indices October-November 2003

The K index is a quasi-logarithmic index, which measures the intensity of the magnetic disturbance from the expected norm every three hours (Moldwin, 2008). It has 28 discrete allowed values (0, 0+, 1-, 1, 1+, ... 9). The planetary K index (Kp) is the mean of the K index measured from 13 different geomagnetic observatories (Chakraborty *et al.*, 2020). Its use in this study is limited due to its discrete nature and the fact that it saturates at 9 during extreme space weather conditions.

The disturbance storm time (Dst) index is a measure of the change in the Earth's magnetic field due to an intensification of the ring current (Moldwin (2008) and Borovsky *et al.* (2017)) (a current due to the longitudinal curvature drift of charged particles trapped in the Earth's magnetosphere). The index is calculated using hourly averages of the northward horizontal field component ( $H(t)$ ) as measured at four ground magnetometer stations at low geomagnetic latitudes. These are Honolulu, San Juan, Hermanus and Kakioka. A baseline 'quiet' reference level ( $H_0(t)$ ) is subtracted from each station's reading to give the disturbance from undisturbed conditions. The 'solar quiet' current (Sq current,  $H_{Sq}(t)$ ) created by the tidal motion of the atmosphere is also subtracted at this stage. They are then averaged to reduce local effects, and multiplied by the average of the cosines of the geomagnetic latitudes ( $\Lambda_n$ ). Equation 1 then gives a value for the ring current

field at the magnetic equator (Baumjohann *et al.*, 2012).

$$\text{Dst}(t) = \frac{1}{16} \left[ \sum_{n=1}^{n=4} \cos \Lambda_n \right] \left[ \sum_{n=1}^{n=4} (H(t) - H_0(t) - H_{Sq}(t)) \right] \quad (1)$$

When a storm occurs, the ring current becomes enhanced with charged particles from the magnetotail. The magnetic field generated by this current acts to oppose the dipole-like magnetic field of the Earth, resulting in a dip in the observed magnetic field during storm times. Therefore more negative values of Dst (in nT) correspond to storm conditions.

The SYM-H index is very similar to the Dst index, as they both measure the intensity of the ring current. However, a difference arises in the method used to determine these indices: SYM-H has a 1-minute time resolution, compared to 1 hour for Dst. SYM-H also uses six ground magnetometer stations instead of four, and the stations used change on a monthly basis according to data quality and availability. SYM-H provides a more detailed depiction of the ring current due to its smaller time resolution, and can be numerically different to Dst due to the greater and more evenly spread range of latitudes used (Wanliss *et al.*, 2006).

The phases of a geomagnetic storm can then be clearly seen by examining how the Dst or SYM-H index changes during this time. Figure 5 shows how the SYM-H index varies during the so-called St Patrick’s day storm in March 2015. Firstly, there is an initial phase in which the increased solar wind pressure compresses the dayside magnetosphere, increasing the northward component of the ground magnetic field so an increase in SYM-H is observed. This phase is shown in yellow in the figure. The ring current then becomes strongly enhanced, causing the magnetic field to weaken and the value of SYM-H to drop (Walach *et al.*, 2019). This is the main phase of the storm, and is shown in red. During the recovery phase, shown in green, the driving of the solar wind eases, and the ring current (and therefore Dst) slowly returns to normal conditions (Hutchinson *et al.*, 2011).

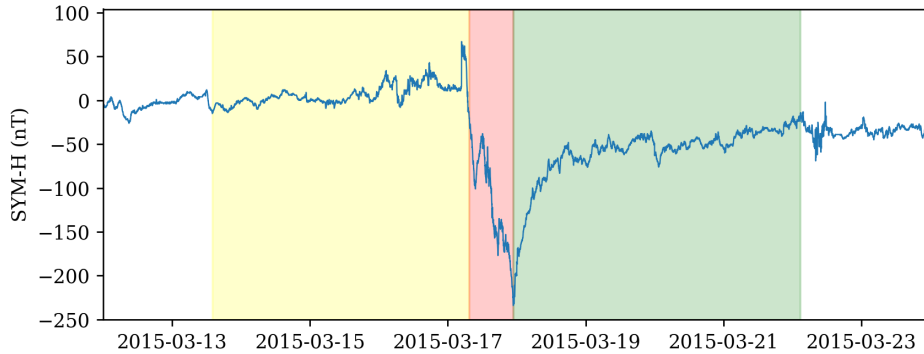


Figure 5: SYM-H for March 2015 storm, showing the three storm phases. The yellow shaded region shows the initial phase, red shows the main phase, and green the recovery phase.

A final measurement used in this report is the rate of change in the horizontal component of the measured magnetic field ( $\frac{dB}{dt}$ ) (Gjerloev, 2012). This is more localised than the previous indices mentioned, in that it is measured independently at each magnetometer station. Since changes in the horizontal magnetic field are believed to be the primary driver of geomagnetically induced currents (GICs), it is a useful quantity for measuring space weather impacts due to this effect.

### 1.3 Geomagnetically Induced Currents

There are many examples of infrastructure in the modern world which are vulnerable to space weather. Examples include satellites, GPS systems, aircraft, radio communication, and railways (Cannon, 2013). In this project, we focus on the risk to ground based energy infrastructure; the electricity grid and the network of power lines and transformers which underpins it. This system is particularly vulnerable to geomagnetically induced currents (GICs).

When the Earth’s magnetic field varies due to solar activity, the time varying flux induces an electric field in the ground due to Faraday’s law of induction (Dimmock *et al.*, 2020). The geoelectric field will then produce a current in any conducting material, such as a power line or pipe. GICs are more likely to occur at solar maximum (although they do occur at other times in the solar cycle), and

their size and risk depends on a number of factors (Thomson *et al.*, 2010). The geological structure and proximity to the coast affects the ground impedance, and therefore the magnitude of GICs generated (Thomson *et al.*, 2005). Through these variations, the conductivity can vary by up to 5 orders of magnitude (Molinski, 2002). Electricity networks provide a ‘path of least resistance’ for the GICs, and the vulnerability of a particular node depends on its level of interconnection with the rest of the network (Kelly *et al.*, 2017), and on the orientation of the GICs with respect to the power lines (Dimmock *et al.*, 2020).

Another factor affecting the size of GICs, and therefore their potential for causing damage, is latitude. Regions closer to the auroral oval will experience stronger GICs, and will therefore be more vulnerable to infrastructure damage from space weather. Figure 6 shows magnetometer stations coloured by the size of the 99.97th percentile in  $\frac{dB}{dt}$ . The contours show lines of constant geomagnetic latitude. It is clear that the stations in the auroral zones (around 55–75° magnetic latitude) experience the highest  $\frac{dB}{dt}$  values in general, and are therefore also more likely to experience the largest GICs. However, during a geomagnetic storm the auroral oval expands equatorward, and this leads to higher  $\frac{dB}{dt}$  at lower latitudes.

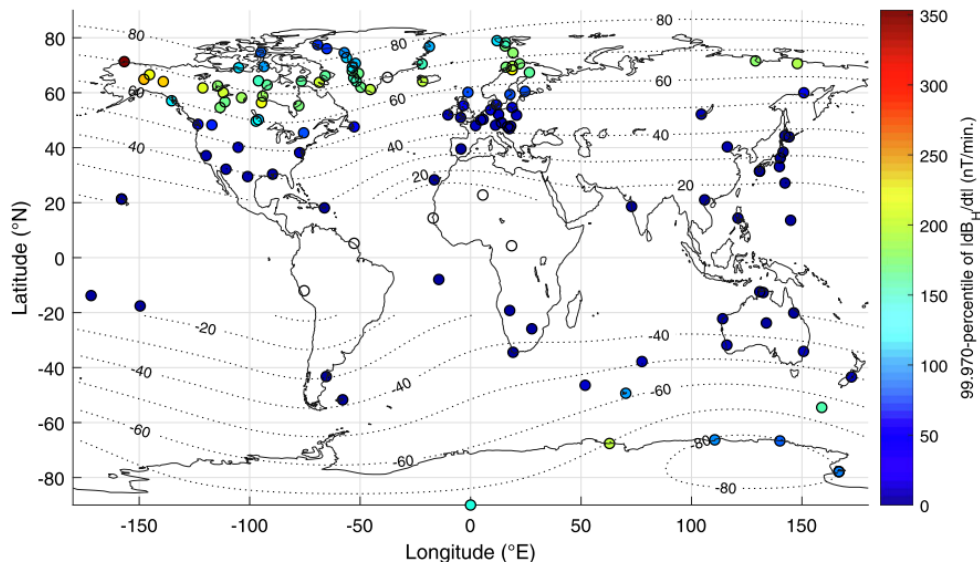


Figure 6: Figure 2 from Rogers (2020), showing the 99.97th percentile in  $\frac{dB}{dt}$  values as measured at magnetometer stations around the world.

All these factors mean that predicting the size and effect of GICs presents a challenge. Such a prediction is outlined for the UK in Beggan *et al.* (2013), and the methodology is as follows. First, a model was made of the ground conductivity using geological properties and measurements throughout the UK. A ‘thin sheet model’ was then used to compute the geoelectric field, and used together with a model of the 400kV and 275kV power networks to then predict the GIC within each transformer node. The results show the theoretical response of the electricity network to an extreme space weather response.

Similar studies have been performed for different regions include France (Kelly *et al.*, 2017), Sweden (Pulkkinen *et al.*, 2005), New Zealand (Rodger *et al.*, 2017), Czechia (Švanda *et al.*, 2020), Brazil (Trivedi *et al.*, 2007), and Spain (Torta *et al.*, 2012). In this report, global (SYM-H) and local ( $\frac{dB}{dt}$ ) geomagnetic indices are used as a proxy for more detailed GIC measurements, which weren’t routinely measured at power stations during this time period. This is adequate as all measures should respond to the same global storm events. However, when results are interpreted for individual transformers, the localised and unpredictable nature of GICs should be noted.

The highest recorded value of  $\frac{dB}{dt}$  was 2700 nT/min in 1982 in Sweden, and the highest measured in the UK was 1100 nT/min in 1989 (Hapgood *et al.*, 2021). Worst case scenario estimates place a 4000–5000 nT/min event roughly once every 100 years, corresponding to GICs of 100s of nT. It is predicted that 6 transformers in England and Wales and 7 in Scotland could be taken out of service during such an event (Hapgood *et al.*, 2021). Space weather events of this magnitude are yet to be observed in modern history, however examining smaller events may allow us to extrapolate and predict the impact of larger ones.

## 1.4 Transformers

### 1.4.1 GIC risk to transformers

Transformers are a crucial part of any electricity grid. They allow voltage to be stepped up to reduce losses in long-range power lines and stepped down to a safe level for homes and businesses. There are an estimated 684,000 distribution transformers in the UK, with the vast majority being part of Distribution Net-

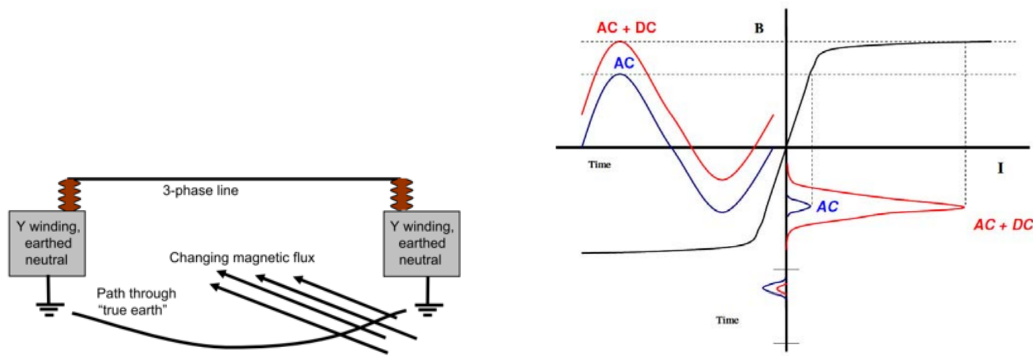
work Operator (DNO) networks (Department for Environment *et al.*, 2013). Most transformers are also oil-filled, as opposed to ‘dry’ transformers which are used where transformer oil might be a fire hazard. The typical lifespan for both transmission and distribution transformers is around 40 years, however several factors can reduce this and result in premature failure and early replacement.

GICs have the potential to damage transformers, a process described in detail in Girgis *et al.* (2012) and Molinski (2002). Quasi-DC currents flow through the grounded neutral (see Figure 7a), offsetting the AC wave by the size of the GIC. Therefore, in one half of the cycle the flux magnitude is increased from the non-GIC level, and in the other half of the cycle the flux magnitude is decreased (see Figure 7b). As can be seen from the B-I characteristic in the figure, under normal operation the transformer operates close to its saturation point, so this DC shift moves the area of operation into the saturation zone during the positive half of the cycle. This is called half-cycle saturation, and effectively means that during GIC exposure the transformer is operating out of the linear flux range it was designed to operate within (Girgis *et al.* (2012) and Molinski (2002)). This leads to stray flux, no longer confined to the transformer core, and approximately proportional to the exciting current.

Stray flux exterior to the core drives eddy currents, causing localised heating. The temperature increase then breaks down the insulation and oil within the windings (Oughton *et al.* (2019) and Pulkkinen *et al.* (2017)), releasing bubbles of gas. The tendency of a particular transformer to have unwanted heating depends on its design, in particular the geometries of the core and windings, and the resistivity of the constituent parts. The exciting current also has harmonics, which can trigger the protective relays and cause tripping (Molinski, 2002).

Power system problems due to GICs were first observed in 1940 (Boteler, 2014), and several examples of transformer damage due to GICs have been documented since. One such example occurred in March 1989 (Allen *et al.*, 1989).

In March 1989, a CME followed by an X15 solar flare erupted in a large sunspot group, producing a period of heightened solar activity lasting around 2 weeks and causing SYM-H as extreme as  $-720$  nT. The most significant impact felt on Earth was in Québec Province, Canada, where the Hydro-Québec Power Company experienced a blackout affecting 6 million people for around 9 hours (Oughton *et*



(a) Figure 3 from Gaunt (2014), showing how GICs interact with transformers.

(b) Figure 1b from Girgis *et al.* (2012), showing how half-cycle saturation of a transformer occurs.

Figure 7

*al.*, 2019). This was the result of large magnetic field changes, inducing GICs at the James Bay station. The transformers were saturated, tripping circuit breakers and cutting off power until they could be restored. For a more detailed description of the nature and effects of this event, see Allen *et al.* (1989). Though these events may seem rare, electricity systems built to last several decades must be resilient to large geomagnetic events.

A more recent geomagnetic storm event was the Halloween storm on 29th–30th October 2003. This storm was triggered by two solar flares from the same active region of the sun on the 28th and 29th of October. The first was an X17 X-ray flare, one of the largest recorded, and the second an X10. Both flares had associated CMEs that were directed towards Earth (Thomson *et al.*, 2005). The Dst index reached  $-400$  nT during the subsequent geomagnetic disturbances, and auroral displays were visible at much lower latitudes than usual, including throughout the UK, and the auroral oval expanded as far south as Texas (Thomson *et al.*, 2010). In Southern Sweden, resulting GICs produced harmonic distortions and tripped protective relays in the electricity network, leading several transformers to become disconnected during the storm, and an outage in the Malmö region cut power to 50,000 customers (Pulkkinen *et al.*, 2005).

In this study, the effect of smaller, more frequent geomagnetic events on transformer health is investigated. Do GICs have a cumulative negative effect on elec-

tricity infrastructure, and are their lifetimes being shortened by persistent space weather? Do smaller storms have a low-energy impact on transformer health that can be extrapolated to predict the effect of larger events?

Weygand (2021) considered two critical thresholds for the rate of change in the horizontal geomagnetic field associated with problems in the electrical grid: 90 nT/min (Pulkkinen *et al.*, 2011) and 300 nT/min (Molinski, 2002). It will be shown that even the lower of these thresholds is rarely reached in the UK during quiet solar periods such as 2010–2015.

#### 1.4.2 Dissolved Gas Analysis

Figure 8 shows the concentration in ppm of four key gases (hydrogen, methane, ethylene and ethane) for two transformers in South Africa in the months following the 2003 Halloween storm. It is clear that during the time following the storm's maximum on the 29th October 2003, the concentrations of several gases within the transformer increased considerably; particularly methane, ethylene and ethane in transformer 1. Both transformers were removed from service approximately 6 months after the storm. This is a good example of dissolved gas analysis used to identify damage caused by GIC activity prior to an actual fault developing and causing the transformer to be discontinued in its use.

As heating occurs within a transformer, the insulating materials break down and release detectable amounts of the gases. These measurements can be used to determine what kind of damage is occurring or has occurred within the transformer itself.

Dissolved Gas Analysis (DGA) is a method of assessing transformer health, to diagnose and predict faults without removing the transformer from operation. Eight different trace gases are typically measured in the transformer oil, and the distribution of gases can be related to the fault type. Gas measurements are regularly taken for all transformers, whereas direct GIC measurements at transformer sites are not common. For this reason, DGA is a useful method for determining space weather impacts by indirectly measuring the transformer health using data with far greater availability.

In this project three different DGA methods were considered:

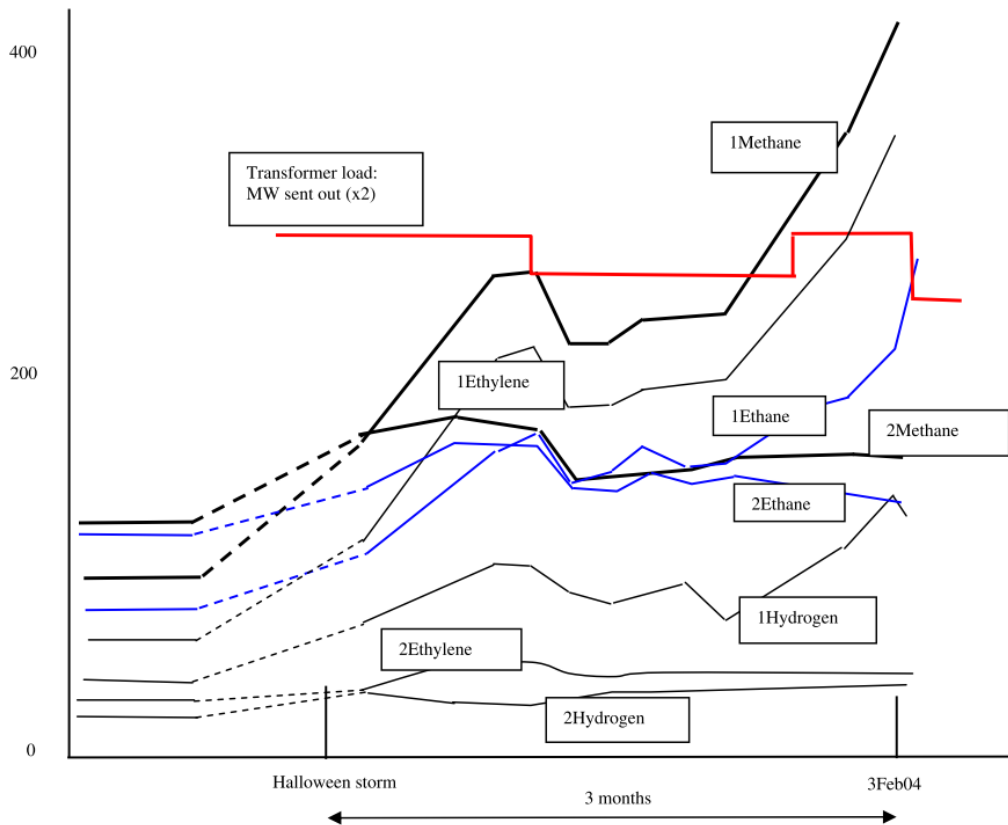


Figure 8: Figure 5 from Thomson *et al.* (2010), showing gas levels (in ppm) taken from two transformers in South Africa following the 2003 Halloween storm. Both transformers were removed from service approximately 6 months after the storm took place.

- The Low Energy Degradation Triangle,
- the Duval Triangle,
- and the Key Gas Ratio.

The Low Energy Degradation Triangle (LEDT) method was outlined in Moodley *et al.* (2017). The LEDT is unique amongst other DGA methods as it aims to predict a fault before it occurs, rather than diagnosing a fault once the transformer has become damaged. It is noted in the paper that ethane, ethylene and acetylene are unsuitable as indicators of low energy degradation as the processes that release them occur at higher energies. Methane, hydrogen and carbon monoxide

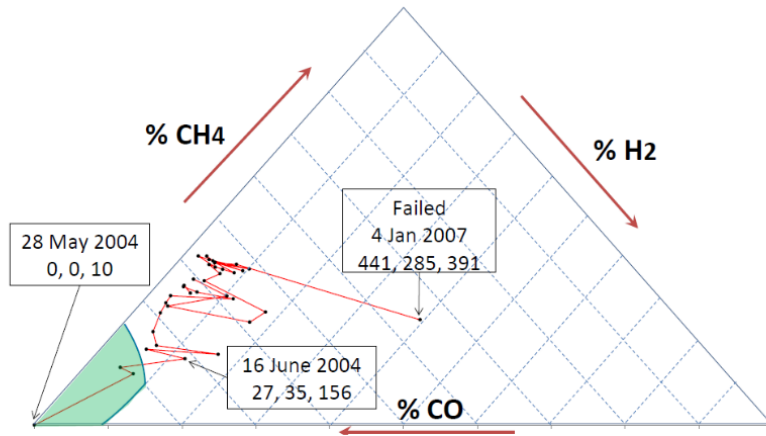
are produced in the oil and paper insulation during low energy processes, so are more suitable for this analysis. The LEDT method then combines the percentage contributions of three gas concentrations on a triangular plot. Note the three concentration percentages must sum to 100%, so there are only two degrees of freedom and they may be plotted in two dimensions. Such a diagram is called a *ternary plot* (Stover, accessed 22nd July 2021). Several equivalent methods exist to read values from such a plot, the most straightforward being the *perpendicular line* method, where lines are drawn from the data point to each side of the triangle, perpendicular to each side. The relative lengths of these perpendicular bisectors then give the value of each quantity.

In the LEDT, one vertex corresponds to ‘normal’ operation of the transformer and any movement away from this normal region corresponds to early indication of a fault. The distance from the origin (at the bottom left corner of the triangle) indicates the severity of the degradation, and the angle between the horizontal and the line connecting the origin to the data point indicates the energy.

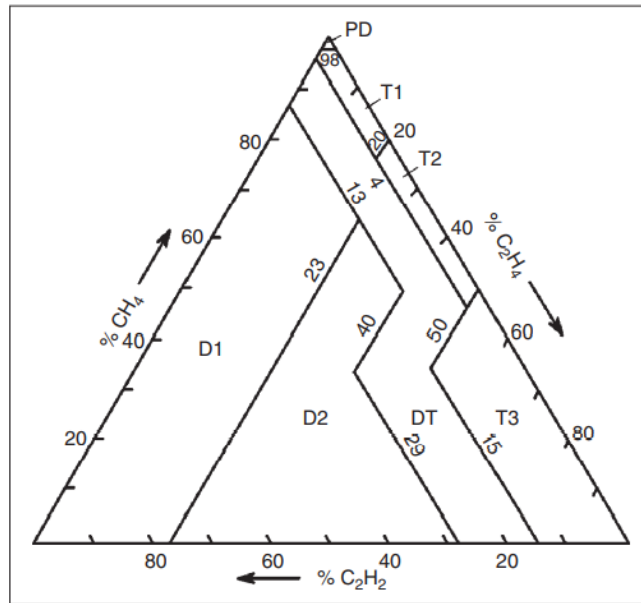
In Figure 9a, an example of an LEDT is shown from Moodley *et al.* (2017). The data can be seen to progress away from the normal region over time, from May 2004 until January 2007 when the transformer eventually failed. This gradual decline in transformer health could not be so easily observed by other DGA methods, such as the Duval triangle.

The Duval triangle (Duval, 2002) (Figure 9b) is an older and more widely established method in diagnosing existing transformer faults. Similar to the LEDT, three gases are plotted on a ternary plot: methane, acetylene and ethylene. There are 7 different regions in the triangle corresponding to 7 fault types. These are: partial discharge (PD), low energy discharge (D1), high energy discharge (D2), thermal faults less than 300°C (T1), thermal faults less than 700°C (T2), thermal faults greater than 700°C (T3) and mixtures of electrical and thermal faults (DT). It must be noted that no ‘normal region’ exists in the Duval Triangle, so the method is best used retrospectively when there is already knowledge of a fault having occurred (Sun *et al.*, 2012). This avoids false positives in fault diagnosis.

Finally, the Key Gas Method simply compares the relative proportions of the 6 key gases (Figure 10). Different ratios of the gases correspond to the four most common fault types, devised according to empirical data. This is the simplest of



(a) Case study example of the Low Energy Degradation Triangle (Figure 6 from Moodley *et al.* (2017))



(b) Duval Triangle (Figure 1 from Duval (2002))

Figure 9

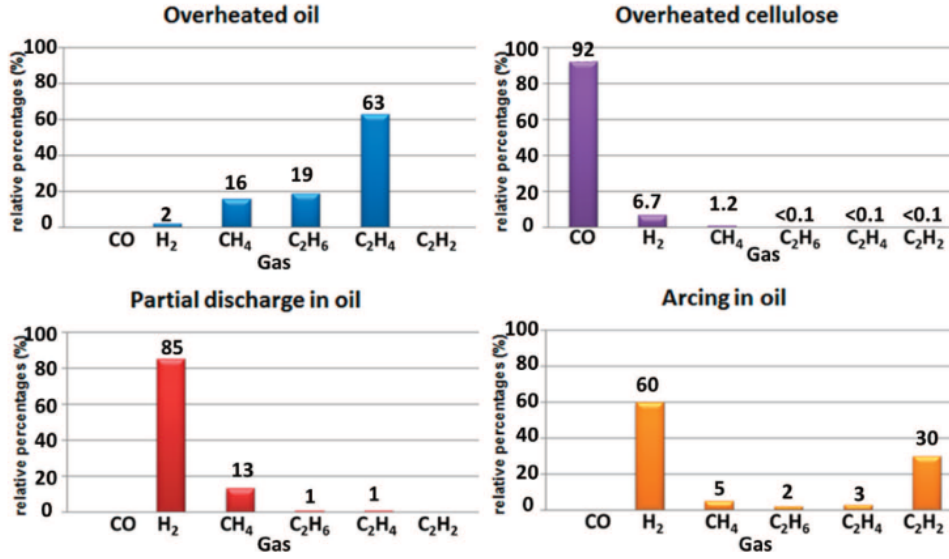


Figure 10: Typical key gas ratios for the four most common fault types (Bakar *et al.*, 2014)

the methods considered here, however it is noted in Bakar *et al.* (2014) that studies show only 42% of Key Gas Method fault diagnoses to be accurate.

All of these methods are empirical in nature, and must be applied carefully. The LEDT method is the most appropriate for this study as it looks to identify ‘low energy’ degradation; to assess whether a fault is likely to occur in the future rather than to diagnose a fault once it has already happened. We will however examine the results of the Duval and Key Gas methods as supplementary evidence.

## 2 Data

### 2.1 Time period studied

As discussed in section 1.1, the time period studied in this work was 2010–2015, due to the availability of the transformer DGA data. This five-year period lies in solar cycle 24 (shown in Figure 2), extending from December 2008 to January 2020.

Figure 11 shows a simple superposed epoch analysis for the number of sunspots (top) and the number of hours per year for which the recorded Dst was less than

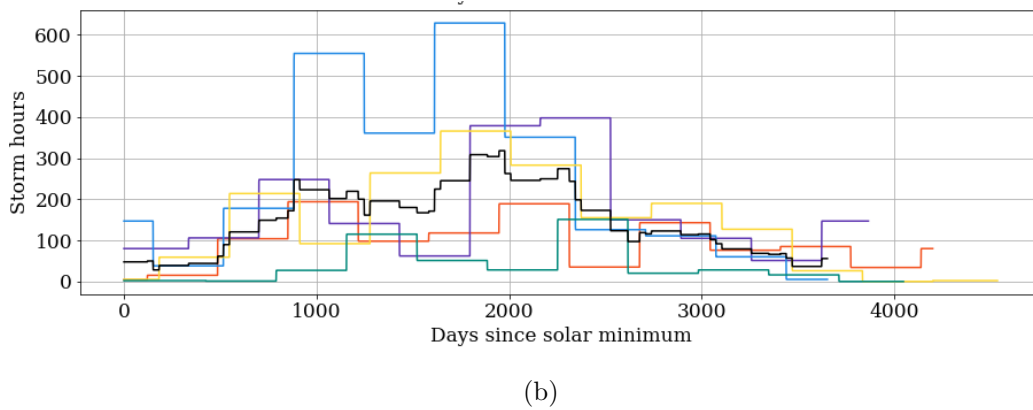
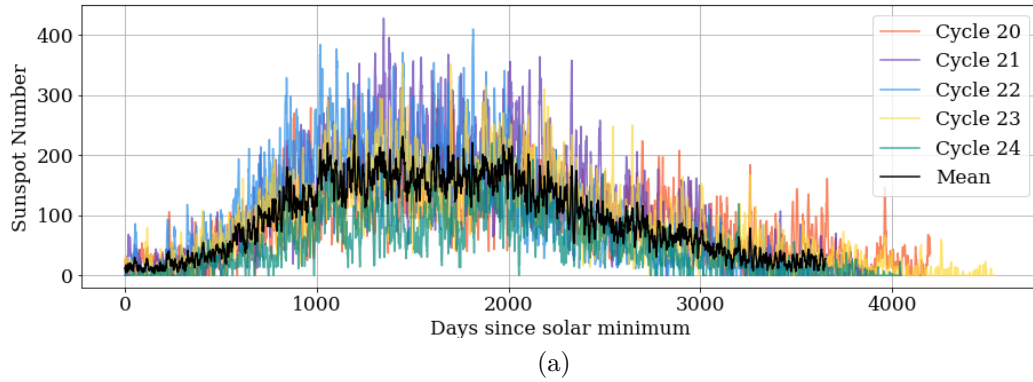


Figure 11: Sunspot number (a) and the number of hours where  $Dst < -80$  nT (b) for each solar cycle, plotted as a function of number of days from solar minimum. The black line shows the mean for the 5 solar cycles (20–24). Colour key the same for both figures.

$-80$  nT (bottom) during the last 5 solar cycles.  $-80$  nT is chosen to be in line with the threshold for geomagnetic storm selection in Walach *et al.* (2019), and later in this study.  $Dst$  is an hourly index, and the number of hours for which the  $Dst$  lies below this threshold (‘storm hours’) can act as a proxy for the number of hours per year spent during a geomagnetic storm. In both figures, the green line shows solar cycle 24 and the black line shows the mean over 5 cycles as a function of the number of days since solar minimum. It can be seen from these plots that solar cycle 24 is significantly below the mean in terms of both sunspot number and ‘storm hours’. This should be taken into consideration when interpreting the results of this study.

## 2.2 Space weather data

### 2.2.1 Rate of change of horizontal magnetic field component

Raw horizontal  $B$  field measurements are taken at magnetometer stations around the world (see Figure 6), and the data are collated and provided by SuperMAG (Gjerloev, 2012). In this study, the magnetometer stations used were Eskdalemuir (Southern Scotland) and Hartland (Devon).  $\left|\frac{dB}{dt}\right|$  was then calculated from the two horizontal components using the same generally accepted method as outlined in Rogers (2020);

$$\frac{dB}{dt} = \frac{1}{\Delta t} \sqrt{(\Delta B_N)^2 + (\Delta B_E)^2}, \quad (2)$$

where  $B_N$  and  $B_E$  are the northward and eastward components of the geomagnetic field respectively. It must be considered how suitable  $\frac{dB}{dt}$  is as a predictor of GIC activity, because detailed GIC measurements weren't routinely taken at transformer sites during the time period.

$\frac{dB}{dt}$  is frequently used in place of GIC measurements. In Rodger *et al.* (2017), it is shown that the correlation between this value and measured GICs is strong, with an  $R^2 = 0.88$ , at least in New Zealand where the study took place. It is reasonable to assume that this correlation will be similarly strong for the UK. This implies that it is appropriate to use calculated  $\frac{dB}{dt}$  values from the ground-based magnetometer readings to determine when the transformers are most at risk of GIC damage. However, magnetic field changes and GIC values are highly localised, and the study in Rodger *et al.* (2017) found a strong correlation for  $\frac{dB}{dt}$  and currents measured at the same location. Given that the transformers used in this study are at 13 different locations around the coastal regions, a more rigorous study would use the available magnetometer measurements and extrapolate GIC estimates using ground conductivity survey data. An example of this analysis is detailed in Beggan *et al.* (2013).

Figure 12 shows the locations of the two main SuperMAG magnetometer stations used in this work. These represent the only two stations on mainland Great Britain that were operational during the time period studied. At the time of writing, the magnetic latitude of Eskdalemuir was  $52.86^\circ$ , and the magnetic latitude of Hartland was  $48.12^\circ$ . Figure 13 then shows the measured rate of change of the horizontal geomagnetic field, as measured at each station and calculated using equation 2 for solar cycle 24. It can then be seen that the  $\frac{dB}{dt}$  values measured at Eskdalemuir generally reach much higher magnitudes than in Hartland, due to its higher geomagnetic latitude and greater proximity to the auroral oval. During solar cycle 24, the maximum magnitude of  $\frac{dB}{dt}$  measured at Eskdalemuir was 103.44 nT/min, and 67.71 nT/min at Hartland. The mean values at Eskdalemuir

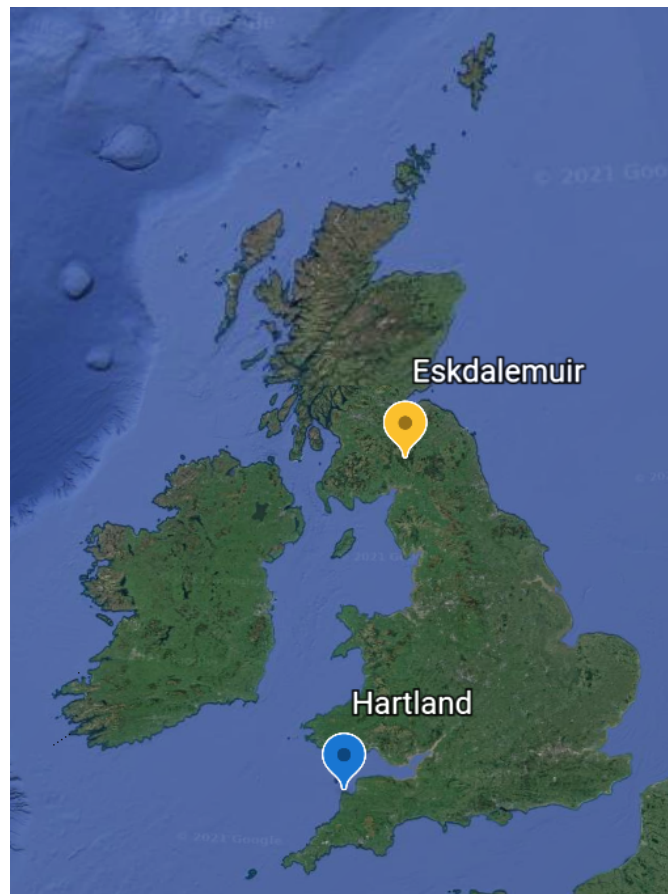
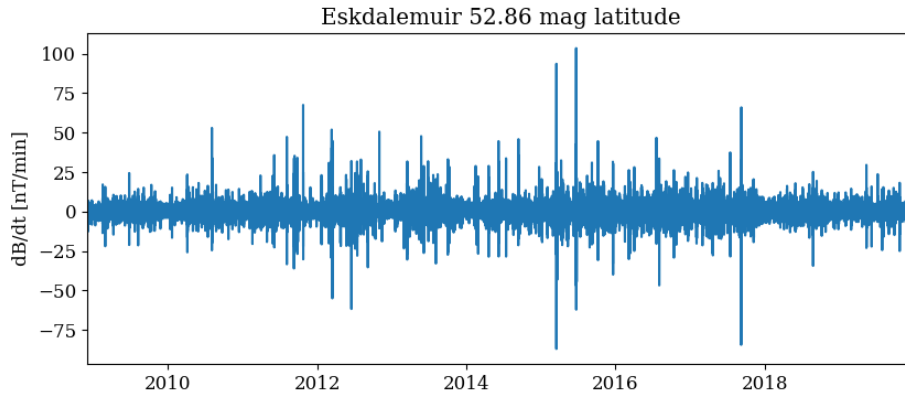
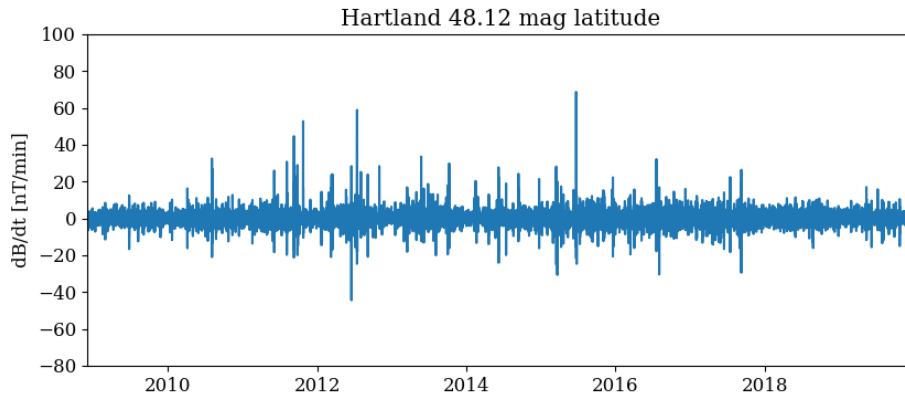


Figure 12: Satellite image showing the location of two magnetometer stations, Eskdalemuir and Hartland. *Google Earth V 9.135.0.3 (Accessed 26th May 2021)*



(a) Eskdalemuir



(b) Hartland

Figure 13: Time derivative of horizontal component of geomagnetic field as measured at two magnetometer stations.

and Hartland were 0.57 nT/min and 0.38 nT/min respectively.

It can also be seen from Figure 13 that the thresholds for infrastructure risk cited in Weygand (2021) and mentioned in section 1.4.1 (90 nT/min and 300 nT/min) were never reached at Hartland during this time, and only once was the 90 nT/min threshold reached at Eskdalemuir. This suggests that the levels of magnetic field change in the UK during the time period studied are unlikely to be of immediate risk to transformers. This is not surprising considering the quiet nature of solar cycle 24. We are therefore not expecting to see transformer failure directly related to a space weather event in this analysis, rather looking for gradual changes in

transformer health that can be linked to increased geomagnetic activity. However, it must be noted that these two thresholds have a large difference between them, and the true threshold for GIC risk is likely to change depending on many of the factors previously discussed; such as the design of the transformer and geometry of the network.

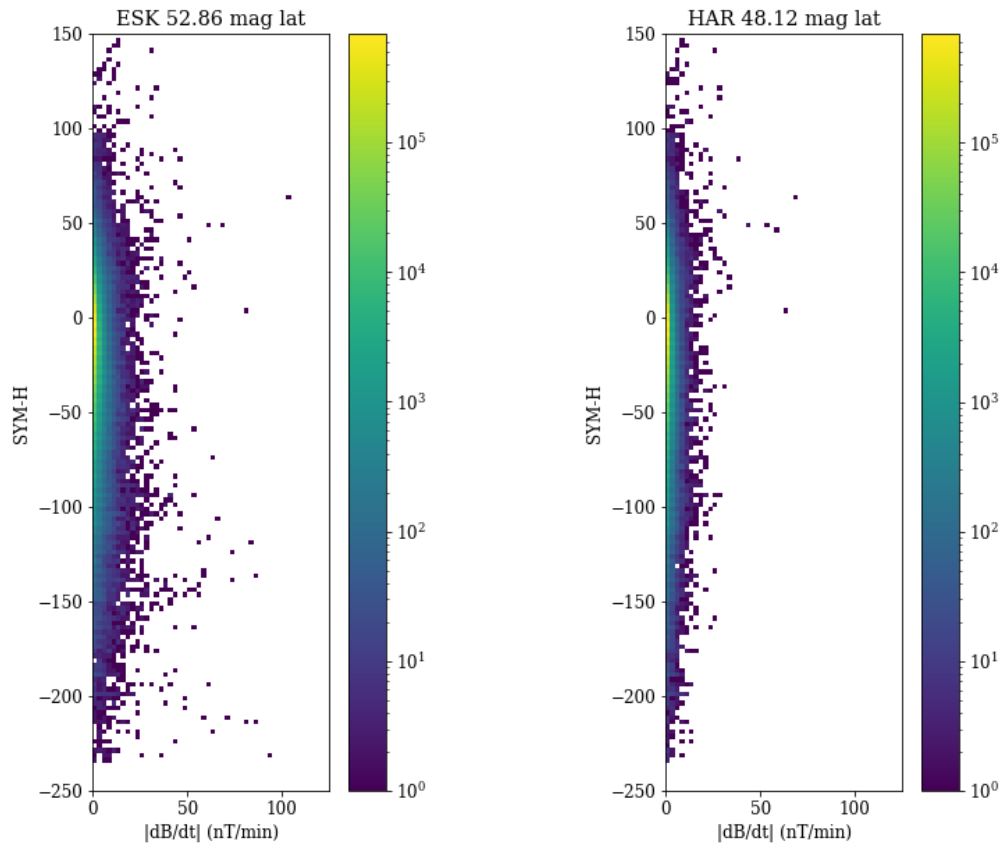
### 2.2.2 SYM-H

In this project, SYM-H was used to determine storm events as a measure of global ‘storminess’. However, we know that  $\frac{dB}{dt}$  is likely to be a better indicator of infrastructure risk, due to its strong correlation with GIC size and locally calculated values. For that reason, the strength of the correlation between the two measures was examined.

Global SYM-H data are provided by the World Data Center for Geomagnetism, Kyoto. Figure 14 shows heatmaps for SYM-H and  $\left|\frac{dB}{dt}\right|$  values for the whole of solar cycle 24 (December 2008 – May 2020). The density of points in each bin (pixel) is shown by the colour gradient on the right hand side of the plot. These plots indicate that the size of the measured change in the geomagnetic field is generally much higher at Eskdalemuir than at Hartland, as also demonstrated in Figure 13. In addition, it can be seen from these figures that the highest magnitudes of  $\frac{dB}{dt}$  at Eskdalemuir occur with low SYM-H, and at Hartland with high SYM-H. At Eskdalemuir, this suggests that in general the highest rate of change in the geomagnetic field occurs between the main and recovery phases of the storm (where SYM-H is at its minimum), whereas at Hartland high  $\left|\frac{dB}{dt}\right|$  is more likely to occur alongside the peak SYM-H of storms (the initial phase).

To further investigate the difference between Eskdalemuir and Hartland, the analysis was expanded to more magnetometer stations, over a wider range of magnetic latitudes. The stations were chosen to be mainly around similar longitudes, and to cover a range of latitudes between and around Eskdalemuir and Hartland, with some more extreme latitudes chosen for comparison.

The results are shown in Figure 15. The top left panel shows a histogram of all the SYM-H values recorded during solar cycle 24 (red), and the distribution of SYM-H values below  $-80$  nT (yellow).  $-80$  nT was chosen as it is the threshold



(a) Eskdalemuir

(b) Hartland

Figure 14: Heatmap showing relation between SYM-H and  $\left|\frac{dB}{dt}\right|$  as measured at two magnetometer stations. Gradient shows the density of points in each bin.

for storm identification used in Walach *et al.* (2019). The other 11 plots show 11 magnetometer stations, in order of increasing magnetic latitude. Each plot shows the distribution of SYM-H values for which the coincident  $\frac{dB}{dt}$  value was above the 99th percentile (blue) and the 99.99th percentile (orange). The distribution of SYM-H points for which  $\left|\frac{dB}{dt}\right|$  was above the 99.99th percentile can be seen to shift towards lower, more negative values as the magnetic latitude increases. These findings echo the results of Smith (2020) and Smith *et al.* (2021).

Smith (2020) compares the proportions of high  $\left|\frac{dB}{dt}\right|$  that can be attributed directly to sudden commencements (SCs) at three UK magnetometer stations (Hartland, Eskdalemuir and Lerwick) between 1996 and 2016. They found that although only 8% of significant  $\left|\frac{dB}{dt}\right|$  ( $\geq$  99.99th percentile) are attributed to SCs at Hartland, this still represents the greatest shift in  $\left|\frac{dB}{dt}\right|$  relative to normal for the three stations considered. In other words, the greatest fraction of extreme  $\left|\frac{dB}{dt}\right|$  related to SCs was at Hartland. SCs, when they precede a geomagnetic storm, are referred to as Storm Sudden Commencements (SSCs). In the SYM-H timeseries, this relates to the peak in nT observed during the initial phase of the storm. Therefore, it is expected that at stations where a larger proportion of extreme  $\left|\frac{dB}{dt}\right|$  values are due to SCs and SSCs, when comparing the magnetic field rate of change and the SYM-H measured, higher  $\left|\frac{dB}{dt}\right|$  would correspond to higher positive SYM-H values. Hence the shift in the SYM-H distribution at these stations in Figure 15.

This pattern breaks at Qaanag, which lies at 85.35 degrees North. This may be due to the effects beyond the auroral oval at this latitude.

In general, this comparison of SYM-H and the magnetic field change shows that it is not appropriate to assume that SYM-H and  $\frac{dB}{dt}$  follow the same patterns. The largest space weather events in SYM-H will not necessarily have the most significant magnetic field change associated with them, nor the largest GIC values. In addition, the relationship between the two measures is not constant as latitude changes. Figure 14 shows that SYM-H is not well correlated with  $\frac{dB}{dt}$  at either Eskdalemuir or Hartland, and that the behaviour of the geomagnetic field changes as a result of differing latitudes. The transformers used in this study are located at various sites around the UK, in both Scotland and England, therefore it will not be assumed that the GICs at all sites will be correlated well with global SYM-H and  $\frac{dB}{dt}$  at a specific station. The event lists produced in the next section will therefore

be generated using Hartland, Eskdalemuir and global SYM-H measurements, and cross-compared.

### 2.3 Storm identification

The time period analysed for this study was 2010–2015. A list of storms within this period needed to be found, firstly by looking at the variation of global SYM-H values during this time.

All the SYM-H values for 2010–2015 were combined in a distribution plot (Figure 16), and the threshold for the lowest 1% marked with a vertical line. This corresponded to a SYM-H value of  $-70$  nT. This was then compared with the method outlined in Hutchinson *et al.* (2011 and Walach *et al.* (2019), where a threshold of  $-80$  nT was used to identify a storm. This corresponds to the lowest 0.64% of values between 2010 and 2015. Comparing the produced storm list for each threshold found the lower limit to produce fewer duplicate storms and doubtful storm events, so this threshold was selected.

An algorithm was then implemented to identify the storms. First, a table of SYM-H values below the  $-80$  nT threshold was created. Then, a list of all storm ‘start times’ was defined as the timestamp every time the SYM-H trace dropped below the threshold. Each ‘start time’ was then iterated over, to collect the SYM-H values for 24 hours before and 24 hours after the drop below the threshold. This created a list of 48-hour long SYM-H traces, centred on the ‘start time’. This method produced many duplicates, where the storm trace crossed the  $-80$  nT threshold multiple times during the event. This duplicate number was reduced by removing storms where the start time happened on the same calendar day, though several duplicates still remained, to be removed by eye. Therefore, throughout the rest of this project the storm list provided by Maria Walach in line with Walach *et al.* (2019) was used, so that the results could be more readily compared with previous publications. From this list, 48 storms were found to have occurred between January 2010 and December 2015. The ten storms with the most extreme minima in SYM-H values were then selected to be used as case studies for the DGA section of this project.

Next, an event list was produced for the 10 largest events in terms of the change

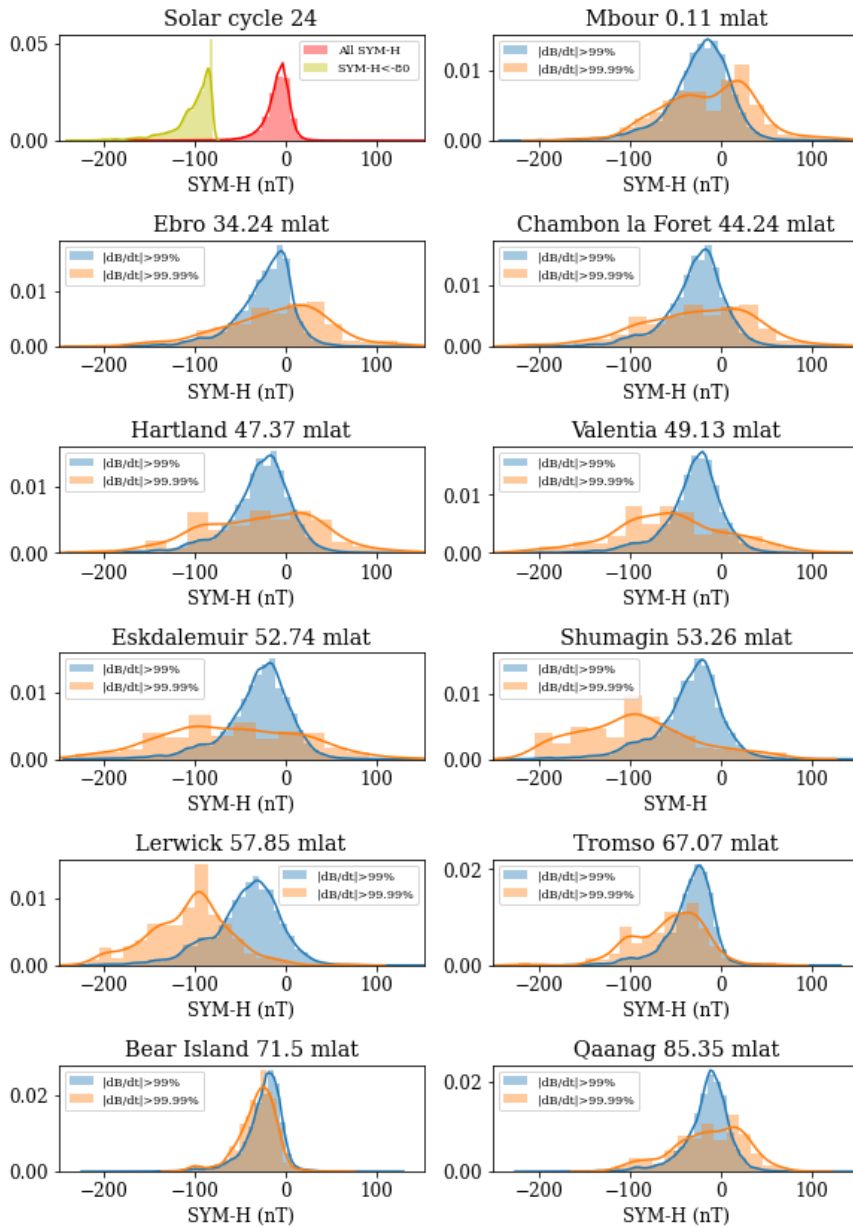


Figure 15: Top left shows a histogram of the distribution of SYM-H values (red) and SYM-H values less than -80 nT (yellow) for the entirety of solar cycle 24. Other plots show histograms of the distribution of SYM-H values when  $\left|\frac{dB}{dt}\right|$  is in the top 99% (blue) and top 99.99% (orange), for 9 magnetometer stations at different magnetic latitudes.

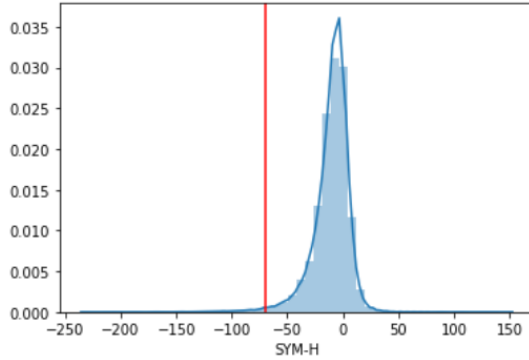


Figure 16: Distribution plot of all SYM-H values 2010–2015, with lowest 1% threshold marked at  $-70$  nT.

in the horizontal magnetic field measured at Eskdalemuir and Hartland. Instead of taking the 10 largest values with 1 minute resolution, the magnetometer data were resampled to produce a mean  $\left|\frac{dB}{dt}\right|$  for each half hour interval. This was chosen because a very high change in the magnetic field over a one minute period is less likely to be impactful to infrastructure than moderately high changes over a more extended time frame. The resulting event lists are shown in Appendix A. The ‘SYM-H’ column shows the dates and times of the 10 most significant events in SYM-H, with their corresponding minima in nT shown in the next column (‘min SYM-H’). The columns labelled ‘Eskdalemuir’ and ‘Hartland’ show the dates and times of the largest mean  $\left|\frac{dB}{dt}\right|$  in the preceding half hour interval, with the values of that half-hour mean in the corresponding ‘mean  $\left|\frac{dB}{dt}\right|$ ’ columns. It can be seen that the two largest storms in SYM-H (17th March 2015 and 23rd June 2015) also rank in the top three events with the magnetometer readings. There is more variation in the events which appear lower down the lists. As predicted by the comparison of SYM-H with the two magnetometer stations, the lists from Hartland and Eskdalemuir are not as similar as one might expect.

## 2.4 Dissolved Gas data

In this study, DGA data were analysed from 13 UK power station transformers. The data includes three AC phases offset from each other by  $120^\circ$ , but for simplicity only one phase has been considered in this work. The data generally cover the

Transformer	Data range
A	7 August 2014 – 9 July 2015
B	10 January 2011 – 18 May 2015
C	14 September 2010 – 9 July 2015
D	2 July 2010 – 9 July 2015
E	9 July 2010 – 9 July 2015
F	9 July 2010 – 9 July 2015
G	9 July 2010 – 9 July 2015
H	9 July 2010 – 9 July 2015
I	29 July 2013 – 9 July 2015
J	9 July 2010 – 9 July 2015
K	27 September 2010 – 9 July 2015
L	4 June 2011 – 9 July 2015
M	30 October 2013 – 9 July 2015

Table 1: Summary of DGA data available for 13 anonymised transformers (A–M)

period 2010–2015, however the range covered by each transformer differs and can be seen in Table 1. The transformers have been anonymised, and typical data for an example transformer (E) is shown in Figure 17 Gas data for all other transformers are shown in Appendix B. The six gases shown are the ‘key’ gases used in DGA: methane, ethylene, ethane, hydrogen, acetylene and carbon monoxide. Values for the concentration in ppm are automatically recorded three times every 24 hours.

Figure 17 shows a general upwards trend on a multi-year timescale, with breaks in the data where either data gaps exist or where the concentrations ‘reset’ to a lower value. This pattern is indicative of maintenance or oil replacement work carried out during this time.

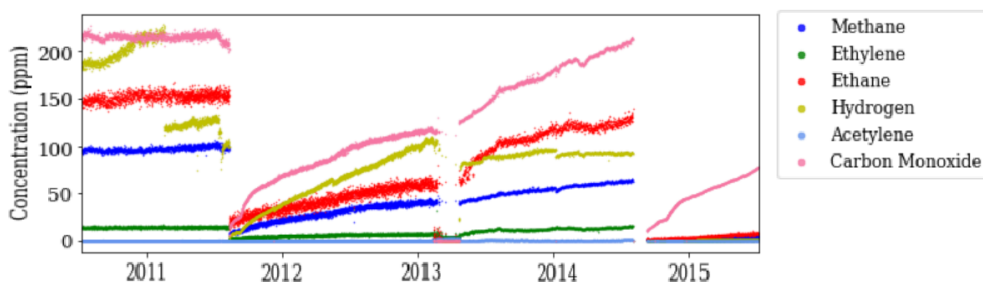


Figure 17: Typical gas concentrations for transformer E

### 3 Dissolved Gas Analysis

Figure 17 illustrates the difficulty in analysing DGA data. There is significant noise and gaps in the data, and it is difficult to interpret in its raw form. For this reason, DGA methods are used to understand the state of the transformer; to determine whether faults are likely to occur or to diagnose a fault after the fact.

However, it is instructive to first look at the general trends in the gas concentrations during storm events. The most significant storm event during this five year period was that on St Patrick’s day in March 2015. This storm was the largest in solar cycle 24, and reached a minimum Dst value of  $-222$  nT (Mukhtar *et al.*, 2020). Minimum SYM-H was reached at 22:47 on the 17th March (see Appendix A). This event also led to the largest  $\frac{dB}{dt}$  values measured at Eskdalemuir, with a 30 minute mean of 29.24 nT/min between 22:30 and 23:00 on the 17th March. The change in the magnetic field at Hartland was less significant, but still the third largest 30 minute mean across the 5 year period was measured between 17:00 and 17:30 on the 17th March, at 10.50 nT/min (see Appendix A).

Figure 18 shows the gas levels in each transformer from the 15th until the 23rd March. The yellow shaded region marks the initial phase of the storm and the red shaded region shows the main phase. The green region shows the recovery phase. The results for all transformers show that despite the large variability in the concentrations on a multi-year scale (see Figure 17), for a shorter time window they are largely extremely stable, with an upwards trend not usually visible on this scale. Exceptions are transformers C and L, which show a gradual increase in carbon monoxide levels, which seem unaffected by the storm onset. Note also a gap in the data for transformer G around the 13th March, followed by an abrupt decrease in all gas levels, but particularly in carbon monoxide. In general, there also appears to be no increase in the rate of gas production during any phases of the storm. For the majority of the transformers, the gas with the highest concentration is carbon monoxide, but the actual magnitude of this concentration varies from less than 1 ppm to 500 ppm.

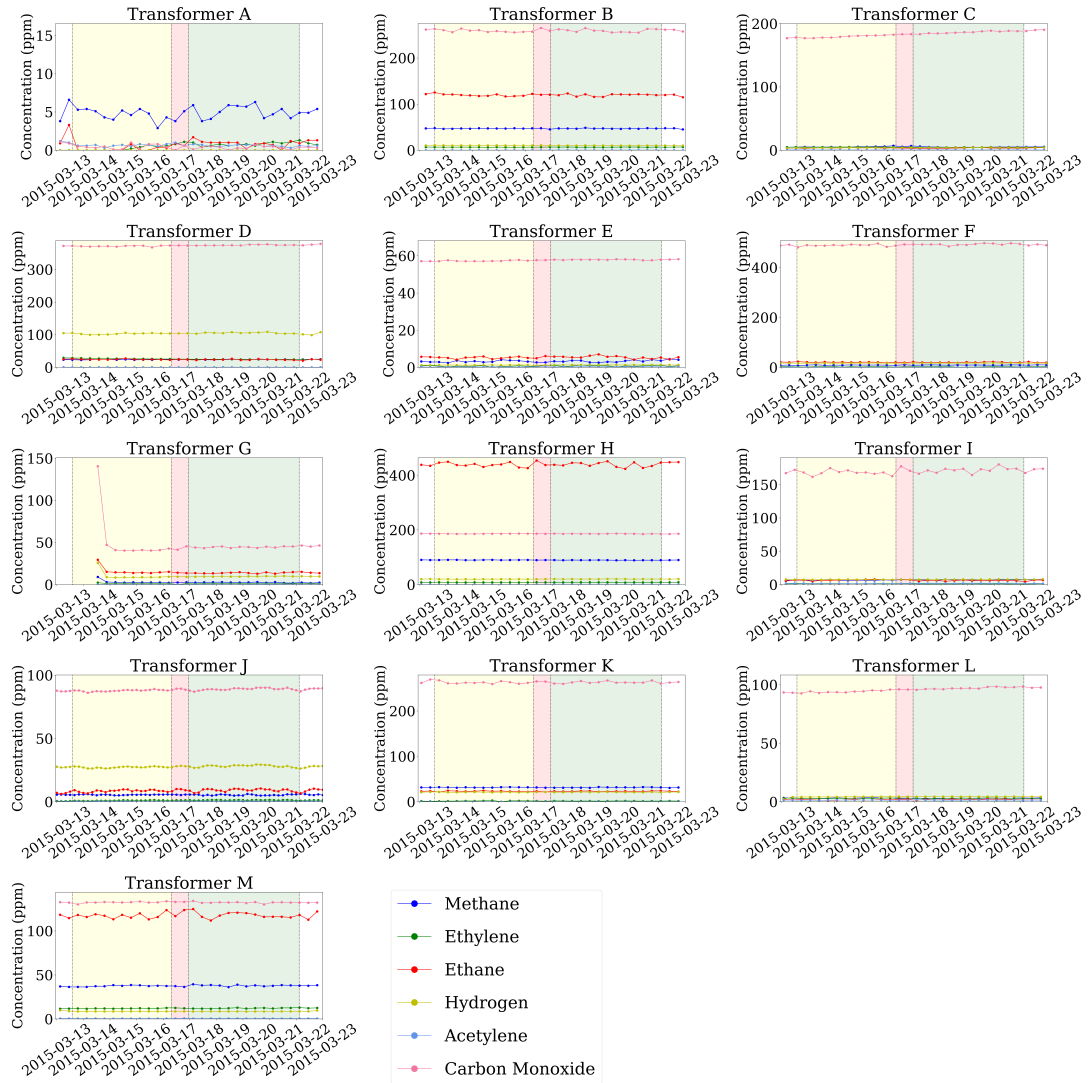


Figure 18: Dissolved gas levels for each of the 13 transformers, including all 6 key gases. The yellow, red and green shaded regions show the initial, main and recovery phases of the storm respectively.

## 3.1 LEDT

### 3.1.1 Method

The LEDT plots were produced as follows. First, the raw concentrations of carbon monoxide, hydrogen, and methane at each timestamp were summed, and the contribution of each gas as a fraction of this sum was calculated. The  $x$  and  $y$  coordinates to be plotted were then calculated as follows:

$$x = 1 - \frac{[\text{CO}]}{[\text{CO}] + [\text{CH}_4] + [\text{H}_2]} - \frac{1}{2} \frac{[\text{CH}_4]}{([\text{CO}] + [\text{CH}_4] + [\text{H}_2])}, \quad (3)$$

$$y = \frac{\sqrt{3}}{2} \frac{[\text{CH}_4]}{([\text{CO}] + [\text{CH}_4] + [\text{H}_2])}. \quad (4)$$

Where  $[\text{CO}]$  indicates the concentration in ppm of carbon monoxide,  $[\text{H}_2]$  for hydrogen, and  $[\text{CH}_4]$  for methane. The  $x$  and  $y$  coordinates were then combined to give the polar coordinates  $R$  and  $\theta$  in the usual way:

$$R = \sqrt{x^2 + y^2}, \quad (5)$$

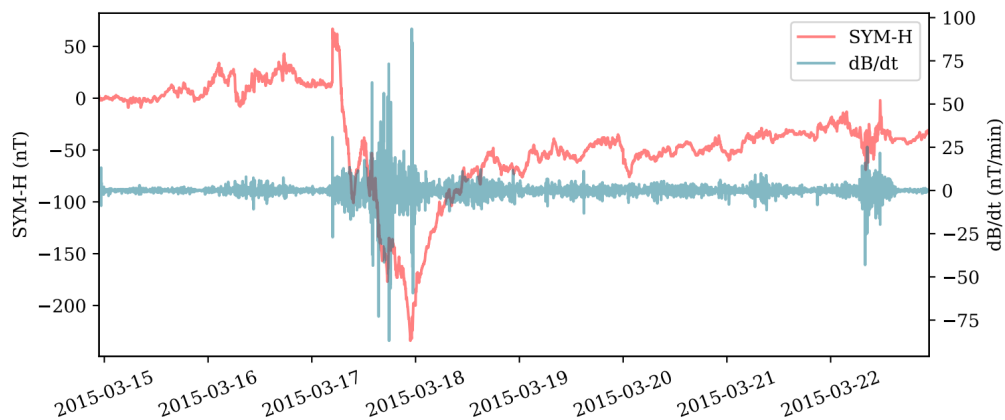
$$\theta = \arctan \frac{y}{x}. \quad (6)$$

The ‘R index’, given by equation 5 is then a useful measure of a transformer’s distance from the normal region, showing the level of degradation in the insulation. It measures the distance from the origin in the bottom left corner of the plot. The far edge of the normal region corresponds to an R value of 0.175 and values of R larger than this will indicate an increased likelihood of transformer failure.  $\theta$  (equation 6) represents increasing fault energy. The data were then plotted in this manner for each gas reading taken (at approximately eight-hour intervals). The further from the origin the data lie, the higher the probability of failure.

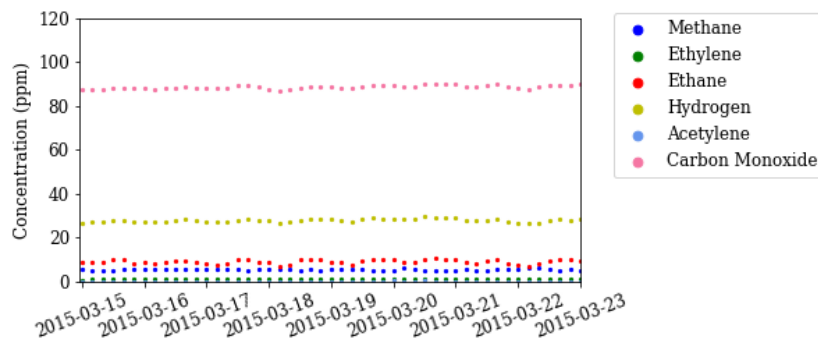
An LEDT was plotted for each of the 13 transformers, for each of the events in Appendix A. The following sections show case studies for the transformer behaviour during three of these events.

### 3.1.2 Case study 1

Shown in Figure 19a are  $\frac{dB}{dt}$  and SYM-H, again for the St Patrick's Day storm in March 2015. The sudden storm commencement (SSC) can be observed by the increase in SYM-H around 00:00:00 on 17 March, with the ground magnetometer  $\frac{dB}{dt}$  readings increasing in magnitude correspondingly, as the ring current becomes enhanced and alters the global magnetic field as a result. Figure 19b shows the dissolved gas measurements in transformer J for the same time period. Little to no change can be observed in the gas data as the storm progresses, suggesting that the rate of gas production due to heating in the transformer is unaffected by the presence of heightened geomagnetic activity.



(a) Horizontal component of  $\frac{dB}{dt}$  as measured at Eskdalemuir (blue, right axis) and global SYM-H index (red, left axis) plotted for the storm period during the March 2015 'St Patrick's day' storm.

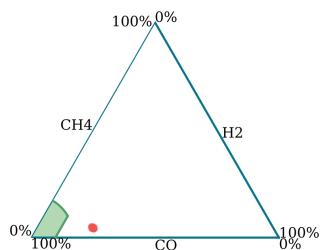


(b) Raw gas data for the same time period, for the 6 key DGA gases in transformer J.

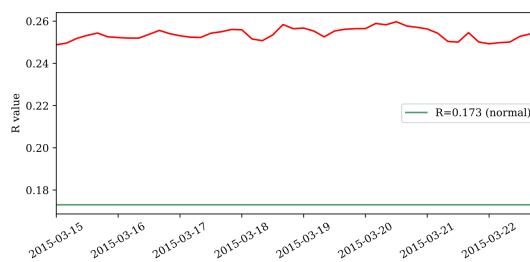
Figure 19: Case study 1

Figure 20 shows the LEDT (plotted for 72 hours before and 120 hours after the

minimum value of SYM-H, the same time period as shown in Figure 19) alongside the degradation R index. The degradation R index refers to the polar coordinate of distance from the origin, where  $R = 0.175$  marks the limit of the normal region. The LEDT shows the transformer to be operating away from the normal region (though not drastically). However the location on the triangle is stable throughout the storm period (appearing almost as a single point) and does not progress further away from the normal region during this time.



(a) LEDT for transformer J, 15th–22nd March 2015. The green shaded area denotes the region of typical ‘normal’ operation of the transformer.



(b) R index. The green line shows the value of R at the boundary of the normal region.

Figure 20: Case study 1

### 3.1.3 Case study 2

Figure 21 shows the second largest storm studied, reaching a minimum SYM-H of  $-208$  nT on the 23rd June 2015. While less intense than the St Patrick’s day storm in terms of SYM-H, the  $\frac{dB}{dt}$  recorded at Eskdalemuir reaches almost 200 nT/min, so there was a more significant change in geomagnetic field. Figure 22 shows the LEDT analysis for another transformer (F) during this time. In this example, the data plotted stays within the normal region at all times before and after the storm, again with very little movement. The R index in Figure 22b shows that the gas concentrations were very stable during this time. It is clear that the storm had no effect on the transformer health, at least for this window.

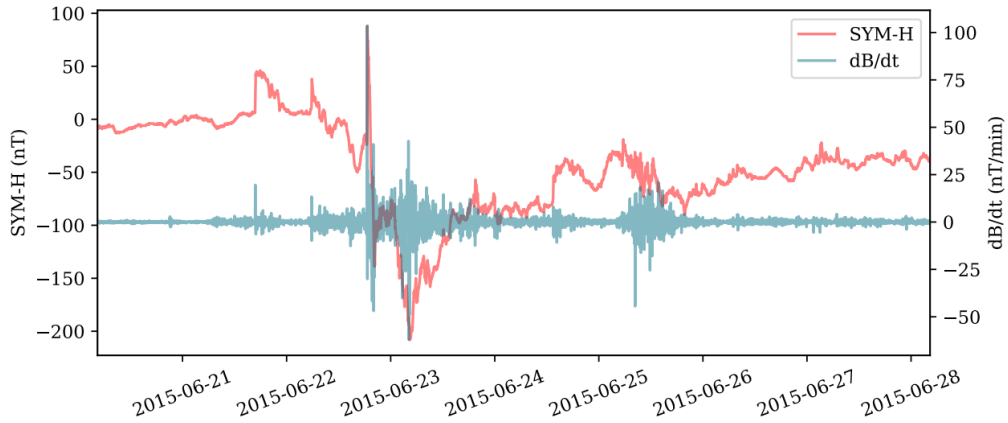


Figure 21: Horizontal component of  $\frac{dB}{dt}$  as measured at Eskdalemuir (blue, right axis) and global SYM-H index (red, left axis) plotted for the storm period June 2015

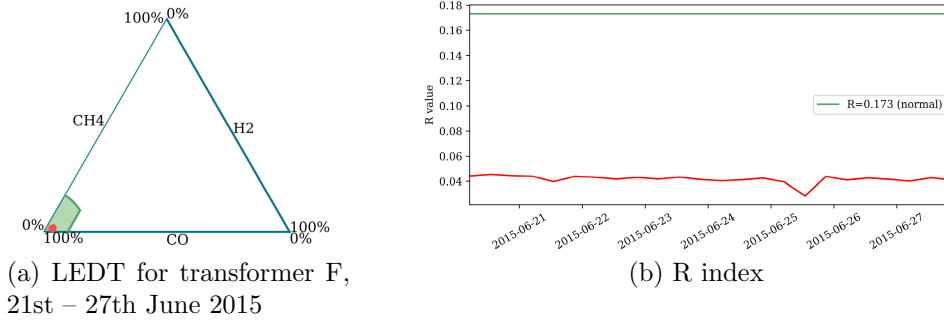


Figure 22: Case study 2

### 3.1.4 Case study 3

In a final case study, Figure 23 shows another storm which took place on 24th – 25th October 2011. The minimum SYM-H reached during this storm was  $-160$  nT. This example is interesting as the LEDT for transformer D in Figure 24a and R index in 24b shows a small movement away from the normal region during the recovery phase of the storm. This is possibly a direct effect of GICs in the transformer, but the change is very small ( $+0.006$  in the R index).

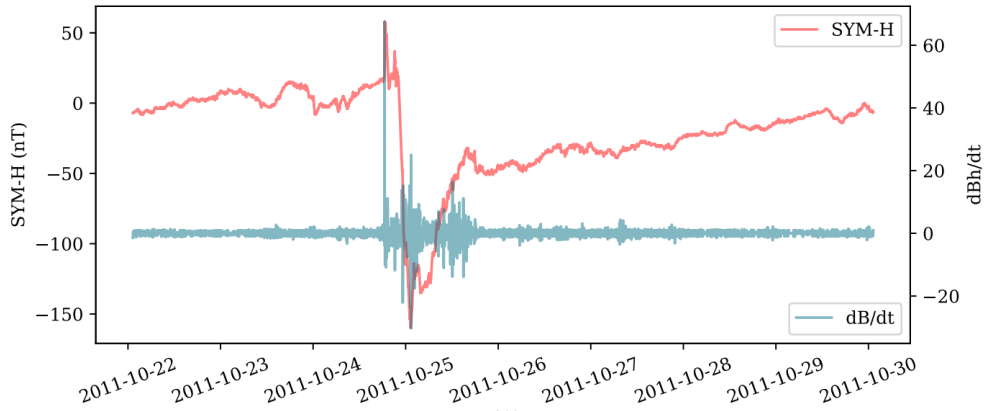
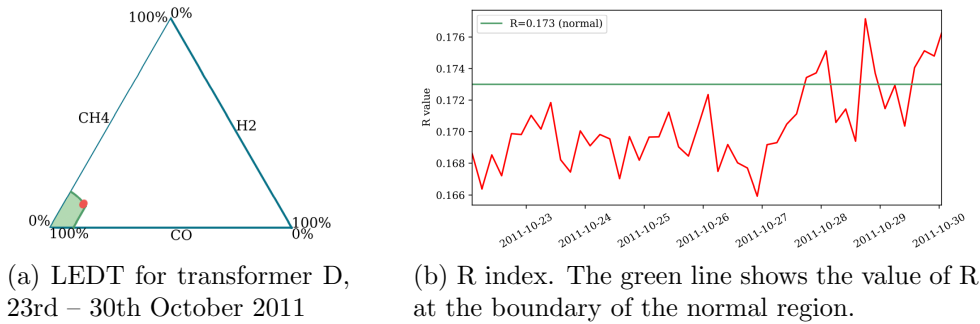


Figure 23: Horizontal component of  $\frac{dB}{dt}$  as measured at Eskdalemuir (blue, right axis) and global SYM-H index (red, left axis) plotted for the storm period October 2011



(a) LEDT for transformer D, 23rd – 30th October 2011

(b) R index. The green line shows the value of R at the boundary of the normal region.

Figure 24: Case study 3

### 3.1.5 Discussion

LEDTs for all transformers during each of the three storms in case studies 1, 2, and 3 are shown for completeness in Appendix C. Of the 98 transformer-storm combinations studied (not all transformers had data available for every storm), 63% of the LEDTs showed the transformer to be outside of the normal region throughout the entire storm period (similar to case study 1). This does not suggest that many of the transformers will develop a fault, but that as they move away from the normal region the probability of failure increases. This increased likelihood of failure does not appear to be linked to GIC activity, as in only 5% of cases studied did the LEDT plot show movement between the normal and abnormal regions during the storm period, and only 1 case (case study 3) showed

convincing movement out of the normal region after onset of the storm. Also, no faults were reported by the energy company during the time studied. Considering the number of cases studied, and small size of the observed change in the LEDT, this is not likely to be a significant result. However, in future work it would be worth a further analysis to ascertain where similar examples can be found outside the time period and transformer group studied in this project.

### **3.2 Duval triangle**

The Duval triangle method (Duval, 2002) was then applied to the same 10 storms and 13 transformers as the LEDT method. However, it is not appropriate to use this method in all cases, as there is no region on the Duval Triangle that corresponds to a healthy transformer. Therefore, a poorly considered approach to this method might indicate that all the transformers have a fault, but this would not be accurate. The most useful information to extract from the Duval triangle comes where the data moves between regions of the transformer i.e. is not stable in one region.

Figure 25 shows the Duval triangle for transformer D during the storm in October 2011 (case study 3). Figure 24 shows the transformer to be moving away from the normal region during the few days after the storm main phase has occurred. However, the Duval triangle for the same window appears to be very stable within the T3 (thermal fault above 700°C) region. The stability and lack of progression within the Duval triangle suggests that the transformer is not directly going on to produce a fault during this time.

For completeness, Figure 26 shows the Duval triangles for case studies 1 and 2. Again, the data are very stable, with movement between the T1 (thermal fault less than 300°C) and T2 (thermal fault less than 700°C) regions. There is nothing to suggest a fault is developing during the storm period, and indeed no fault was reported to have occurred.

### **3.3 Key Gas Ratio**

Figure 27 shows each gas plotted as a percentage of the sum of the total gas concentrations, again for transformer D. Comparing the relative gas quantities

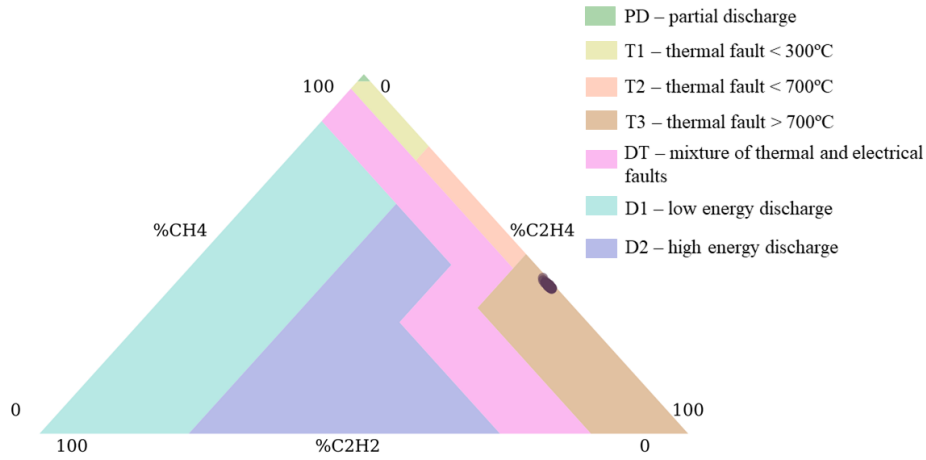
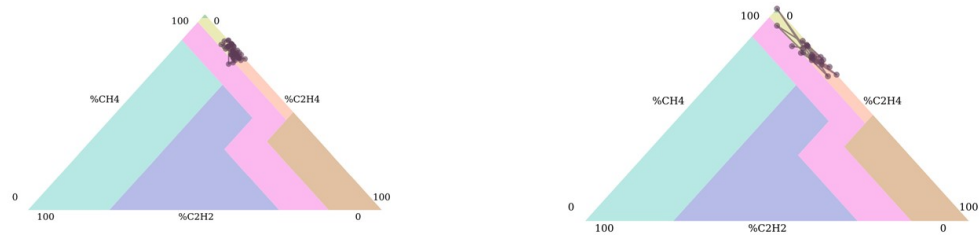


Figure 25: Duval triangle for case study 3 (storm maximum on 25th October 2011, transformer D).



(a) Duval triangle for case study 1 (storm maximum on 17th March 2015, transformer J).

(b) Duval triangle for case study 2 (storm maximum on 23rd June 2015, transformer F).

Figure 26: Duval triangles for case studies 1 and 2

with Figure 10 implies no particular faults within the transformer. At one reading during 2013, the fraction of hydrogen suddenly increases, resembling the conditions in Figure 10 for partial oil discharge. However these particular gas levels are very short lived, and therefore more likely to be an anomaly in the data than a sustained fault. It is also reassuring that, following October 2011, there is again no progression towards a fault state.

As previously noted, the Key Gas Ratio DGA method is empirical and considered to be only 42% accurate (Bakar *et al.*, 2014), however in this case it goes some way to confirm the results of the Duval triangle, and to imply that the storm on 25th October 2011 did not cause damage to transformer D.

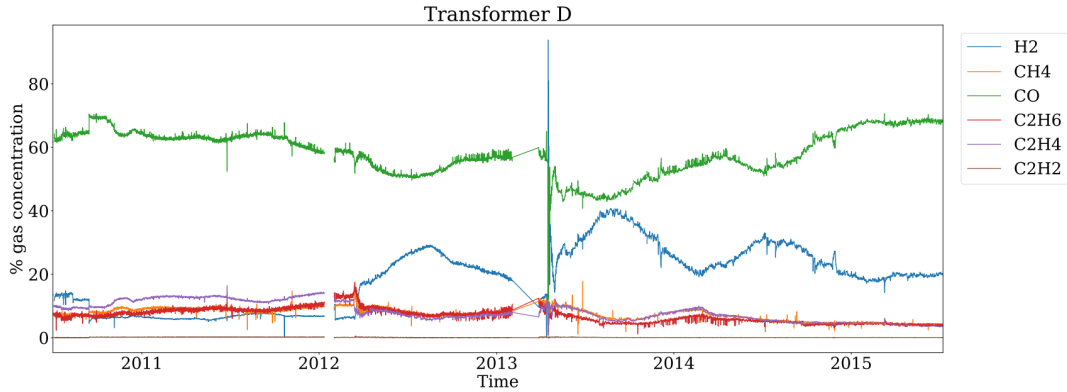


Figure 27: Percentage of total gas concentration plotted against time for the 6 key gases in transformer D.

## 4 Superposed Epoch Analysis

A superposed epoch analysis (SEA) was then performed on the dataset as a whole (Morley *et al.*, 2010), to ascertain whether any small but systematic gas changes could be seen in the gas data when averaged over multiple storm events. Figure 28 shows the SYM-H data superposed and lined up on the start of the main phase of the storm as defined in Walach *et al.* (2019). The black line shows the median, the red dotted line shows the mean, and the light blue shaded area shows the interquartile range. The six ‘key’ gases were then centred on the same epoch with 6 days either side, and plotted individually for each transformer. Figure 29 shows the results for a particular transformer. Thirty-three storms were included in this analysis, which reflects all the storms which occurred during the time period covered by data for this transformer (see Table 1). This example is for transformer C, but all transformers produced similar results. Appendix D shows the same analysis for each of the 13 transformers. Note the number of epochs used differs for each transformer due to the data availability. In particular, the superposed epoch analysis for transformer A (Figures 49 and 50) includes only 9 storms, and transformer M (Figure 61) includes 12.

These results show that generally the rate of production of the key gases does not increase following the main phase of a storm. The interquartile range is also large compared to the variation in the mean and median, owing to the noisy and

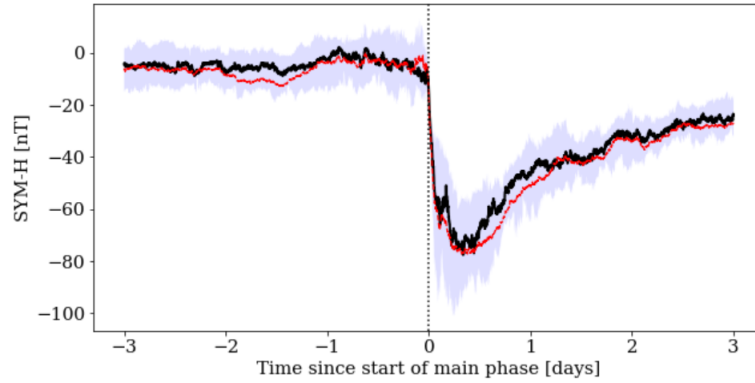
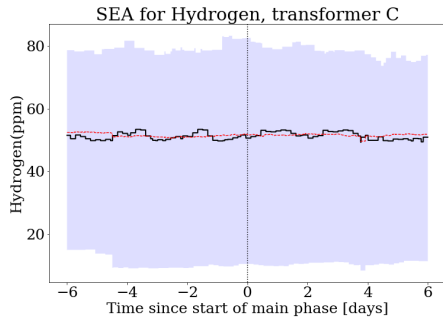


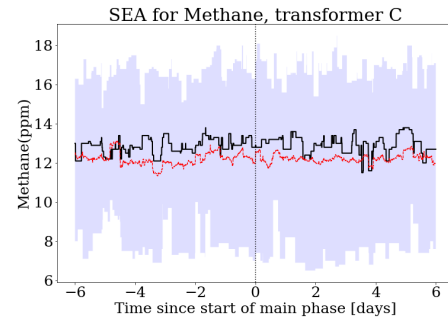
Figure 28: Superposed epoch analysis of all the storms in the 2010–2015 time period as defined by the storm list outlined in Walach *et al.* (2019). The black line shows the median, red dotted line shows the mean and the light blue shaded area shows the interquartile range.

highly variable nature of the gas data. In the median and mean, this noise cancels out to produce a largely constant gas concentration level. These particular results are applicable to transformer C, but are generally reproduced in other transformers studied.

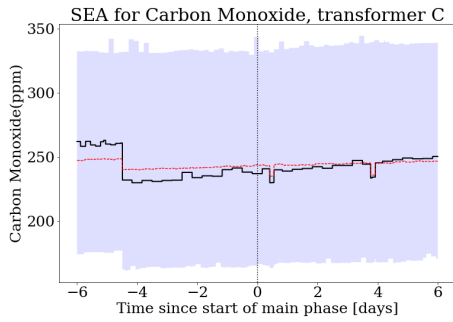
Figure 30 shows a superposed epoch analysis of the R index value (defined in equation 5) from the LEDT triangle. The data are aligned on the same epoch as in Figure 29 (i.e. the start of the main phase as defined in the storm list) and for the same transformer (C). The mean and median R values are again approximately constant, with the interquartile range large compared to the fluctuation in the mean and median. A small increase in the mean at the onset of the storm is much lower than the interquartile range, therefore not significant. The boundary of the normal region for healthy operation of the transformer is within the interquartile range, but below both the median and the mean R values throughout the 12 days shown. This suggests that transformer C is operating just outside the normal range during the majority of the 33 storms superposed. However, the R index plot agrees with the individual gas figures in Figure 29 that when the overall (and large) level of data noise is averaged out, the gas levels are very stable and appear to be unaffected by the presence of the storms. This echoes the results of the LEDT case studies, showing that the location of the gas data within the ternary



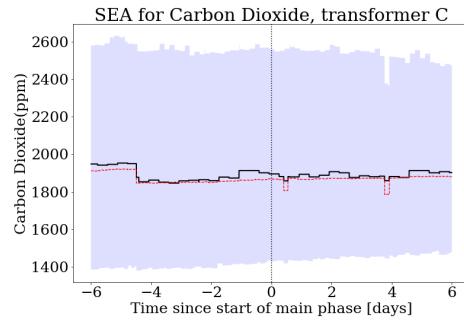
(a) SEA for Hydrogen concentration levels in transformer C.



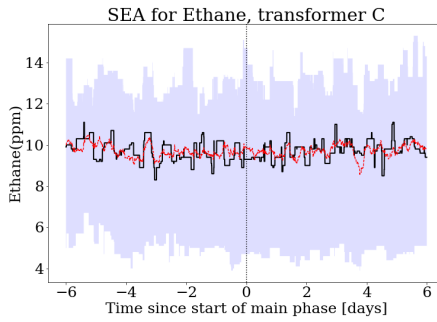
(b) SEA for Methane concentration levels in transformer C.



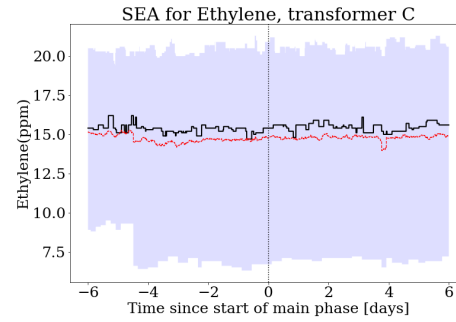
(c) SEA for Carbon Monoxide concentration levels in transformer C.



(d) SEA for Carbon Dioxide concentration levels in transformer C.



(e) SEA for Ethane concentration levels in transformer C.



(f) SEA for Ethylene concentration levels in transformer C.

Figure 29: Superposed Epoch Analyses for six gas concentrations. Gas data for 33 storms is superposed on the start of the main phase. The black line shows the median, the red dashed line shows the mean, and the blue shaded region shows the interquartile range.

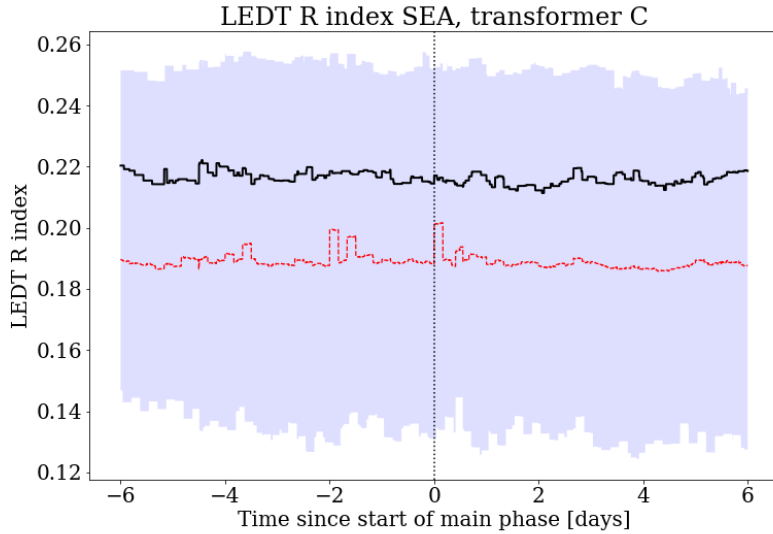


Figure 30: Superposed Epoch Analysis of the LEDT R index for transformer C, centred around the start of the main phase. The black line shows the median, the red dashed line shows the mean, and the blue shaded area shows the interquartile range.

plot remains stable after storm onset.

## 5 Further analysis

### 5.1 Heat maps

The rate of gas production in ppm/hour was then calculated for the key gases in each transformer. Figure 31 shows this rate of gas production (for all transformers) plotted against SYM-H for the 6 key gases. The colour gradient shows the number of data points in each pixel. It is clear that the majority of points lie in the region where  $\text{SYM-H} \approx 0$  and the gas production rate is very low. Only a small number of points lie at higher rates of gas production, and the symmetry of these points about the zero line indicate statistical noise in the gas data i.e. the same point mirrored above and below the zero line indicates one anomalous higher or lower concentration reading which then returns to the normal baseline. The vertical line of points around  $\text{SYM-H} = 0$  nT also suggests that the pattern is of a

statistical nature. Due to the much higher likelihood of SYM-H being close to zero (corresponding to non storm time), it is expected that any randomly fluctuating noise in the gas production rate would be more prevalent at this time. There is no indication from this plot that higher gas production rates are linked to more negative values of SYM-H (and therefore to geomagnetic storm conditions).

A similar analysis was then performed to compare the gas production rate and the rate of change of the horizontal component of the magnetic field ( $\frac{dB}{dt}$ ) as measured at Eskdalemuir. Figure 32 plots the gas production rate against the maximum  $\left|\frac{dB}{dt}\right|$  between the two consecutive gas readings (approximately 8 hours apart but not consistently spaced). Figure 33 shows the gas production rate now plotted against the mean  $\left|\frac{dB}{dt}\right|$  between each set of gas readings. Both plots show a similar picture to Figure 31; most of the data points lie where  $\left|\frac{dB}{dt}\right|$  and the gas production rate is low, and the remaining points are spread either side of the horizontal zero line showing a statistical spread due to noisy data. There is again no indication that increasing gas production rates occur at higher levels of geomagnetic activity.

## 5.2 Cross correlation

The exact timescale on which GICs affect transformer health is not clear. Blackouts have been known to occur during geomagnetic storms (for example, power outages in Sweden during the Halloween storm of 2003 (Pulkkinen *et al.*, 2005)), but in Thomson *et al.* (2010) (Figure 8) dissolved gas analysis shows an increase in gas production rates in two South African transformers from shortly after the storm up to 3 months later.

So far, this work has focussed on the gas levels during and up to a week after the storm main phase, but this section now considers the potential for a lag between high magnetic field change and increased gas production.

Figure 34 shows the results of a cross correlation method applied to the data. The two datasets that were cross-correlated were  $\left|\frac{dB}{dt}\right|$  calculated from the Eskdalemuir data and resampled up to 8 hours to match the gas data sampling rate. This is then compared with the gas production rate for hydrogen, methane and carbon monoxide in transformer B. Transformer B was selected for this analysis as it was

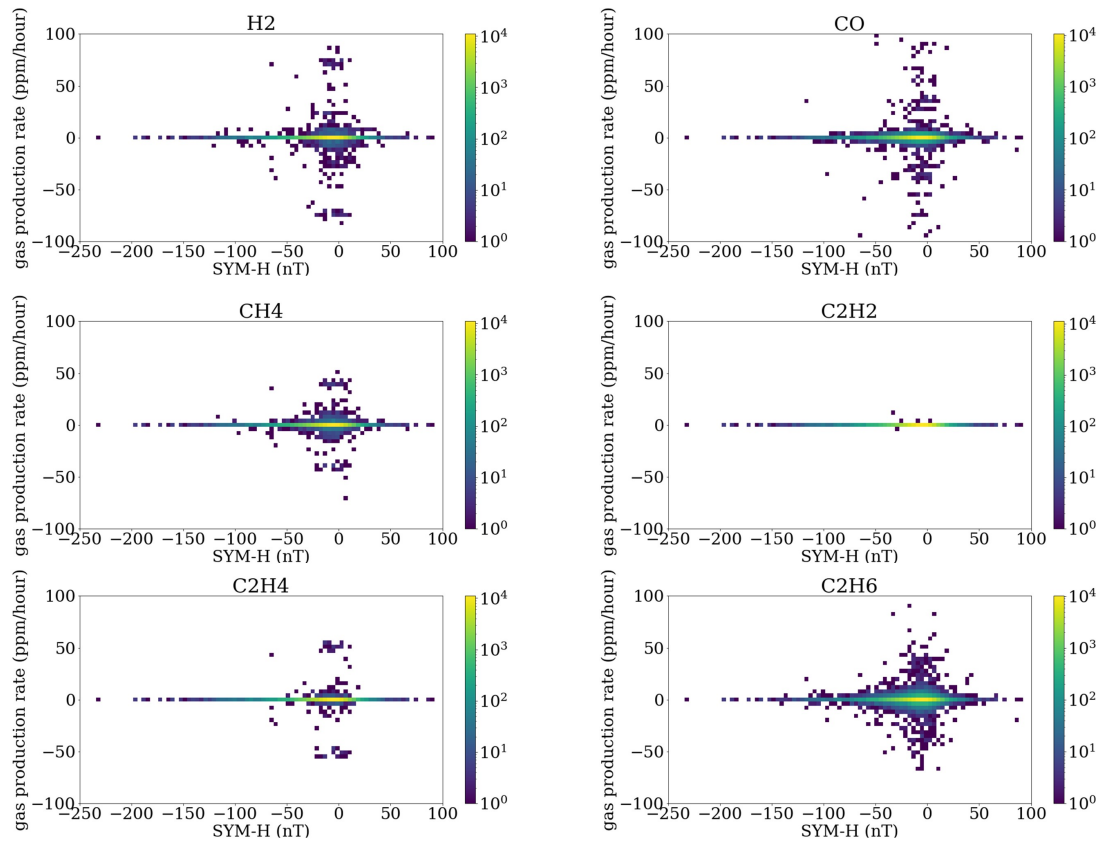


Figure 31: Heat maps showing the rate of gas of six key gases (in ppm/hour) against SYM-H. The colour scale corresponds to the number of data points in each pixel.

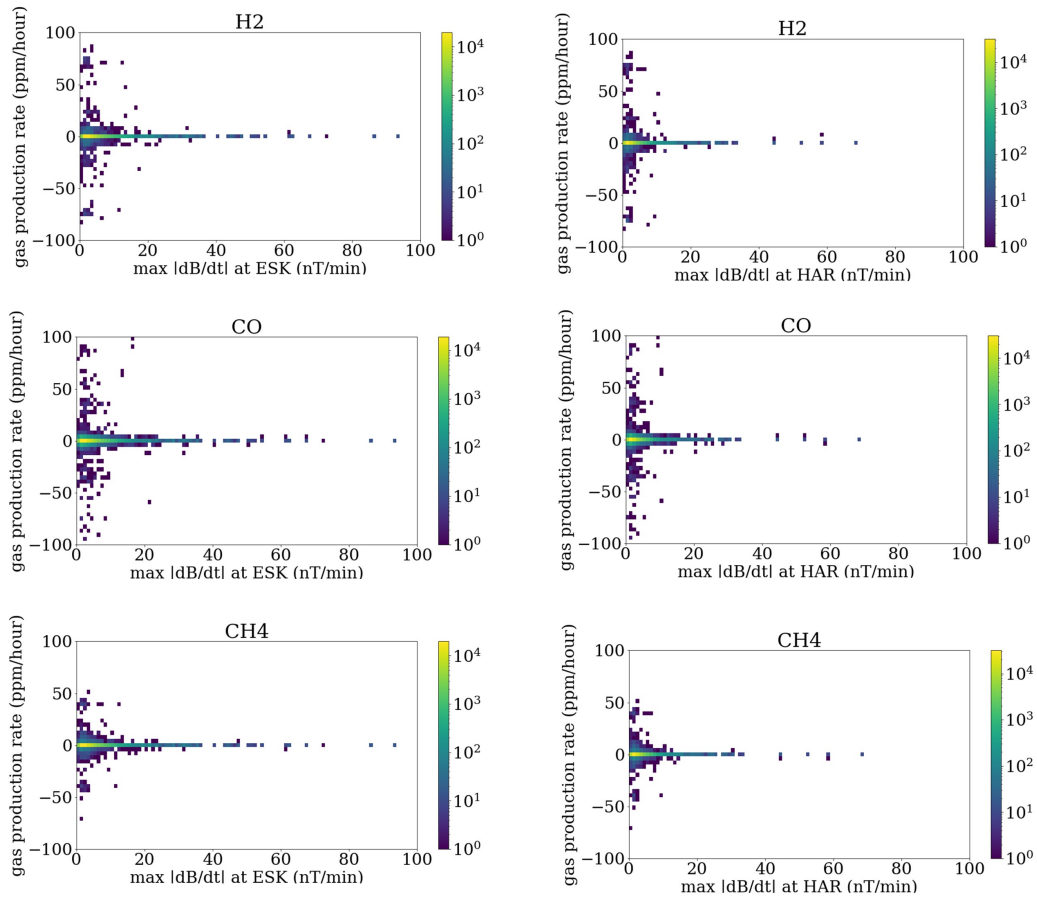


Figure 32: Heat maps showing the rate of gas production (in ppm/hour) against the maximum  $\left|\frac{dB}{dt}\right|$  recorded between consecutive gas readings. The top row shows hydrogen, the middle row shows carbon monoxide and the bottom row shows methane. The left column uses magnetometer readings from Eskdalemuir, and the right column shows magnetometer readings from Hartland.

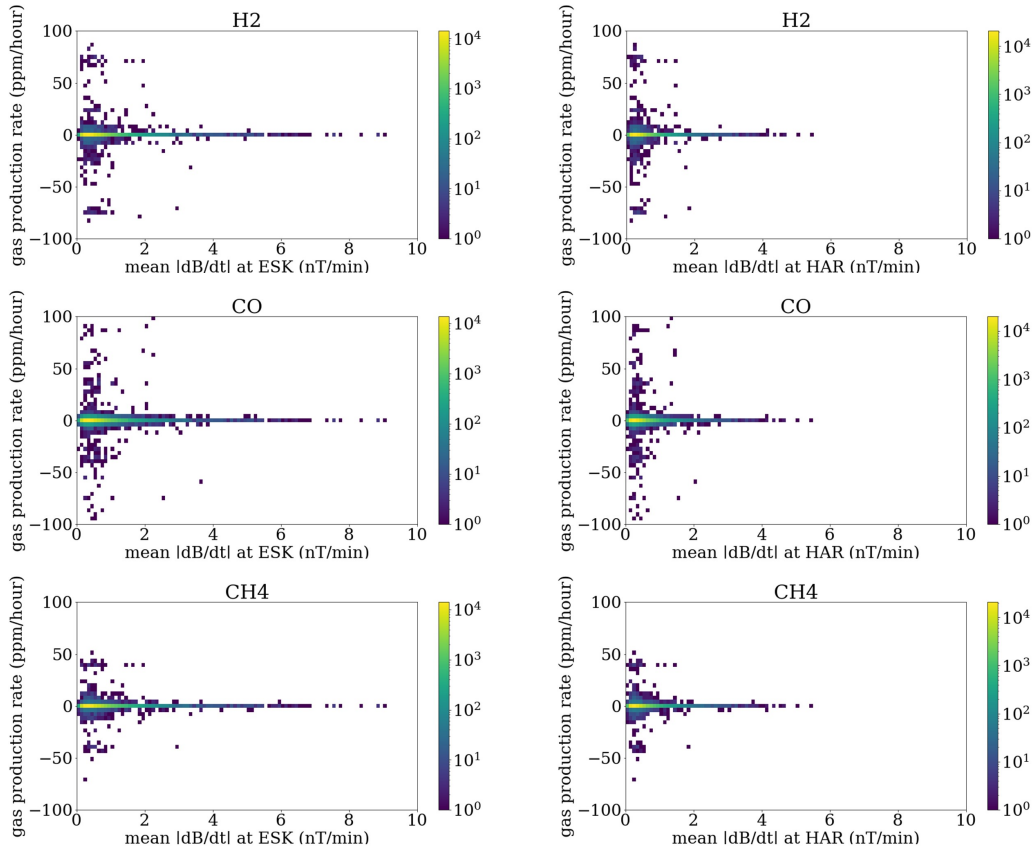


Figure 33: Heat maps showing the rate of gas production (in ppm/hour) against the mean  $\left|\frac{dB}{dt}\right|$  recorded between consecutive gas readings. The top row shows hydrogen, the middle row shows carbon monoxide and the bottom row shows methane. The left column uses magnetometer readings from Eskdalemuir, and the right column shows magnetometer readings from Hartland.

the only transformer where data was taken consistently every 3 hours, and the cross correlation function is not appropriate for inconsistently spaced data.

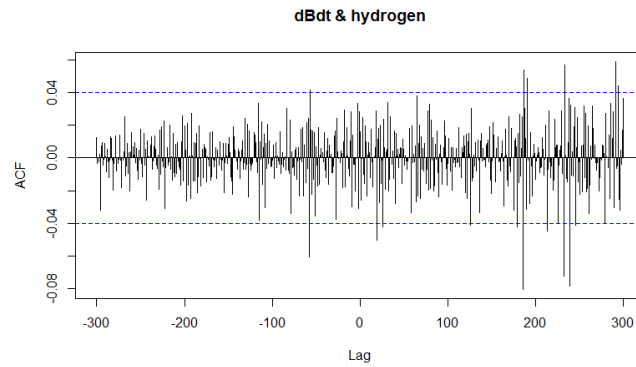
The lag along the x axis shows the number of readings the two datasets have been offset by. Strong correlation for a positive value of lag would indicate y leading x and strong correlation at the negative values of lag would indicate y lagging behind x. In this case, y is the gas concentration rate of change in ppm/hour and x is the magnitude of the change in the geomagnetic field (in nT/min). We would therefore expect to see a strong positive correlation for negative values of lag if large values of  $\left|\frac{dB}{dt}\right|$  were followed by an increase in the gas production rate some time later. This analysis has been performed for a lag of up to 300 readings, or 100 days, to be in line with the results from Thomson *et al.* (2010) which had a gas production increase over 3 months.

It can be seen in Figure 34 that the strength of the correlation at all lags is very weak and below the 95% confidence intervals for the majority of lag values. The few correlation values which lie outside the confidence intervals are not large or enough to be significant and can be attributed to statistical noise (we would expect the 95% confidence level to be surpassed 5% of the time).

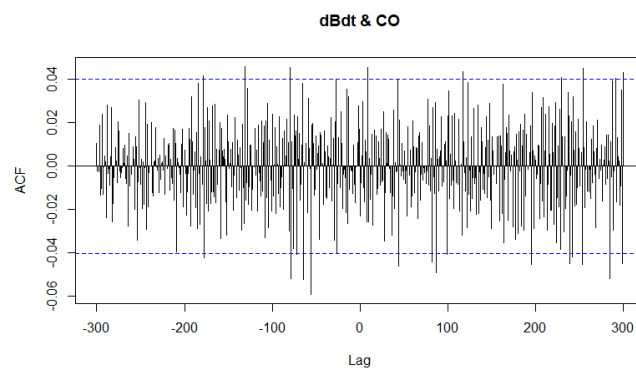
These results are reassuring in that they confirm that the results of the previous analyses discussed in this work are unlikely to change if a longer time lags were to be considered. However, this cross correlation has only been applied to one transformer due to constraints in the sampling rates of the gas data.

## 6 Discussion and suggestions for future work

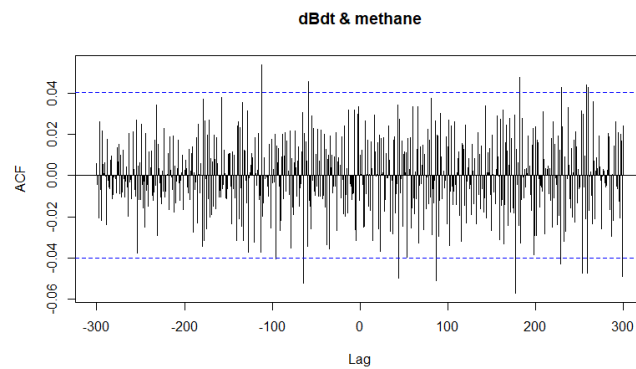
In this study, DGA measurements were exploited to look for trends in transformer health related to geomagnetic storm activity. Case studies were considered for the 10 largest geomagnetic storms in the 2010–2015 period, and the Low Energy Degradation Triangle method was used to look for low-level changes to transformer health. The LEDTs showed that in most cases, the transformers appear to be operating away from the normal region, despite no faults being reported by the energy company during this time. This raises several questions about the suitability of the LEDT to pre-empt transformer faults in this situation, and further research may need to be undertaken on the validity of the method in predicting



(a) Hydrogen



(b) Carbon monoxide



(c) Methane

Figure 34: Cross correlation function plots for the production rate of 3 gases in transformer B with the magnitude of the rate of change of the horizontal magnetic field (Eskdalemuir). The x axis label refers to the number of gas readings the two data sets have been offset by and therefore is in multiples of 8 hours, with Lag = 300 corresponding to a 100 day lag. The horizontal blue lines indicate the 95% confidence interval.

faults in general. However, it is noted in Moodley *et al.* (2017) that an abnormal LEDT result does not indicate absolute likelihood of a transformer failure, and DGA methods in general are empirical and should be applied with caution.

In further work, this analysis could be expanded to periods of greater solar activity, as 2010–2015 lies in a relatively quiet solar cycle, with no geomagnetic storms that would be considered large on the scale of the past few decades. It is well understood that transformers can be impacted by space weather, and recorded examples of blackouts are described in section 1.4.1. It would also be beneficial to incorporate direct GIC measurements from transformer sites, or to use a geoelectric field model to find more accurate estimates of the GIC values at each location.

In this study,  $\frac{dB}{dt}$  and SYM-H were used as a proxy for actual GIC values, as they were not routinely measured during the time period considered. Therefore, an assumption has been made that the largest GICs flowing through transformer neutrals will also occur during the largest measured geomagnetic storms, and in reality this may not be the case. The magnitude of GICs in transformers is dependent on many factors, such as geology, latitude, proximity to the coast and geometry of the local electricity network with respect to the direction of the geoelectric field. For this reason, further study may focus on more local factors affecting a particular site to determine whether GICs have affected transformer health at that location.

Another way in which this analysis could be extended is by including more contextual data from the transformer sites about when maintenance work was performed; for example whether the transformer oil was cleaned or the transformer was removed from service. This data would clarify gaps in the gas measurements and probably explain some of the more abnormal results in the LEDT analysis. This data was not available during the course of this project, and would be a valuable component of future work in this area.

## 7 Summary and conclusions

Space weather is a known risk to transformers as storm events produce geomagnetically induced currents which follow the path of least resistance through grounded electricity infrastructure. This results in quasi-DC currents flowing through transformer neutrals and resulting in half-wave saturation and localised heating within

the insulation and windings.

Localised heating within transformers releases small quantities of gases into the insulating oil, which can be remotely measured without the need to remove the transformer from service. These dissolved gas measurements can then be used to monitor equipment health and to predict and diagnose faults. As GICs are not routinely directly measured at power station sites, dissolved gas analysis can be employed to look for unusual heating as a result of space weather activity.

In this study, dissolved gas data from UK power station transformers were analysed in detail in a space weather context for the first time. Beyond a superficial examination of a dissolved gas time series, several analysis techniques have been explored which could further be usefully applied to a variety of transformer contexts and locations.

The data utilised in this study were from 13 nuclear power station transformers across the UK, in which concentrations of 8 different gases were measured thrice daily and recorded between 2010 and 2015. This information was then analysed alongside space weather data, namely SYM-H and the rate of change of the horizontal component of the ground magnetic field. Events were identified from these data sets by using a threshold in SYM-H, and by taking half-hourly averages of  $\frac{dB}{dt}$  to look at particularly active times.

The Low Energy Degradation Triangle (LEDT) method was then used alongside other common dissolved gas analysis methods to produce case studies for some of the largest storm events found for this time period, and three of these case studies have been discussed. No decisive evidence of transformer deterioration linked to space weather was found, though it is worth noting that the storms studied were uncharacteristically infrequent and small in magnitude compared to others in recorded history.

Further statistical techniques were then implemented to look for systematic changes in gas production rate during storm events. Firstly, a superposed epoch analysis was performed for each gas and transformer, superposing the time series of gas data for each storm identified. Again, no increase in the gas production rate could be observed, and in general the noise in the data cancelled out to leave fairly consistent mean and median values, with a large interquartile range. Heat maps and a cross-correlation function were also used, finding no evidence of a correlation

between high  $\frac{dB}{dt}$  or SYM-H values and higher rates of gas production.

The results of this study provide evidence that lower level geomagnetic activity is unlikely to cause significant damage to modern transformers in the UK. While these results are reassuring, it is important not to be complacent. We know that large space weather events can impact transformers, and the results of this study do not contradict this. Damage may only occur during more severe and rare geomagnetic storms. In future, the work outlined in this dissertation could be extended to more geomagnetically active years, and the results may be very different. As we move into solar cycle 25 over the next few years, the frequency of space weather events will increase, and GIC monitoring will become more prevalent at transformer sites. Through interdisciplinary collaboration and research, our increased ability to predict and mitigate space weather impacts will serve to make future infrastructure more resilient.

## References

- Allen, Sauer, Frank, and Reiff (1989). “Allen 1989 effects of the 1989 solar activity”. In: *Eos* 70.
- Bakar, N., A. Abu-Siada, and S. Islam (2014). “A review of dissolved gas analysis measurement and interpretation techniques”. In: *IEEE Electrical Insulation Magazine* 30.3, pp. 39–49. ISSN: 08837554. DOI: 10.1109/MEI.2014.6804740.
- Baumjohann, W. and R. A. Treumann (2012). *Basic space plasma physics: Revised Edition*. Imperial College Press, pp. 1–479. ISBN: 9781848168961. DOI: 10.1142/P850.
- Beggan, C. D., D. Beamish, A. Richards, G. S. Kelly, and A. W. Alan (2013). “Prediction of extreme geomagnetically induced currents in the UK high-voltage network”. In: *Space Weather* 11.7, pp. 407–419. ISSN: 15427390. DOI: 10.1002/swe.20065.
- Borovsky, J. E. and Y. Y. Shprits (2017). *Is the Dst Index Sufficient to Define All Geospace Storms?* DOI: 10.1002/2017JA024679.
- Boteler, D. (2014). “Methodology for simulation of geomagnetically induced currents in power systems”. In: *Journal of Space Weather and Space Climate* 4. ISSN: 21157251. DOI: 10.1051/swsc/2014018.
- Cabinet Office (2020). “National Risk Register; 2020 edition”. In: p. 5. URL: [https://assets.publishing.service.gov.uk/government/uploads/system/uploads/attachment\\_data/file/952959/6.6920\\_CO\\_CCS\\_s\\_National\\_Risk\\_Register\\_2020\\_11-1-21-FINAL.pdf](https://assets.publishing.service.gov.uk/government/uploads/system/uploads/attachment_data/file/952959/6.6920_CO_CCS_s_National_Risk_Register_2020_11-1-21-FINAL.pdf).
- Cannon, P. (2013). *Extreme space weather: impacts on engineered systems and infrastructures*. Royal Academy of Engineering, p. 70. ISBN: 1-903496-95-0.
- Carrington, R. C. (1859). *Description of a Singular Appearance seen in the Sun on September 1, 1859*. Tech. rep. URL: <https://academic.oup.com/mnras/article/20/1/13/983482>.
- Chakraborty, S. and S. K. Morley (2020). “Probabilistic prediction of geomagnetic storms and the Kp index”. In: *Journal of Space Weather and Space Climate* 10. ISSN: 21157251. DOI: 10.1051/swsc/2020037.

- Department for Environment, Food and Rural Affairs (2013). “Estimating energy saving potential from transformers and evaluating their impact on the feasibility of renewable energy systems”. In: March, pp. 1–46.
- Dimmock, A. P., L. Rosenqvist, D. T. Welling, A. Viljanen, I. Honkonen, R. J. Boynton, and E. Yordanova (2020). “On the Regional Variability of dB/dt and Its Significance to GIC”. In: *Space Weather* 18.8. ISSN: 15427390. DOI: 10.1029/2020SW002497.
- Duval, M. (2002). “A review of faults detectable by gas-in-oil analysis in transformers”. In: *IEEE Electrical Insulation Magazine* 18.3, pp. 8–17. DOI: 10.1109/MEI.2002.1014963.
- Eastwood, J. P. (2008). “The science of space weather”. In: *Philosophical Transactions of the Royal Society A: Mathematical, Physical and Engineering Sciences* 366.1884, pp. 4489–4500. ISSN: 1364503X. DOI: 10.1098/rsta.2008.0161.
- Gaunt, C. T. (2014). “Reducing uncertainty - Responses for electricity utilities to severe solar storms”. In: *Journal of Space Weather and Space Climate* 4. ISSN: 21157251. DOI: 10.1051/swsc/2013058.
- Girgis, R., K. Vedante, and K. Gramm (2012). “Effects of geomagnetically induced currents on power transformers and power systems”. In: *44th International Conference on Large High Voltage Electric Systems 2012*, pp. 1–8.
- Gjerloev, J. W. (2012). “The SuperMAG data processing technique”. In: 117. DOI: 10.1029/2012JA017683.
- Hapgood, M., M. J. Angling, G. Attrill, M. Bisi, P. S. Cannon, C. Dyer, J. P. Eastwood, S. Elvidge, M. Gibbs, R. A. Harrison, C. Hord, R. B. Horne, D. R. Jackson, B. Jones, S. Machin, C. N. Mitchell, J. Preston, J. Rees, N. C. Rogers, G. Routledge, K. Ryden, R. Tanner, A. W. P. Thomson, J. A. Wild, and M. Willis (2021). “Development of Space Weather Reasonable Worst-Case Scenarios for the UK National Risk Assessment”. In: *Space Weather* 19.4, pp. 1–32. ISSN: 1542-7390. DOI: 10.1029/2020sw002593.
- Hutchinson, J. A., D. M. Wright, and S. E. Milan (2011). “Geomagnetic storms over the last solar cycle: A superposed epoch analysis”. In: *Journal of Geophysical Research: Space Physics* 116.9. ISSN: 21699402. DOI: 10.1029/2011JA016463.
- Kelly, G. S., A. Viljanen, C. D. Beggan, and A. W.P. Thomson (2017). “Understanding GIC in the UK and French high-voltage transmission systems during

- severe magnetic storms”. In: *Space Weather* 15.1, pp. 99–114. ISSN: 15427390. DOI: 10.1002/2016SW001469.
- Moldwin, M (2008). *An introduction to space weather*. Cambridge University Press, pp. 1–142. ISBN: 9780511801365. DOI: 10.1017/CB09780511801365.
- Molinski, T. S (2002). *Why utilities respect geomagnetically induced currents*. Tech. rep., pp. 1765–1778.
- Moodley, N. and C. T. Gaunt (2017). “Low Energy Degradation Triangle for power transformer health assessment”. In: *IEEE Transactions on Dielectrics and Electrical Insulation* 24.1, pp. 639–646. ISSN: 10709878. DOI: 10.1109/TDEI.2016.006042.
- Morley, S., D. Welling, J. Koller, B. Larsen, M. Henderson, and J. Niehof (2010). “SpacePy - A Python-based Library of Tools for the Space Sciences”. In: *Proceedings of the 9th Python in Science Conference Scipy*, pp. 67–72. DOI: 10.25080/majora-92bf1922-00c.
- Mukhtar, K., M. Ingham, C. J. Rodger, D. H. Mac Manus, T. Divett, W. Heise, E. Bertrand, M. Dalzell, and T. Petersen (2020). “Calculation of GIC in the North Island of New Zealand Using MT Data and Thin-Sheet Modeling”. In: *Space Weather* 18.11. ISSN: 15427390. DOI: 10.1029/2020SW002580.
- Oughton, E. J., M. Hapgood, G. S. Richardson, C. D. Beggan, A. W. P. Thomson, M. Gibbs, C. Burnett, C. T. Gaunt, M. Trichas, R. Dada, and R. B. Horne (2019). “A Risk Assessment Framework for the Socioeconomic Impacts of Electricity Transmission Infrastructure Failure Due to Space Weather: An Application to the United Kingdom”. In: *Risk Analysis* 39.5, pp. 1022–1043. ISSN: 15396924. DOI: 10.1111/risa.13229.
- Pulkkinen, A., E. Bernabeu, A. Thomson, A. Viljanen, R. Pirjola, D. Boteler, J. Eichner, P. J. Cilliers, D. Welling, N. P. Savani, R. S. Weigel, J. J. Love, C. Balch, C. M. Ngwira, G. Crowley, A. Schultz, R. Kataoka, B. Anderson, D. Fugate, J. J. Simpson, and M. MacAlester (2017). “Geomagnetically induced currents: Science, engineering, and applications readiness”. In: *Space Weather* 15.7, pp. 828–856. DOI: 10.1002/2016SW001501.
- Pulkkinen, A., M. Kuznetsova, A. Ridley, J. Raeder, A. Vapirev, D. Weimer, R. S. Weigel, M. Wiltberger, G. Millward, L. Rastätter, M. Hesse, H. J. Singer, and A. Chulaki (2011). “Geospace Environment Modeling 2008-2009 Challenge:

- Ground magnetic field perturbations”. In: *Space Weather* 9.2, pp. 1–13. ISSN: 15427390. DOI: 10.1029/2010SW000600.
- Pulkkinen, A., S. Lindahl, A. Viljanen, and R. Pirjola (2005). “Geomagnetic storm of 29-31 October 2003: Geomagnetically induced currents and their relation to problems in the Swedish high-voltage power transmission system”. In: *Space Weather* 3.8. ISSN: 15427390. DOI: 10.1029/2004SW000123.
- Riley, P. and J. J. Love (2017). “Extreme geomagnetic storms: Probabilistic forecasts and their uncertainties”. In: *Space Weather* 15.1, pp. 53–64. ISSN: 15427390. DOI: 10.1002/2016SW001470.
- Rodger, C. J., D. H. MacManus, M. Dalzell, A. W. P. Thomson, E. Clarke, T. Petersen, M. A. Clilverd, and T. Divett (2017). “Long-Term Geomagnetically Induced Current Observations From New Zealand: Peak Current Estimates for Extreme Geomagnetic Storms”. In: *Space Weather* 15.11, pp. 1447–1460. ISSN: 15427390. DOI: 10.1002/2017SW001691.
- Rogers (2020). “A global climatological model of extreme geomagnetic field fluctuations”. In: *Journal of Space Weather and Space Climate* 10, pp. 1–19. ISSN: 21157251. DOI: 10.1051/swsc/2020008.
- Smith, A. W. (2020). “The Influence of Sudden Commencements on the Rate of Change of the Surface Horizontal Magnetic Field in the United Kingdom”. In: DOI: 10.1029/2019SW002281.
- Smith, A. W., C. Forsyth, I. J. Rae, C. J. Rodger, and M. P. Freeman (2021). “The Impact of Sudden Commencements on Ground Magnetic Field Variability: Immediate and Delayed Consequences”. In: *Space Weather*, pp. 1–25. ISSN: 1542-7390. DOI: 10.1029/2021sw002764.
- Stover, Christopher (accessed 22nd July 2021). *Ternary Diagram*. URL: <https://mathworld.wolfram.com/TernaryDiagram.html>.
- Sun, H. C., Y. C. Huang, and C. M. Huang (2012). “A review of dissolved gas analysis in power transformers”. In: *Energy Procedia*. Vol. 14, pp. 1220–1225. DOI: 10.1016/j.egypro.2011.12.1079.
- Švanda, M., D. Mourenas, K. Žertová, and T. Výbošťáková (2020). “Immediate and delayed responses of power lines and transformers in the Czech electric power grid to geomagnetic storms”. In: *Journal of Space Weather and Space Climate* 10. ISSN: 21157251. DOI: 10.1051/swsc/2020025.

- Thomson, A. W. P., C. T. Gaunt, P. Cilliers, J. A. Wild, B. Opperman, L. A. McKinnell, P. Kotze, C. M. Ngwira, and S. I. Lotz (2010). “Present day challenges in understanding the geomagnetic hazard to national power grids”. In: *Advances in Space Research* 45.9, pp. 1182–1190. ISSN: 02731177. DOI: 10.1016/j.asr.2009.11.023.
- Thomson, A. W. P., A. J. McKay, E. Clarke, and S. J. Reay (2005). “Surface electric fields and geomagnetically induced currents in the Scottish Power grid during the 30 October 2003 geomagnetic storm”. In: *Space Weather* 3.11. DOI: 10.1029/2005sw000156.
- Torta, J. M., L. Serrano, J. R. Regué, A. M. Sánchez, and E. Roldán (2012). “Geomagnetically induced currents in a power grid of northeastern Spain”. In: *Space Weather* 10.6. ISSN: 15427390. DOI: 10.1029/2012SW000793.
- Trivedi, N. B., Í. Vitorello, W. Kabata, S. L. G. Dutra, A. L. Padilha, S. B. Mauricio, M. B. De Pádua, A. P. Soares, G. S. Luz, F. De A. Pinto, R. Pirjola, and A. Viljanen (2007). “Geomagnetically induced currents in an electric power transmission system at low latitudes in Brazil: A case study”. In: *Space Weather* 5.4. ISSN: 15427390. DOI: 10.1029/2006SW000282.
- Walach, M. T. and A. Grocott (2019). “SuperDARN Observations During Geomagnetic Storms, Geomagnetically Active Times, and Enhanced Solar Wind Driving”. In: *Journal of Geophysical Research: Space Physics* 124.7, pp. 5828–5847. ISSN: 21699402. DOI: 10.1029/2019JA026816.
- Wanliss, J. A. and K. M. Showalter (2006). “High-resolution global storm index: Dst versus SYM-H”. In: *Journal of Geophysical Research: Space Physics* 111.2. ISSN: 21699402. DOI: 10.1029/2005JA011034.
- Weygand, J. M. (2021). “The temporal and spatial development of dB/dt for substorms”. In: *AIMS Geosciences* 7.1, pp. 74–94. ISSN: 2471-2132. DOI: 10.3934/geosci.2021004.

## A Event lists

	<b>SYM-H events</b>	<b>min SYM-H</b>
<b>1</b>	2015-03-17 22:47:00	-234
<b>2</b>	2015-06-23 04:24:00	-208
<b>3</b>	2015-12-20 22:49:00	-160
<b>4</b>	2011-10-25 01:15:00	-150
<b>5</b>	2012-03-09 08:13:00	-141
<b>6</b>	2012-10-01 03:52:00	-138
<b>7</b>	2013-06-01 07:48:00	-137
<b>8</b>	2015-01-07 11:00:00	-135
<b>9</b>	2013-03-17 20:28:00	-132
<b>10</b>	2014-02-19 08:23:00	-127

Table 2

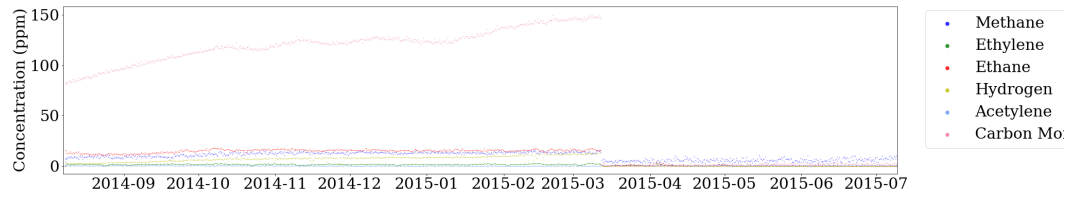
	<b>ESK events</b>	<b>ESK mean</b> $\left  \frac{dB}{dt} \right $
<b>1</b>	2015-03-17 23:00:00	29.241386
<b>2</b>	2012-03-15 17:00:00	18.739061
<b>3</b>	2015-06-23 04:00:00	17.957604
<b>4</b>	2012-06-16 22:30:00	14.023114
<b>5</b>	2014-06-08 07:30:00	12.178883
<b>6</b>	2015-12-20 16:30:00	11.897399
<b>7</b>	2012-07-15 19:30:00	11.524243
<b>8</b>	2011-08-05 19:00:00	11.385472
<b>9</b>	2013-03-17 18:30:00	10.308739
<b>10</b>	2015-10-07 18:30:00	10.155435

Table 3

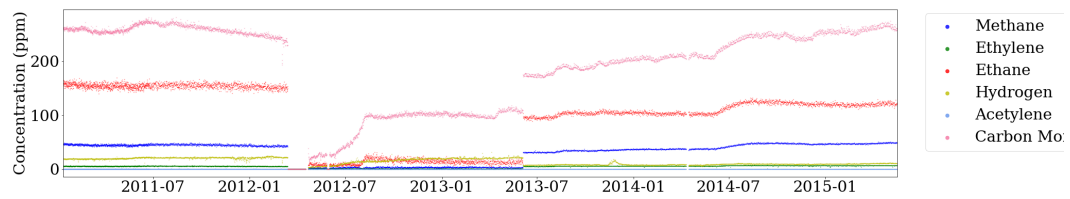
	<b>HAR events</b>	<b>HAR mean</b> $\left  \frac{dB}{dt} \right $
<b>1</b>	2012-06-16 22:30:00	11.766768
<b>2</b>	2015-06-22 18:30:00	11.388441
<b>3</b>	2015-03-17 17:30:00	10.504494
<b>4</b>	2014-06-08 07:30:00	8.519644
<b>5</b>	2012-03-15 17:00:00	7.960874
<b>6</b>	2012-07-14 18:00:00	7.845942
<b>7</b>	2011-08-05 19:00:00	7.773560
<b>8</b>	2010-08-04 10:30:00	7.009526
<b>9</b>	2012-03-08 13:00:00	5.794510
<b>10</b>	2011-09-26 19:30:00	5.557838

Table 4

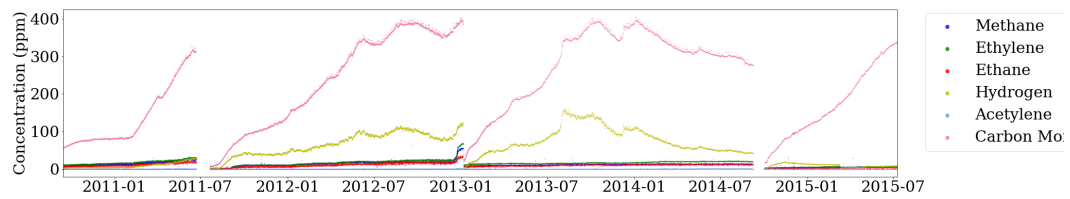
## B Raw gas concentrations



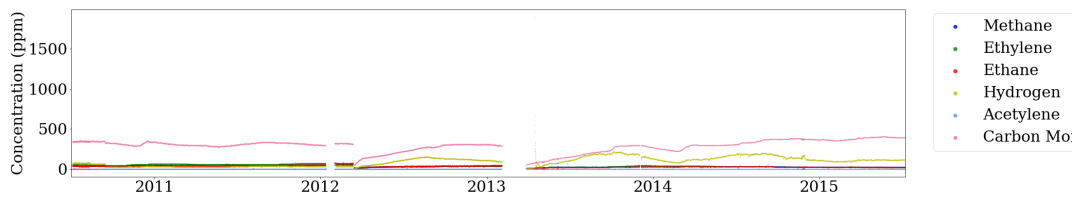
(a) Transformer A



(b) Transformer B

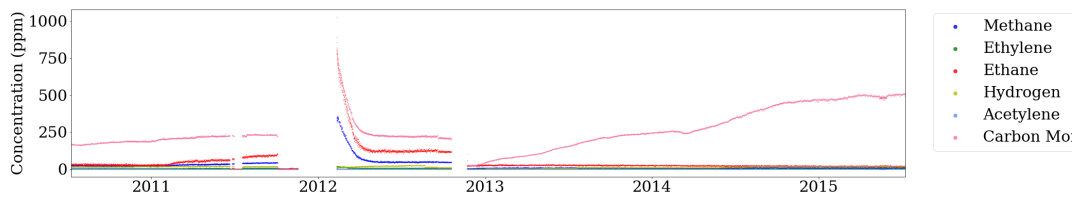


(c) Transformer C

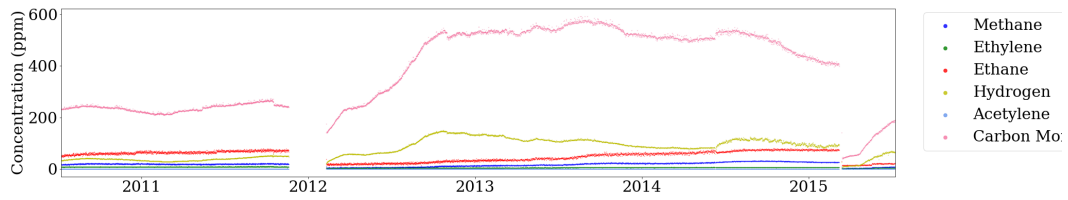


(d) Transformer D

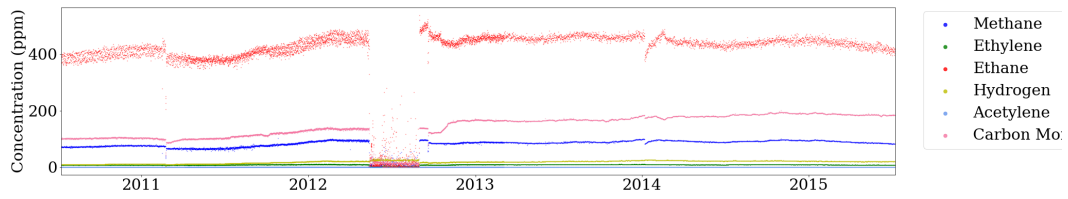
Figure 35: Caption



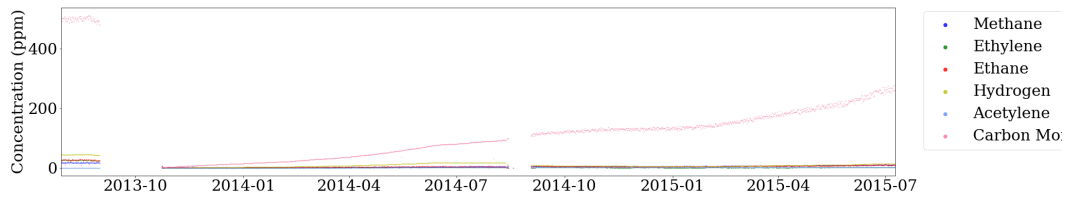
(a) Transformer F



(b) Transformer G

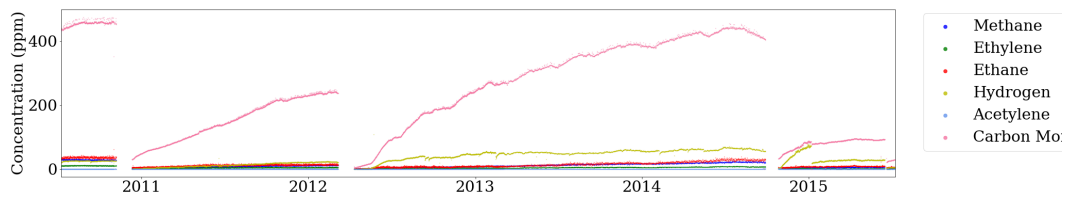


(c) Transformer H

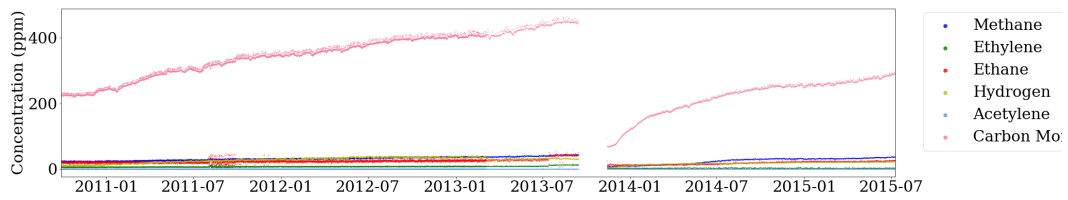


(d) Transformer I

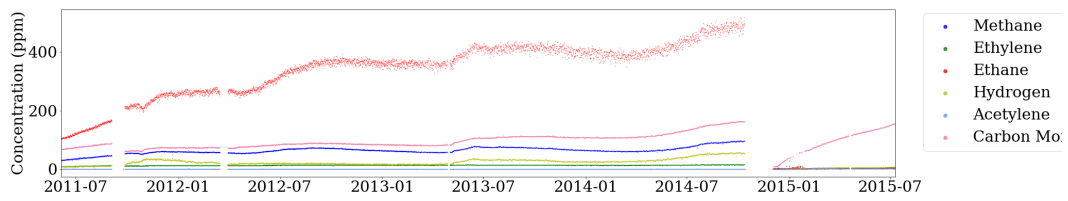
Figure 36: Caption



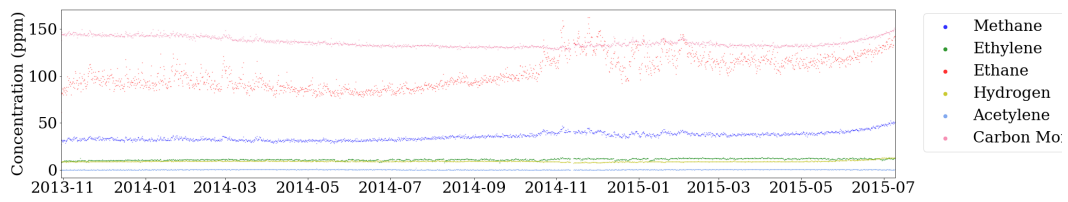
(a) Transformer J



(b) Transformer K



(c) Transformer L



(d) Transformer M

Figure 37: Caption

## C LEDTs

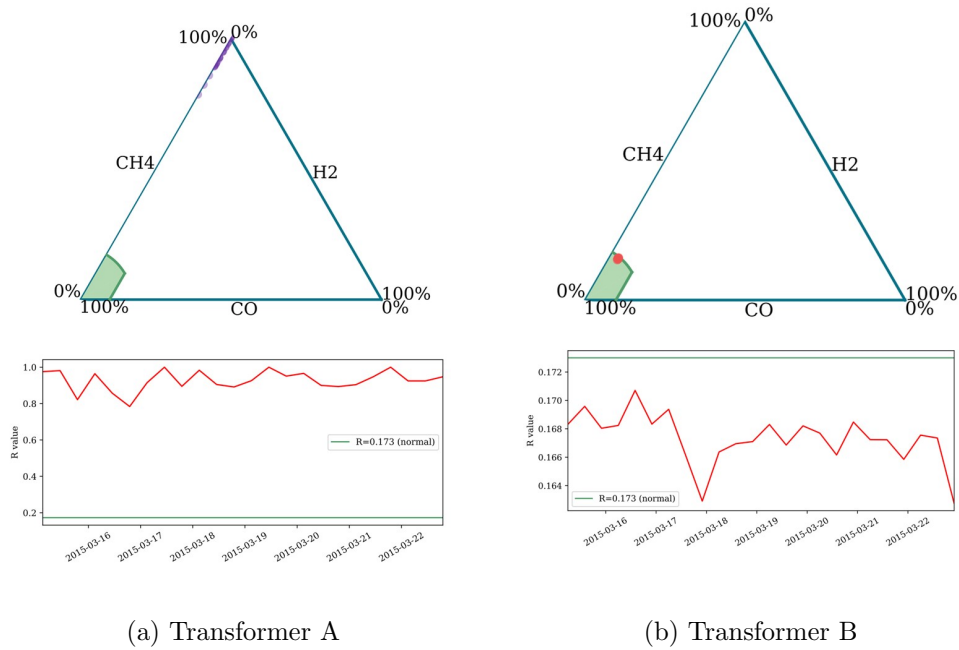
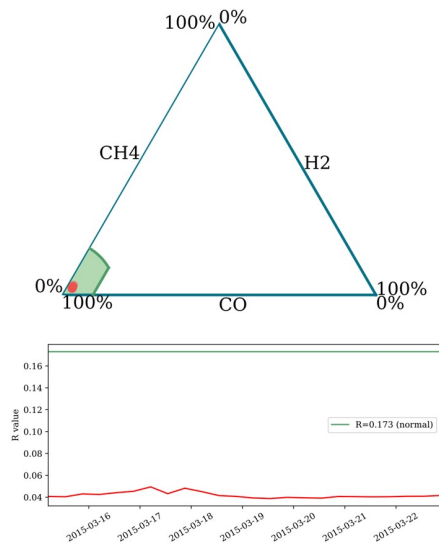
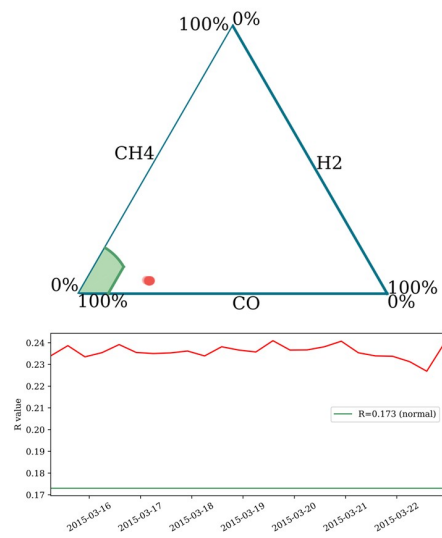


Figure 38: March 2015 storm (case study 1), transformers A-B. Low Energy Degradation Triangle in the upper panel of each figure shows the location of the data in a ternary plot for 15th–23rd March 2015. The lower panel in each figure shows the R index, with the boundary of the normal region marked in green.

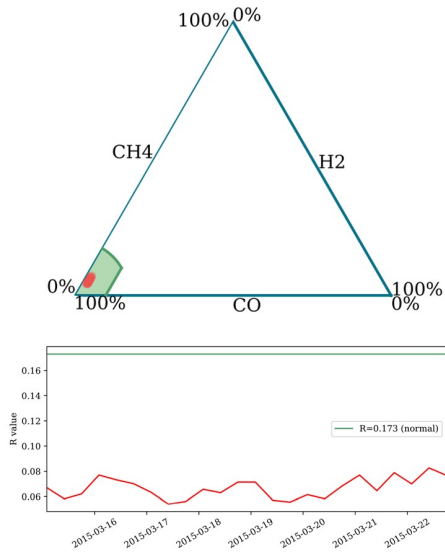


(a) Transformer C

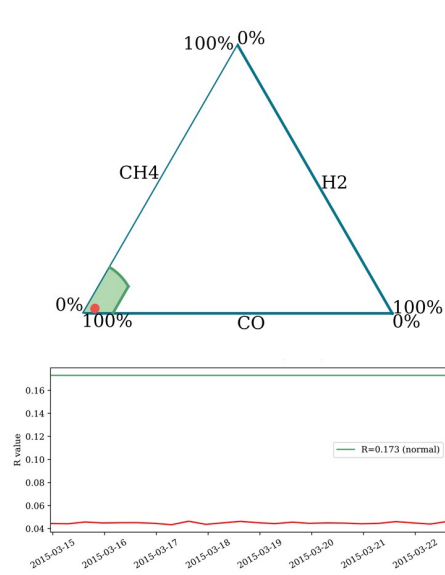


(b) Transformer D

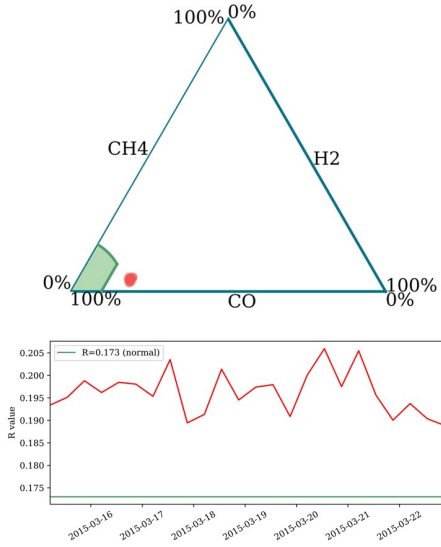
Figure 39: March 2015 storm (case study 1), transformers C-D. Low Energy Degradation Triangle in the upper panel of each figure shows the location of the data in a ternary plot for 15th–23rd March 2015. The lower panel in each figure shows the R index, with the boundary of the normal region marked in green.



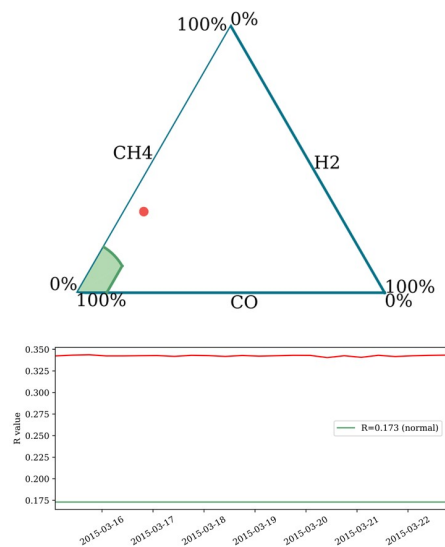
(a) Transformer E



(b) Transformer F

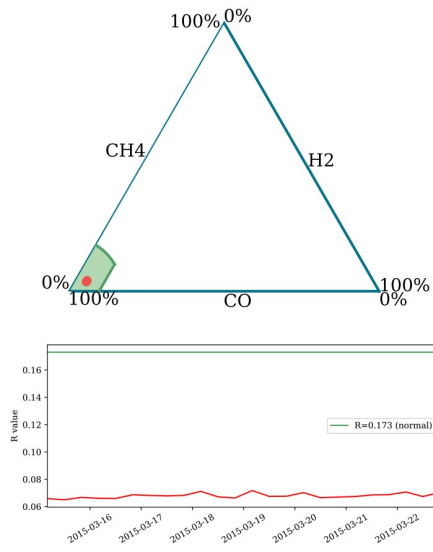


(c) Transformer G

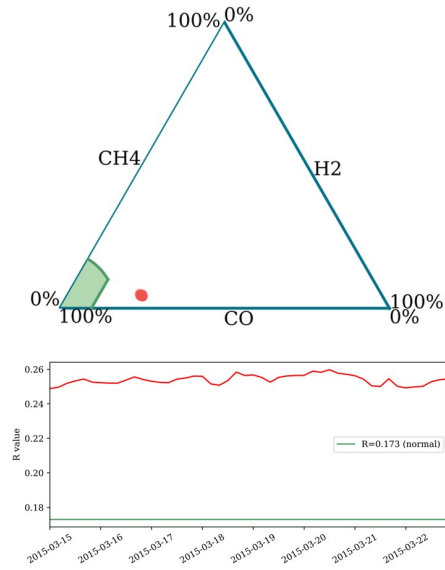


(d) Transformer H

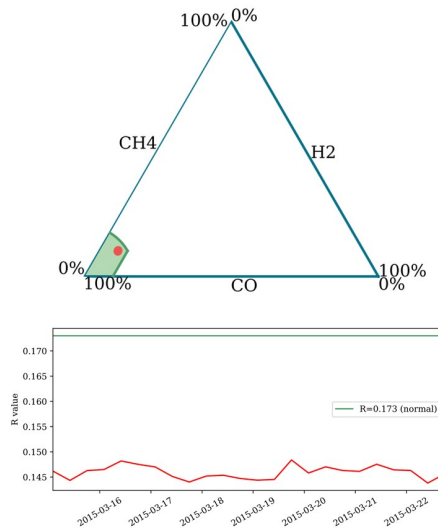
Figure 40: March 2015 storm (case study 1), transformers E-H. Low Energy Degradation Triangle in the upper panel of each figure shows the location of the data in a ternary plot for 15th–23rd March 2015. The lower panel in each figure shows the R index, with the boundary of the normal region marked in green.



(a) Transformer I

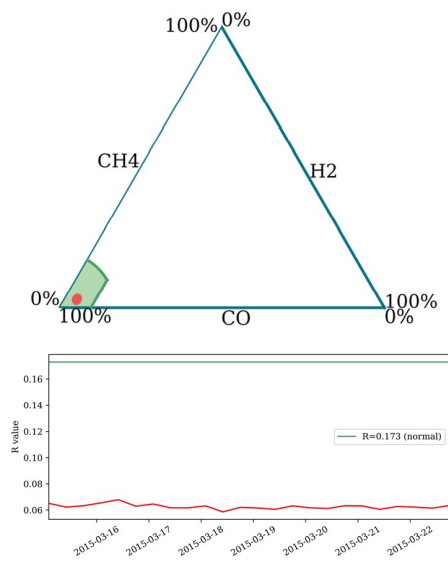


(b) Transformer J

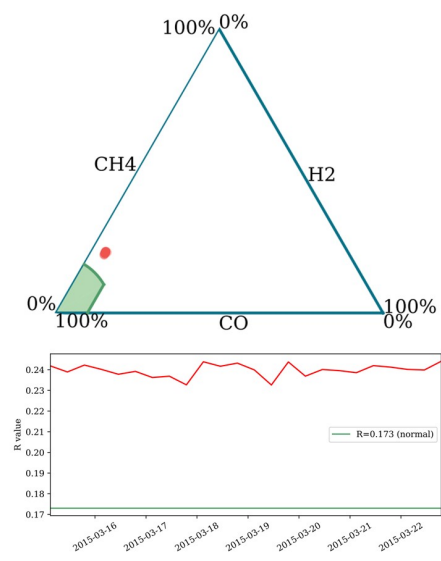


(c) Transformer K

Figure 41: March 2015 storm (case study 1), transformers I-K. Low Energy Degradation Triangle in the upper panel of each figure shows the location of the data in a ternary plot for 15th–23rd March 2015. The lower panel in each figure shows the R index, with the boundary of the normal region marked in green.

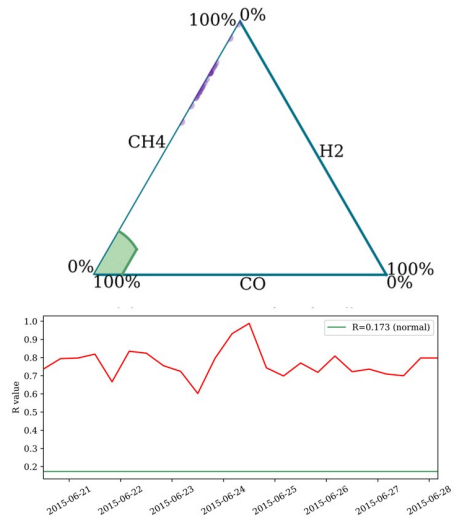


(a) Transformer L

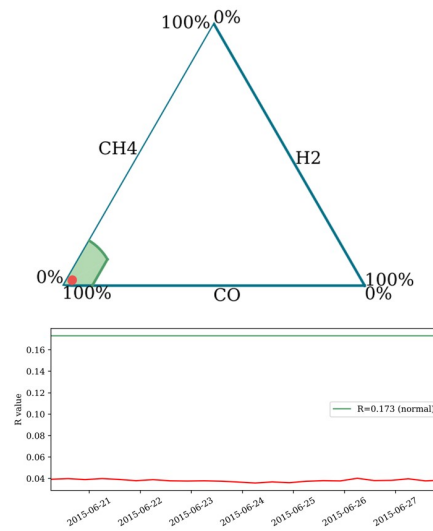


(b) Transformer M

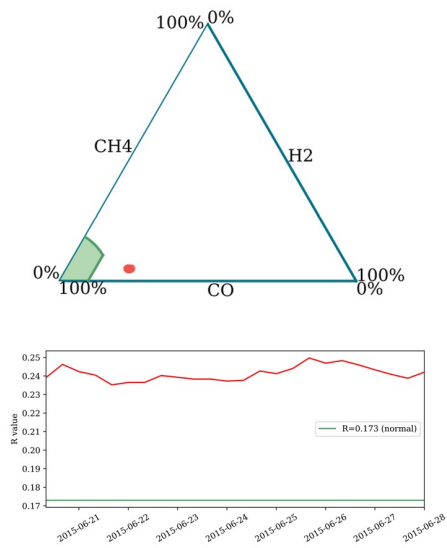
Figure 42: March 2015 storm (case study 1), transformers L-M. Low Energy Degradation Triangle in the upper panel of each figure shows the location of the data in a ternary plot for 15th–23rd March 2015. The lower panel in each figure shows the R index, with the boundary of the normal region marked in green.



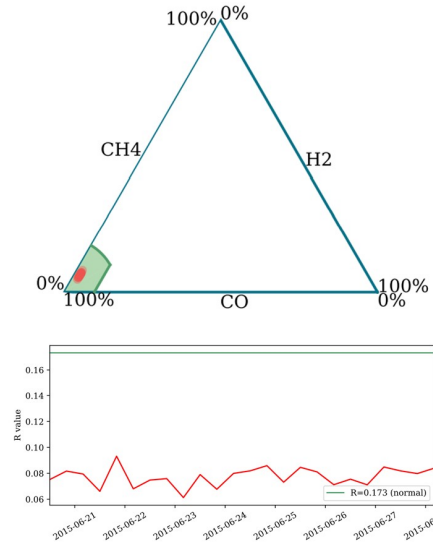
(a) Transformer A. Data points shown in purple indicate that one or more of the gas readings was 0 ppm.



(b) Transformer C

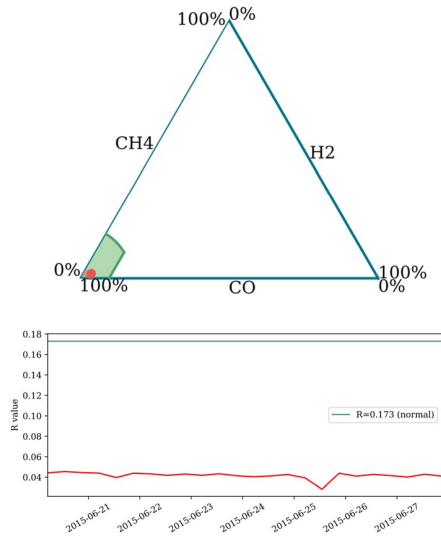


(c) Transformer D

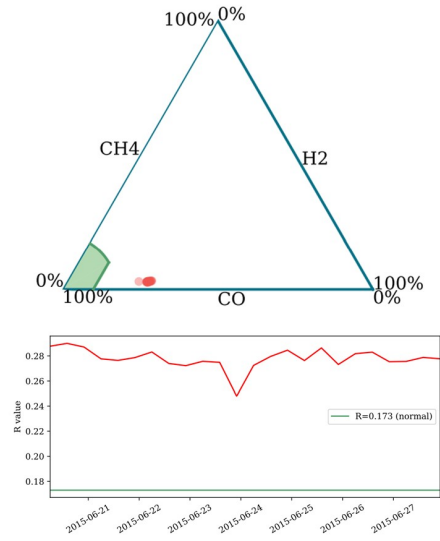


(d) Transformer E

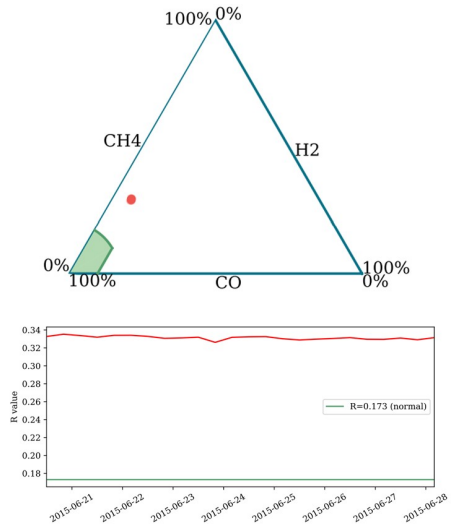
Figure 43: June 2015 storm (case study 2), transformers A-E. B not shown as DGA data was not available for this storm period. Low Energy Degradation Triangle in the upper panel of each figure shows the location of the data in a ternary plot for 20th–28th June 2015. The lower panel in each figure shows the R index, with the boundary of the normal region marked in green.



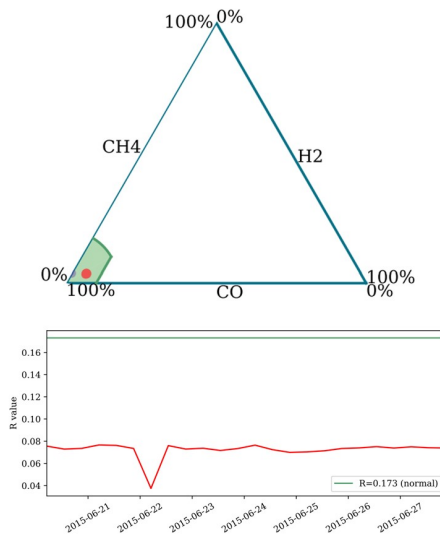
(a) Transformer F



(b) Transformer G

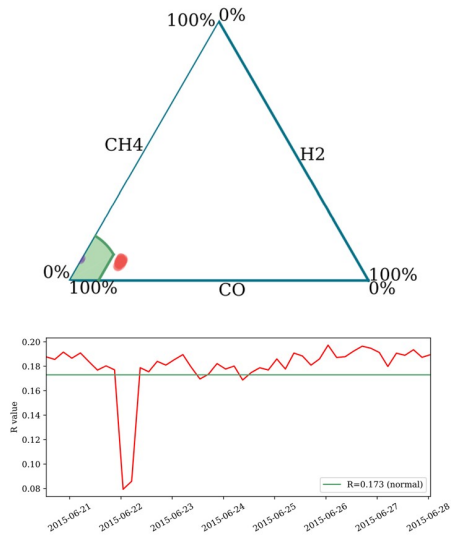


(c) Transformer H

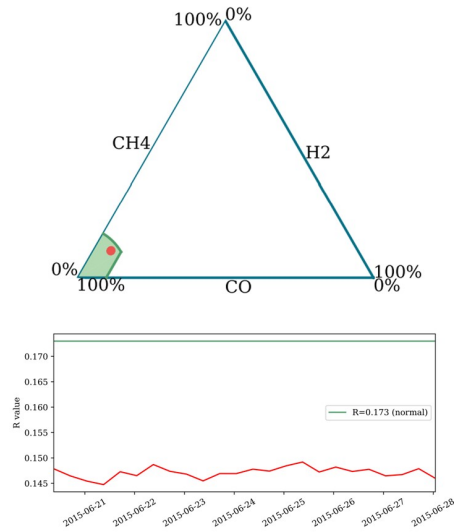


(d) Transformer I

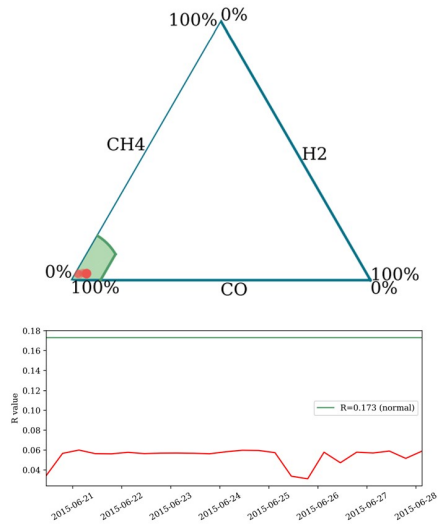
Figure 44: June 2015 storm (case study 2), transformers F-I. Low Energy Degradation Triangle in the upper panel of each figure shows the location of the data in a ternary plot for 20th–28th June 2015. The lower panel in each figure shows the R index, with the boundary of the normal region marked in green.



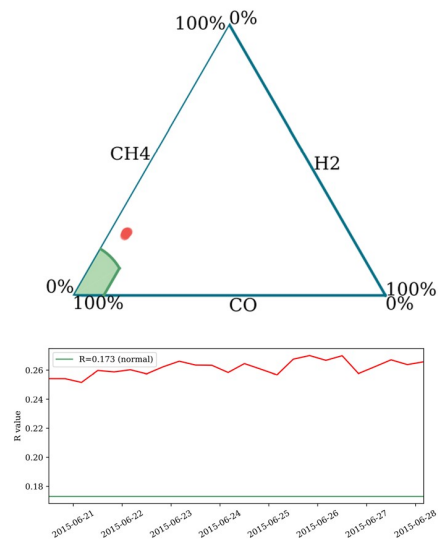
(a) Transformer J. Data points shown in purple indicate that one or more of the gas readings was 0 ppm.



(b) Transformer K

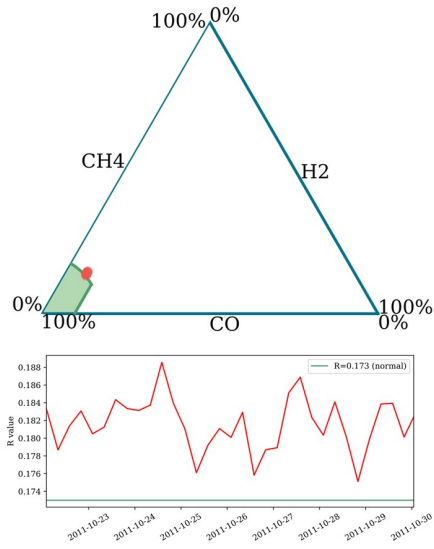


(c) Transformer L

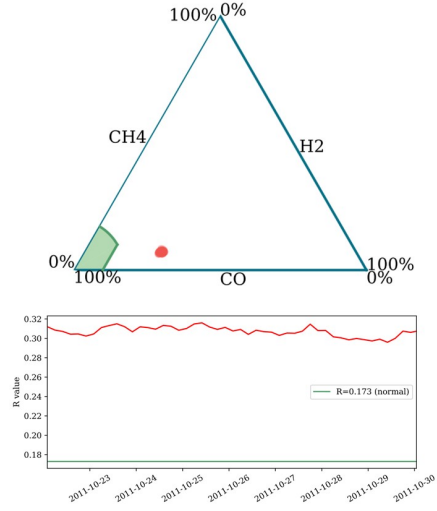


(d) Transformer M

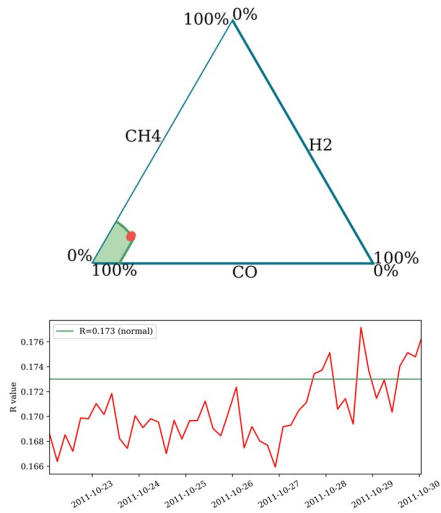
Figure 45: June 2015 storm (case study 2), transformers J-M. Low Energy Degradation Triangle in the upper panel of each figure shows the location of the data in a ternary plot for 20th–28th June 2015. The lower panel in each figure shows the R index, with the boundary of the normal region marked in green.



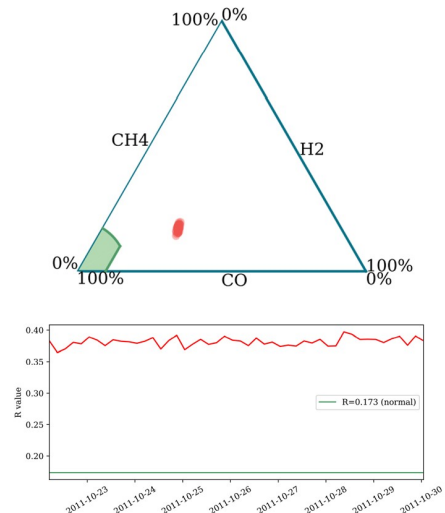
(a) Transformer B



(b) Transformer C

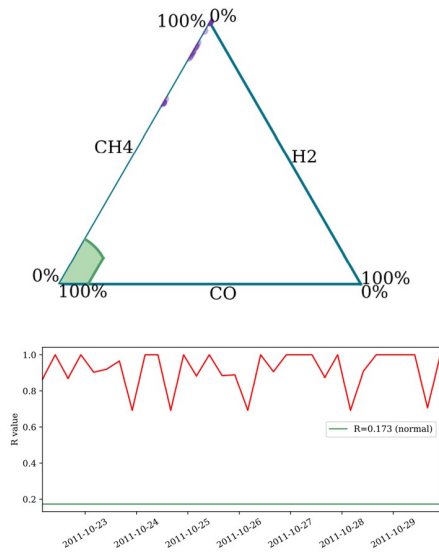


(c) Transformer D

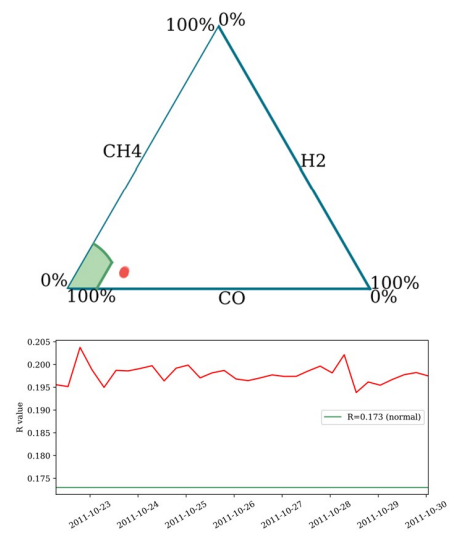


(d) Transformer E

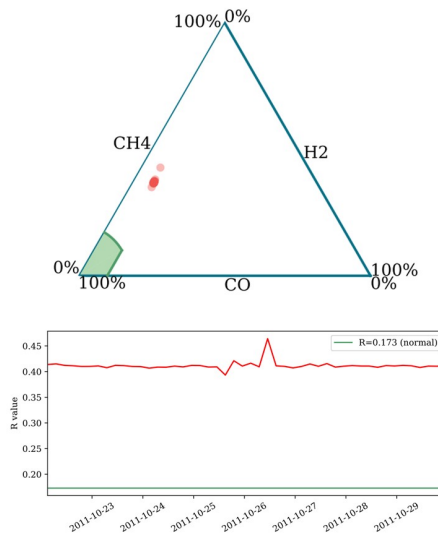
Figure 46: October 2011 storm (case study 3), transformers B-E. A not shown as DGA data not available for this storm period. Low Energy Degradation Triangle in the upper panel of each figure shows the location of the data in a ternary plot for 22nd–30th October 2011. The lower panel in each figure shows the R index, with the boundary of the normal region marked in green.



(a) Transformer F. Data points shown in purple indicate that one or more of the gas readings was 0 ppm.

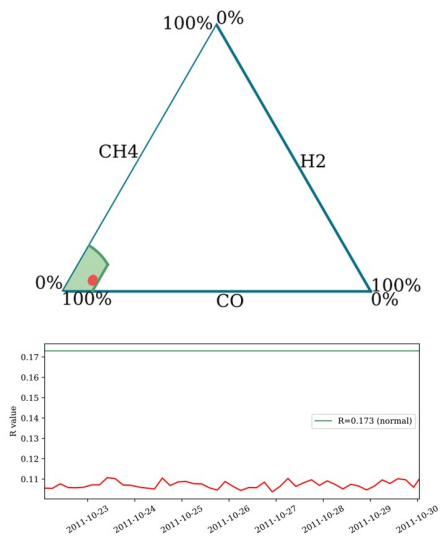


(b) Transformer G

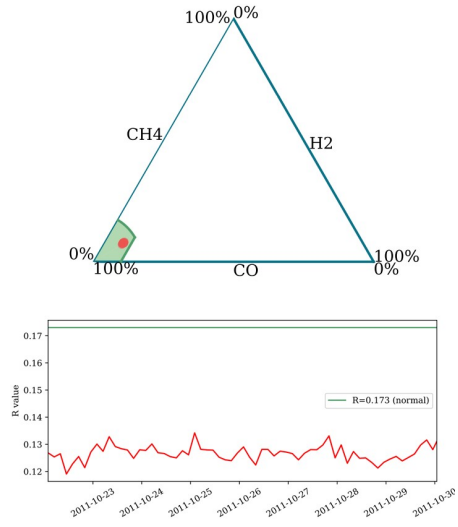


(c) Transformer H

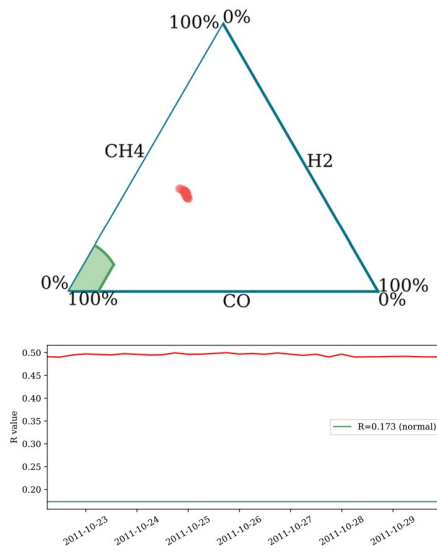
Figure 47: October 2011 storm (case study 3), transformers F-H. Low Energy Degradation Triangle in the upper panel of each figure shows the location of the data in a ternary plot for 22nd–30th October 2011. The lower panel in each figure shows the R index, with the boundary of the normal region marked in green.



(a) Transformer J



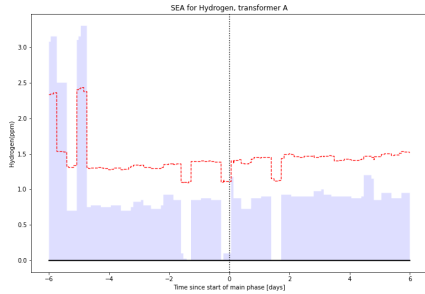
(b) Transformer K



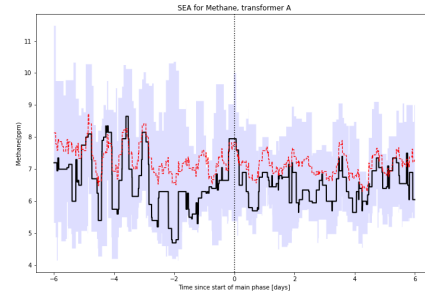
(c) Transformer L

Figure 48: October 2011 storm (case study 3), transformers F-H. I and M not shown due to lack of DGA data in this storm period. Low Energy Degradation Triangle in the upper panel of each figure shows the location of the data in a ternary plot for 22nd–30th October 2011. The lower panel in each figure shows the R index, with the boundary of the normal region marked in green.

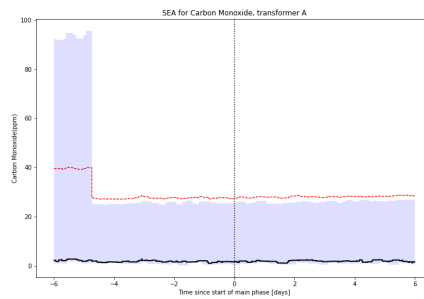
## D Superposed Epoch Analysis



(a) SEA for Hydrogen concentration levels in transformer A.

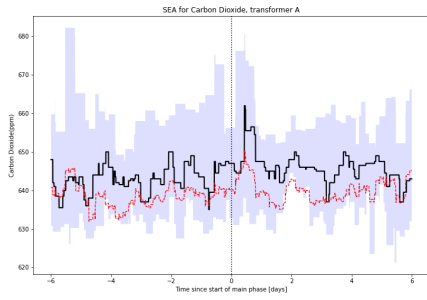


(b) SEA for Methane concentration levels in transformer A.

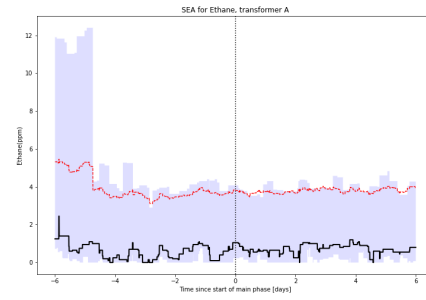


(c) SEA for Carbon Monoxide concentration levels in transformer A.

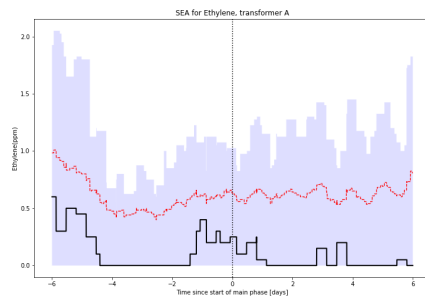
Figure 49: Superposed Epoch Analyses for 3 gas concentrations, superposed on the start of the main phase of 9 storms. The black line shows the median, red dashed line shows the mean and blue shaded region shows the interquartile range.



(a) SEA for Carbon Dioxide concentration levels in transformer A

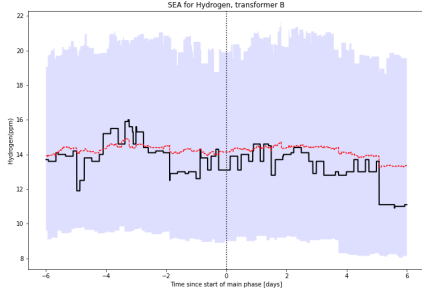


(b) SEA for Ethane concentration levels in transformer A

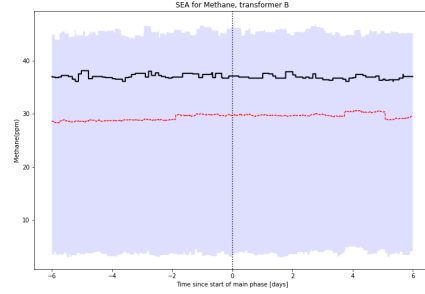


(c) SEA for Ethylene concentration levels in transformer A

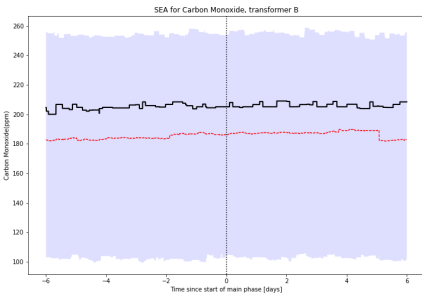
Figure 50: Superposed Epoch Analyses for 3 gas concentrations, superposed on the start of the main phase for 9 storms. The black line shows the median, red dashed line shows the mean and blue shaded region shows the interquartile range.



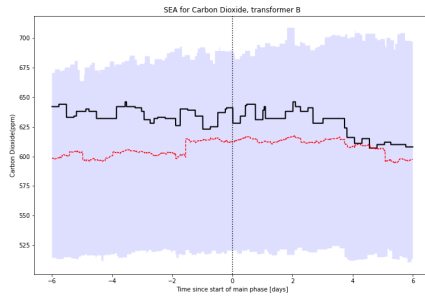
(a) SEA for Hydrogen concentration levels in transformer B.



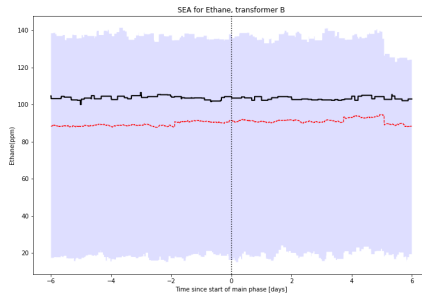
(b) SEA for Methane concentration levels in transformer B



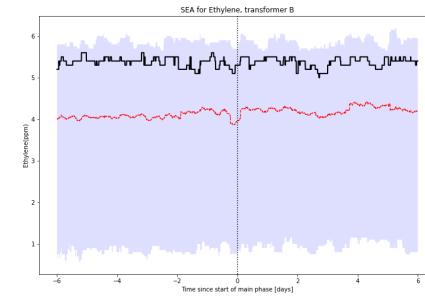
(c) SEA for Carbon Monoxide concentration levels in transformer B



(d) SEA for Carbon Dioxide concentration levels in transformer B

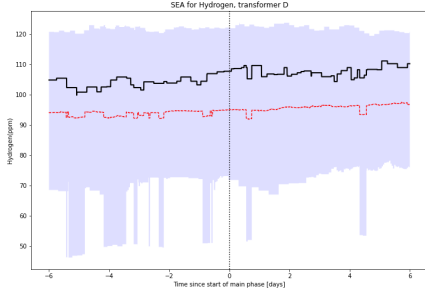


(e) SEA for Ethane concentration levels in transformer B

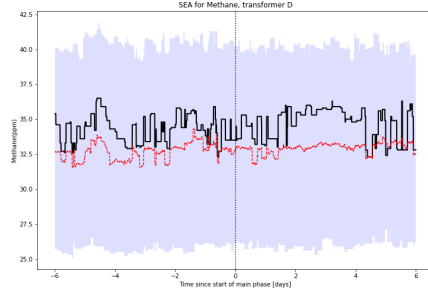


(f) SEA for Ethylene concentration levels in transformer B

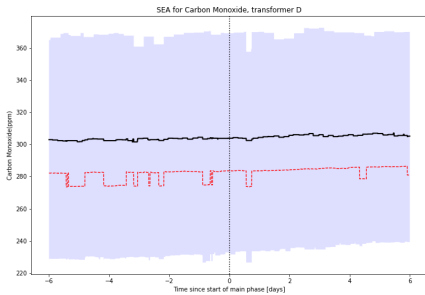
Figure 51: Superposed Epoch Analyses for 6 gas concentrations, superposed on the start of the main phase for 30 storms. The black line shows the median, red dashed line shows the mean and blue shaded region shows the interquartile range.



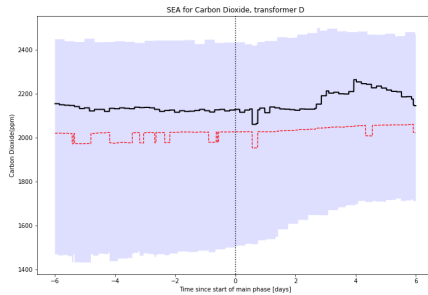
(a) SEA for Hydrogen concentration levels in transformer D.



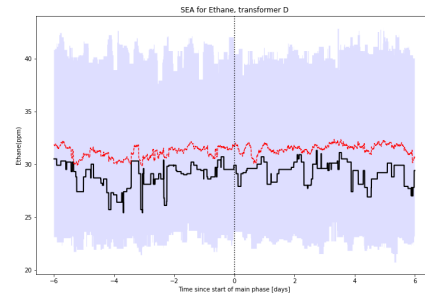
(b) SEA for Methane concentration levels in transformer D



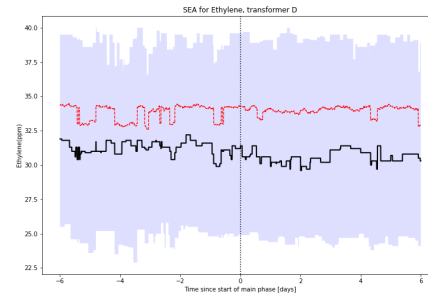
(c) SEA for Carbon Monoxide concentration levels in transformer D



(d) SEA for Carbon Dioxide concentration levels in transformer D

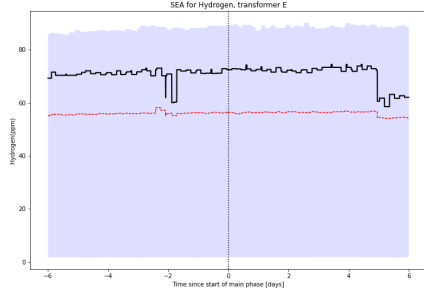


(e) SEA for Ethane concentration levels in transformer D

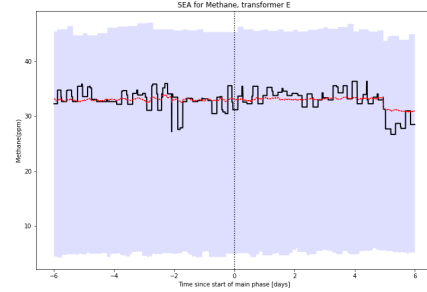


(f) SEA for Ethylene concentration levels in transformer D

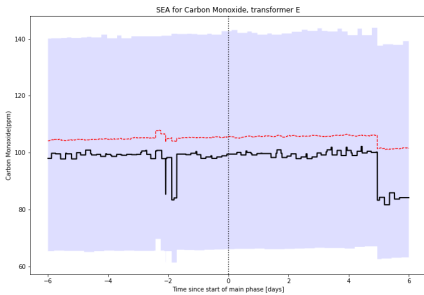
Figure 52: Superposed Epoch Analyses for 6 gas concentrations, superposed on the start of the main phase for 34 storms. The black line shows the median, red dashed line shows the mean and blue shaded region shows the interquartile range.



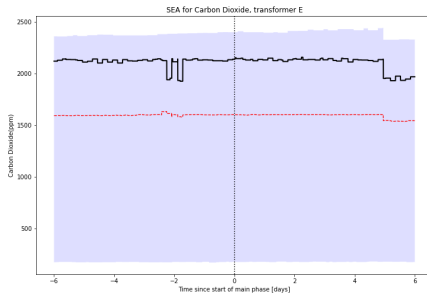
(a) SEA for Hydrogen concentration levels in transformer E.



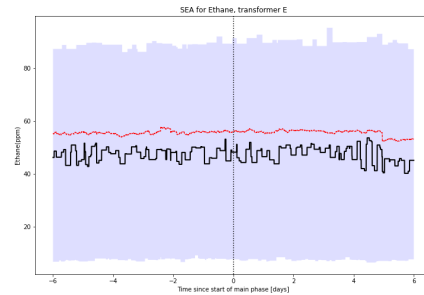
(b) SEA for Methane concentration levels in transformer E



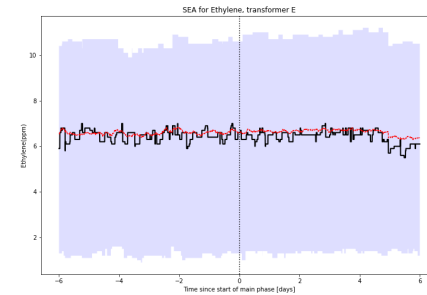
(c) SEA for Carbon Monoxide concentration levels in transformer E



(d) SEA for Carbon Dioxide concentration levels in transformer E

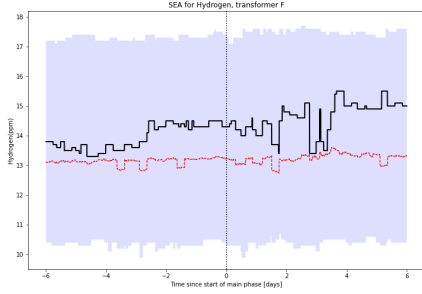


(e) SEA for Ethane concentration levels in transformer E

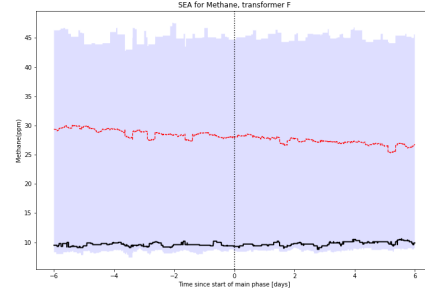


(f) SEA for Ethylene concentration levels in transformer E

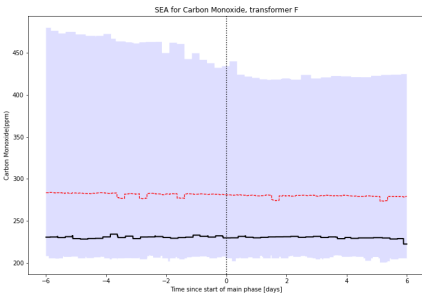
Figure 53: Superposed Epoch Analyses for 6 gas concentrations, superposed on the start of the main phase for 34 storms. The black line shows the median, red dashed line shows the mean and blue shaded region shows the interquartile range.



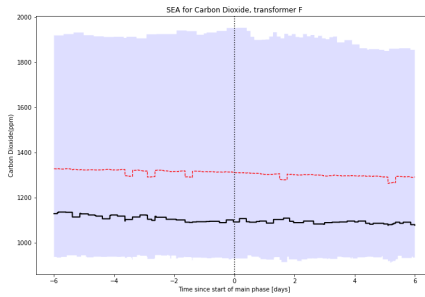
(a) SEA for Hydrogen concentration levels in transformer F.



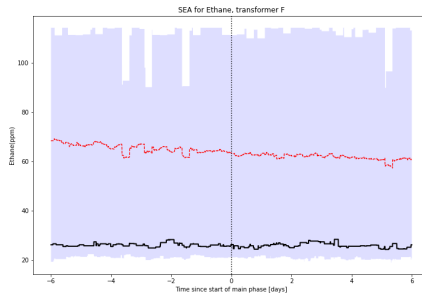
(b) SEA for Methane concentration levels in transformer F



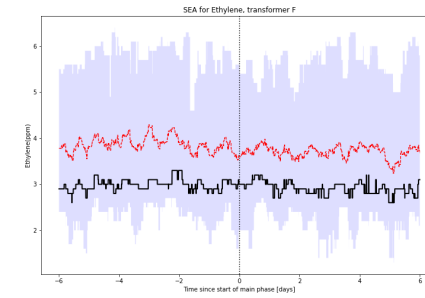
(c) SEA for Carbon Monoxide concentration levels in transformer F



(d) SEA for Carbon Dioxide concentration levels in transformer F

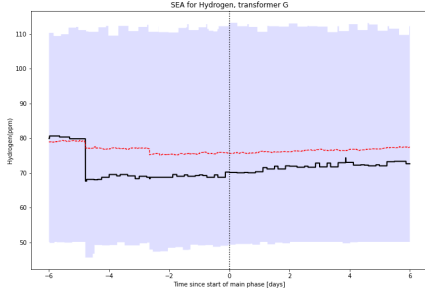


(e) SEA for Ethane concentration levels in transformer F

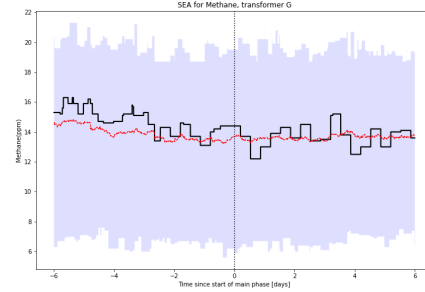


(f) SEA for Ethylene concentration levels in transformer F

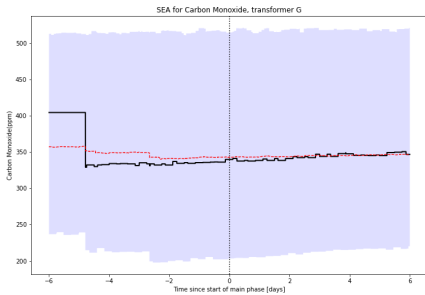
Figure 54: Superposed Epoch Analyses for 6 gas concentrations, superposed on the start of the main phase for 34 storms. The black line shows the median, red dashed line shows the mean and blue shaded region shows the interquartile range.



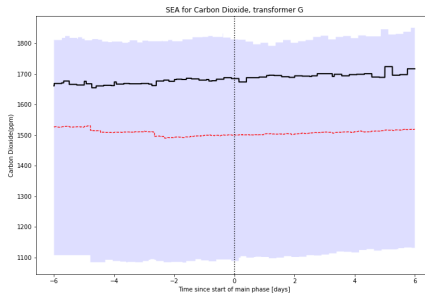
(a) SEA for Hydrogen concentration levels in transformer G.



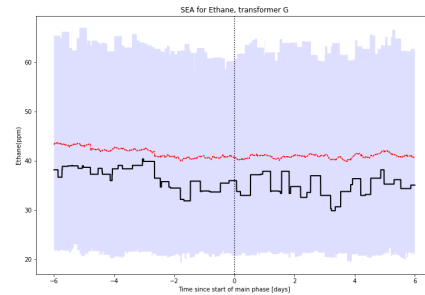
(b) SEA for Methane concentration levels in transformer G



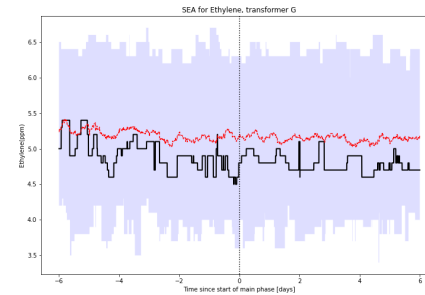
(c) SEA for Carbon Monoxide concentration levels in transformer G



(d) SEA for Carbon Dioxide concentration levels in transformer G

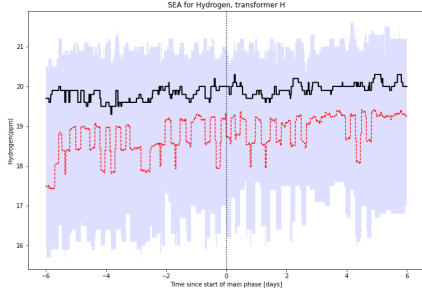


(e) SEA for Ethane concentration levels in transformer G

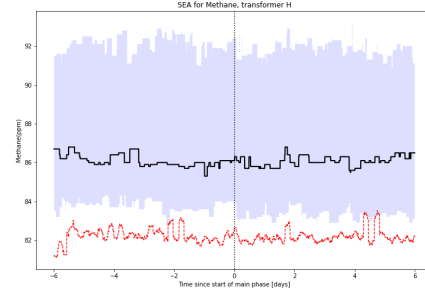


(f) SEA for Ethylene concentration levels in transformer G

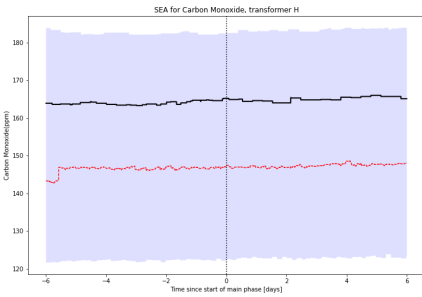
Figure 55: Superposed Epoch Analyses for 6 gas concentrations, superposed on the start of the main phase for 34 storms. The black line shows the median, red dashed line shows the mean and blue shaded region shows the interquartile range.



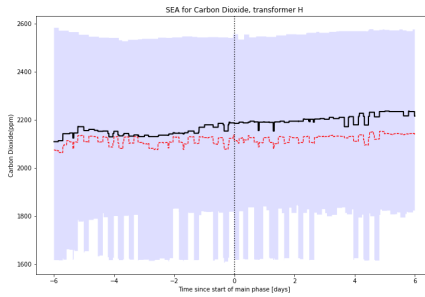
(a) SEA for Hydrogen concentration levels in transformer H.



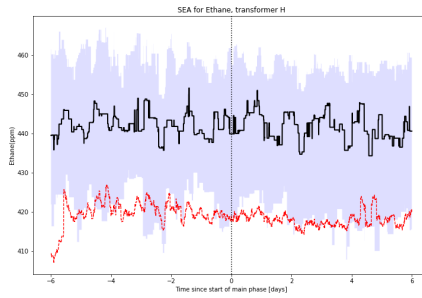
(b) SEA for Methane concentration levels in transformer H



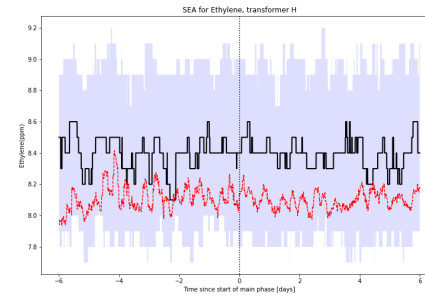
(c) SEA for Carbon Monoxide concentration levels in transformer H



(d) SEA for Carbon Dioxide concentration levels in transformer H

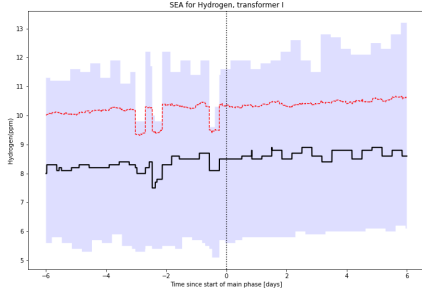


(e) SEA for Ethane concentration levels in transformer H

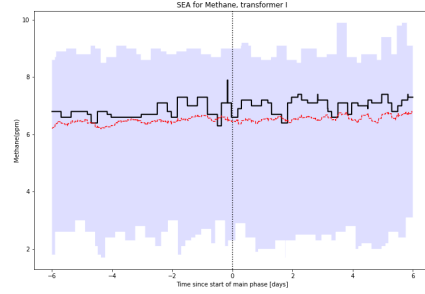


(f) SEA for Ethylene concentration levels in transformer H

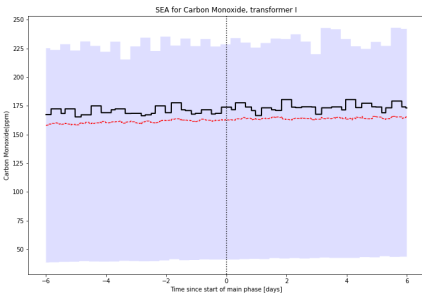
Figure 56: Superposed Epoch Analyses for 6 gas concentrations, superposed on the start of the main phase for 34 storms. The black line shows the median, red dashed line shows the mean and blue shaded region shows the interquartile range.



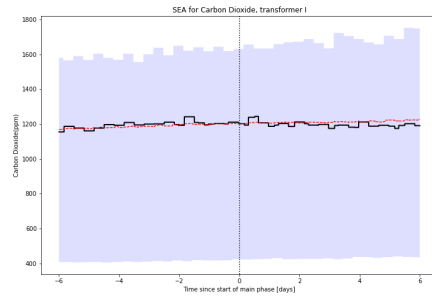
(a) SEA for Hydrogen concentration levels in transformer I



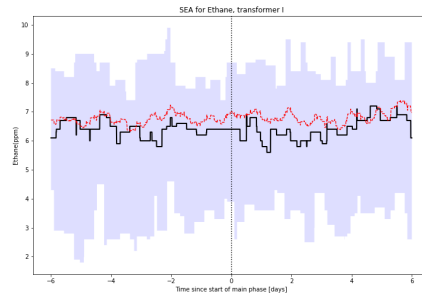
(b) SEA for Methane concentration levels in transformer I



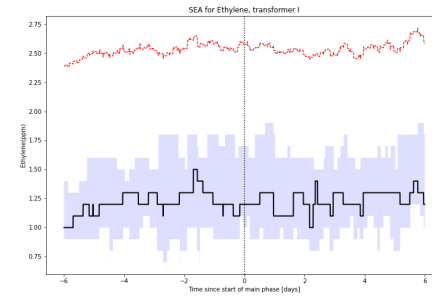
(c) SEA for Carbon Monoxide concentration levels in transformer I



(d) SEA for Carbon Dioxide concentration levels in transformer I

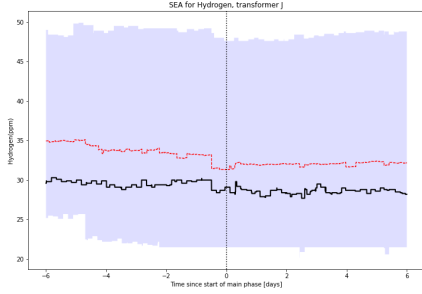


(e) SEA for Ethane concentration levels in transformer I

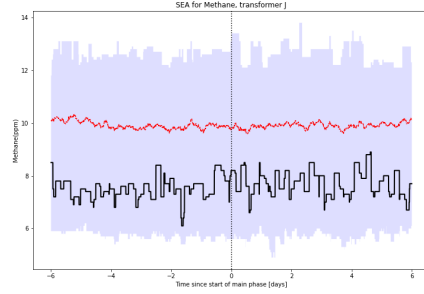


(f) SEA for Ethylene concentration levels in transformer I

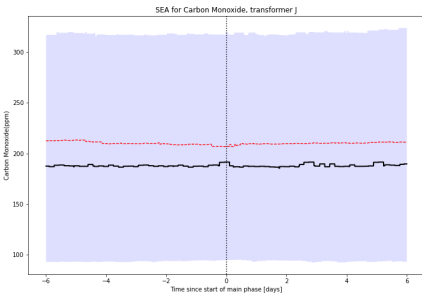
Figure 57: Superposed Epoch Analyses for 6 gas concentrations, superposed on the start of the main phase for 13 storms. The black line shows the median, red dashed line shows the mean and blue shaded region shows the interquartile range.



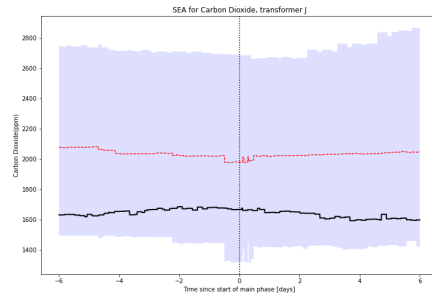
(a) SEA for Hydrogen concentration levels in transformer J



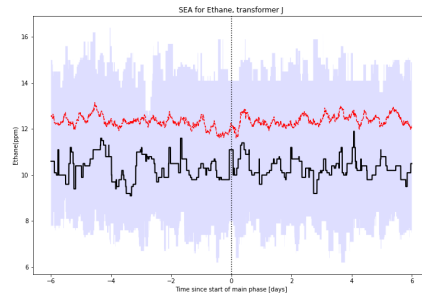
(b) SEA for Methane concentration levels in transformer J



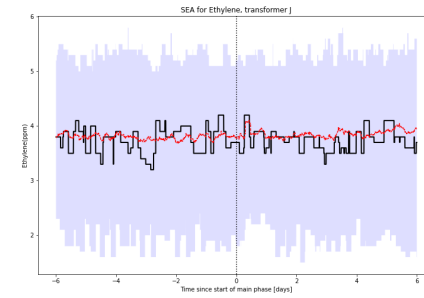
(c) SEA for Carbon Monoxide concentration levels in transformer J



(d) SEA for Carbon Dioxide concentration levels in transformer J

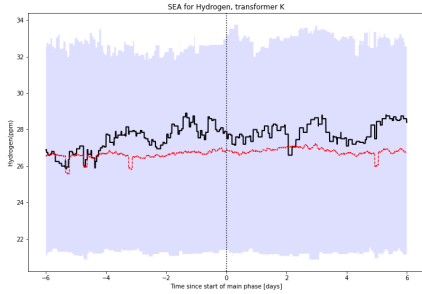


(e) SEA for Ethane concentration levels in transformer J

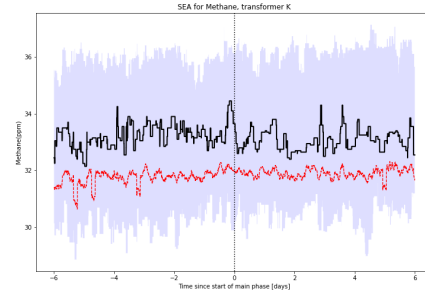


(f) SEA for Ethylene concentration levels in transformer J

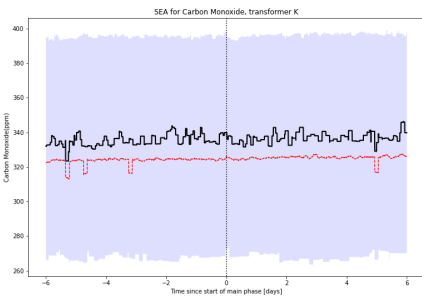
Figure 58: Superposed Epoch Analyses for 6 gas concentrations, superposed on the start of the main phase for 34 storms. The black line shows the median, red dashed line shows the mean and blue shaded region shows the interquartile range.



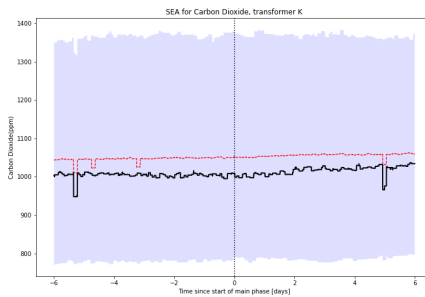
(a) SEA for Hydrogen concentration levels in transformer K



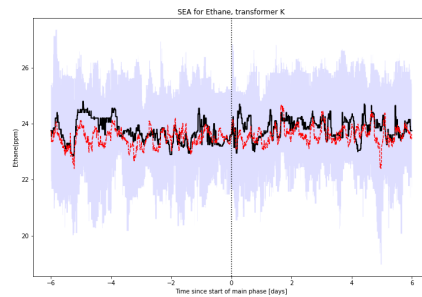
(b) SEA for Methane concentration levels in transformer K



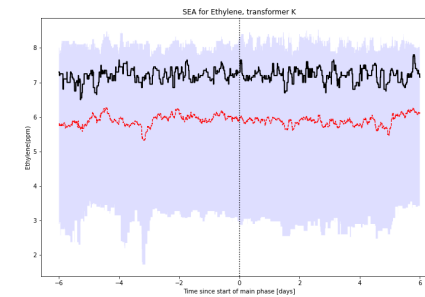
(c) SEA for Carbon Monoxide concentration levels in transformer K



(d) SEA for Carbon Dioxide concentration levels in transformer K

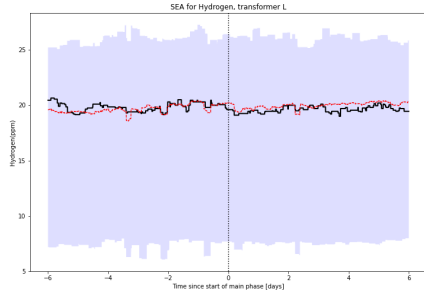


(e) SEA for Ethane concentration levels in transformer K

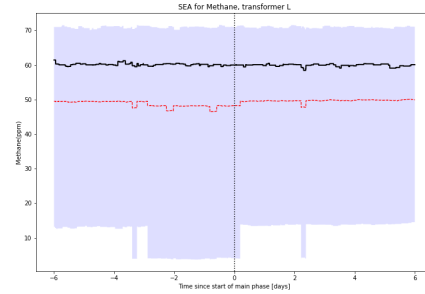


(f) SEA for Ethylene concentration levels in transformer K

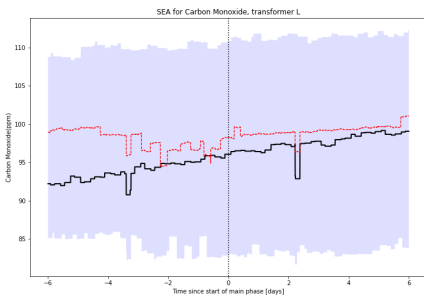
Figure 59: Superposed Epoch Analyses for 6 gas concentrations, superposed on the start of the main phase for 33 storms. The black line shows the median, red dashed line shows the mean and blue shaded region shows the interquartile range.



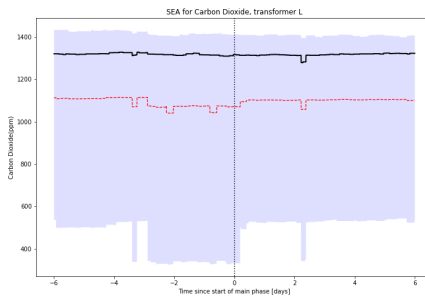
(a) SEA for Hydrogen concentration levels in transformer L



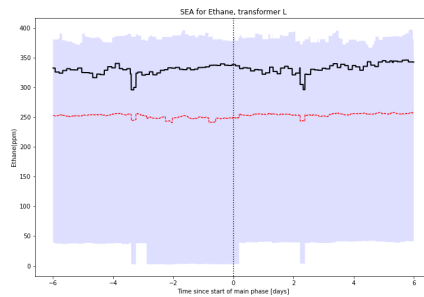
(b) SEA for Methane concentration levels in transformer L



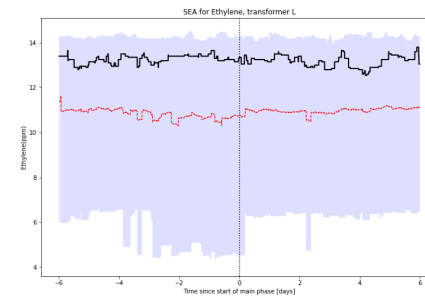
(c) SEA for Carbon Monoxide concentration levels in transformer L



(d) SEA for Carbon Dioxide concentration levels in transformer L

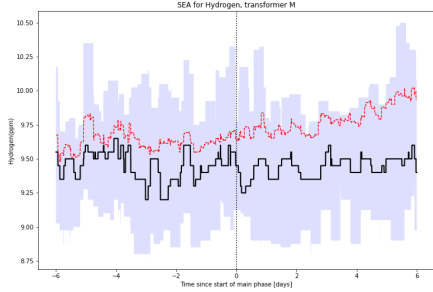


(e) SEA for Ethane concentration levels in transformer L

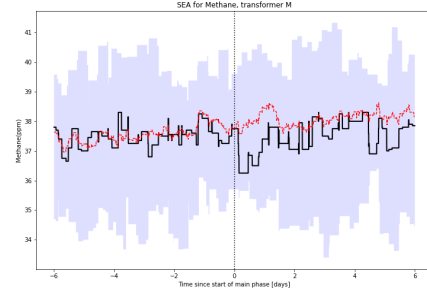


(f) SEA for Ethylene concentration levels in transformer L

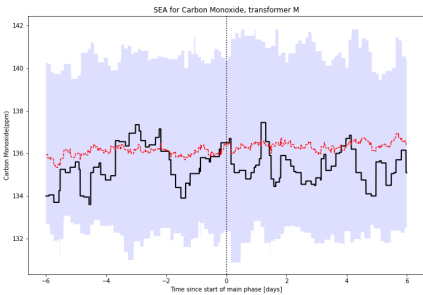
Figure 60: Superposed Epoch Analyses for 6 gas concentrations, superposed on the start of the main phase for 31 storms. The black line shows the median, red dashed line shows the mean and blue shaded region shows the interquartile range.



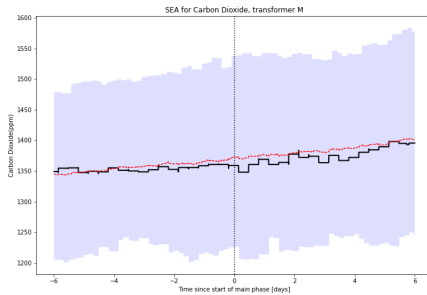
(a) SEA for Hydrogen concentration levels in transformer M.



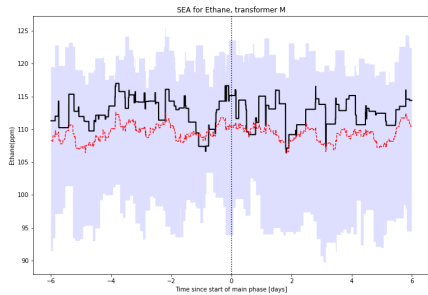
(b) SEA for Methane concentration levels in transformer M



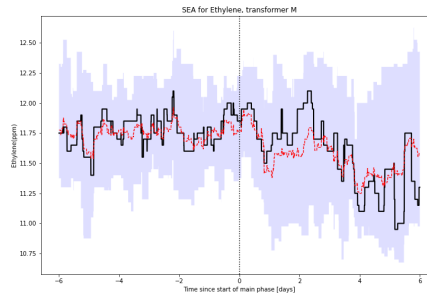
(c) SEA for Carbon Monoxide concentration levels in transformer M



(d) SEA for Carbon Dioxide concentration levels in transformer M



(e) SEA for Ethane concentration levels in transformer M



(f) SEA for Ethylene concentration levels in transformer M

Figure 61: Superposed Epoch Analyses for 6 gas concentrations, superposed on the start of the main phase for 12 storms. The black line shows the median, red dashed line shows the mean and blue shaded region shows the interquartile range.